Mid-Infrared Supercontinuum based Spectroscopic OCT

Hansen, Rasmus Eilkær

Publication date:
2023

Document Version
Publisher's PDF, also known as Version of record

DTU Electro
Department of Electrical and Photonics Engineering

Ph.D. Thesis

Mid-Infrared Supercontinuum based Spectroscopic OCT

Rasmus Eilkær Hansen, February 2023

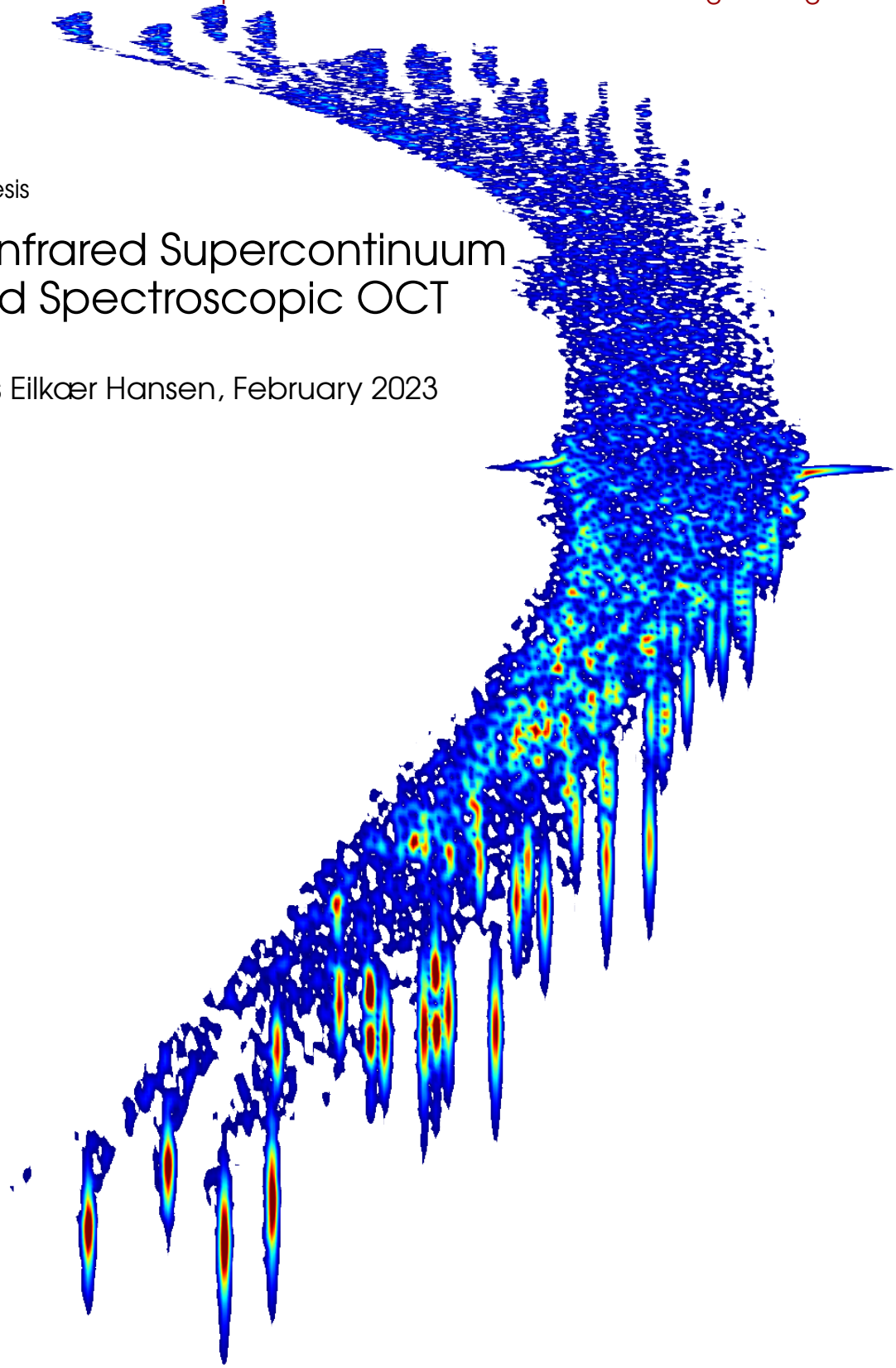

DTU Electro
Department of Electrical and
Photonics Engineering

Ph.D. Thesis

Mid-Infrared Supercontinuum based Spectroscopic OCT

Rasmus Eilkær Hansen

Kongens Lyngby, 2023

Mid-Infrared Supercontinuum based Spectroscopic OCT

Ph.D. Thesis
Rasmus Eilkær Hansen
February 28th, 2023

Cover: Spectrogram from a supercontinuum simulation in a photonic crystal fiber. The optical fibre was pumped in the anomalous dispersion regime, resulting in modulational instability, soliton generation, and dispersive wave generation.

Technical University of Denmark
DTU Electro
Department of Electrical and Photonics Engineering

Ørsteds Plads 343
2800 Kongens Lyngby, Denmark
Phone: +45 4525 6352

www.electro.dtu.dk

Preface

This thesis is submitted in candidacy for a Ph.D. degree in Electrical and Photonics Engineering from the Technical University of Denmark (DTU). The Ph.D project was carried out in the Fiber Sensors and Supercontinuum group at the DTU Department of Electrical and Photonics Engineering between March 2020 and February 2023. The project was supervised by Main Supervisor Professor Ole Bang and Co-supervisors Researcher Christian Rosenberg Peterson and Researcher Niels Møller Israelsen.

Rasmus Eilkær Hansen

Kongens Lyngby, February 28th, 2023

Abstract

This thesis provides a thorough review of mid-infrared (mid-IR) supercontinuum (SC) laser sources and their application within optical coherence tomography (OCT). A strong emphasis has been put on the development of the SC light sources as the performance of the light source in terms of power, spectral range, and noise directly impacts the quality, and acquisition speed of the OCT images.

The beautiful theory behind the nonlinear dynamics that is responsible for SC generation has been applied in numerical modelling. The numerical simulations are a useful tool to investigate a large set of fiber, and input pulse parameters. This has resulted in the prediction of a pump modulation scheme that can provide a more flat blue edge of commercially relevant SC sources based on input pulses with picosecond duration. It has also been applied to investigate SC generation in the curious case of a highly nonlinear fiber with an oscillating dispersion.

Numerical simulations have been further used to describe a novel type of of SC dynamics, which is important in the last stage in cascaded SC generation. In the cascaded SC sources, that we consider, a large number of solitons are created in the first fiber stages. The last stage is a chalcogenide fiber in which the solitons are coupled into normal dispersion. After initial nonlinear broadening the pulses are temporally dispersed until a temporal overlap is created between different spectral components, allowing a red-shift of power through Raman interaction.

Also in cascaded mid-IR SC generation a novel noise reduction mechanism has been shown both numerically and experimentally. The initial nonlinear broadening of solitons - also in the last stage of the cascade - results in spectral overlap between each subpulse, providing an effective averaging of subpulses within each pulse, thus reducing pulse-to-pulse fluctuations. We experimentally show a reduction from above 35 % to below 25 % in relative intensity noise across a broad bandwidth.

Based on cascaded mid-IR SC sources, OCT is performed with a centre wavelength of 4 μm. A centre wavelength in the mid-IR typically allows increased penetration in samples compared to the more conventional near-IR systems. The OCT system consists of an SC laser source, a Michelson interferometer, and detection based on near-IR detection after nonlinear upconversion of the mid-IR light. A characterisation of the OCT system is provided showing 11.9 μm axial resolution, 60 dB sensitivity, and 3.9 mm 6 dB sensitivity roll of distance.

The applicability of mid-IR OCT in non-destructive testing is shown on a set of paper samples. The 4 μm centre wavelength allowed penetrating through paper with a thickness of 90 μm, such that the thickness of the sample could be measured simultaneously with the refractive index. It was further shown that the OCT system can

show the roughness of the paper surface, and that it detect defects in the cases of tears, voids and contamination by a droplet of oil.

By spectrally subdividing the OCT images in the post processing it is possible to obtain spectral information such as spectrally dependent scattering or absorption of the sample. This data analysis technique was applied to show a proof-of-concept of spatially and temporally resolved imaging of CO_2 gas in channels inside a 3D printed epoxy resin cube.

Resumé

I denne afhandling præsenteres en grundig gennemgang af midt-infrarød (midt-IR) supercontinuum (SC) laserkilder og deres anvendelse inden for optisk kohærens tomografi (OCT). Der er lagt stor vægt på udviklingen af SC lyskilderne da lyskildens ydeevne i form af intensitet, farve sammensætning og støj direkte påvirker kvaliteten og billed raten af OCT-billederne.

Den smukke teori bag den ikke-lineære dynamik, der er ansvarlig for generering af SC kilder er blevet anvendt i numerisk modellering. De numeriske simuleringer er et nyttigt værktøj til at undersøge et stort sæt fiber, og input puls parametre. Dette har resulteret i forudsigelsen af en måde at modulere amplituden af input pulser så der kunne opnås en mere flad blå kant af kommercielt relevante SC-kilder baseret på input pulser med picosekund varighed. Det er også blevet anvendt til at undersøge SC-generering i det kuriøse af en meget ikke-lineær fiber med en oscillerende dispersions kurve.

Numeriske simuleringer er blevet brugt til at beskrive en ny type SC-dynamik, som er vigtig i den sidste fase i kaskade baseret generering af SC kilder. I de kaskade baserede SC kilder, som vi betragter, skabes et stort antal solitoner i de første fibre. Det sidste trin er en chalkogenid fiber, hvori solitonerne kobles til normal dispersion. Efter en indledende ikke-lineær spectral forbredning spredes pulserne tidsmæssigt, indtil der skabes et tidsmæssigt overlap mellem forskellige spektrale komponenter, hvilket tillader et rød skift af energi gennem Raman-interaktion.

En ny mekanisme der leder til støjreduktion, i generering af kaskade baserede midt-IR SC kilder, er illustreret både numerisk og eksperimentelt. Den indledende ikke-lineære forbredning af solitoner - også i det sidste trin af kaskaden - resulterer i et spektralt overlap mellem hver puls, hvilket giver en effektiv midling af puls-til-puls-fluktuationer. Vi viser eksperimentelt en reduktion fra over 35 % til under 25 % i relativ intensitets støj over en bred båndbredde.

Med kaskade baserede midt-IR SC-kilder udføres OCT med en centerbølgelængde på 4 μm. En centerbølgelængde i den midt infrarøde del af det elektromagnetiske spektrum tillader typisk øget penetration i prøver sammenlignet med de mere konventionelle nær-IR systemer. OCT-systemet består af en SC-laserkilde, et Michelson-interferometer og detektion baseret på nær-IR detektion efter ikke-lineær opkonvertering af midt-IR lyset. En karakterisering af OCT-systemet er præsenteret, den viser 11.9 μm dybde opløsning, 60 dB følsomhed og 3.9 mm forskel i optisk vejlængde før signalet er aftaget med 6 dB.

Anvendeligheden af midt-IR OCT i ikke-destruktiv testning er vist på et sæt papirprøver. 4 μm centerbølgelængde tillader at trænge gennem papir med en tykkelse på

90 μm, således at tykkelsen af prøven kunne måles samtidigt med brydningsindekset. Det er endvidere blevet vist, at OCT-systemet kan vise papiroverfladens ruhed, og at det kan bruges til defektdetektering i tilfælde af revner, hulrum og forurening med en olie dråbe.

Ved spektral underopdeling af OCT-billederne i efterbehandlingen er det muligt at opnå spektral information såsom spektralt afhængig spredning eller absorption af prøven. Denne teknik blev anvendt til at vise et proof-of-concept af rumlig og tidsmæssigt opløst billeddannelse af CO_2 gas i kanaler inde i en 3D-printet epoxy resin terning.

Acknowledgements

Through three years of work I have received encouragement, help, and guidance from a large number of people. In the following I will try to thank some of the people that have been part of this project.

First of all, I would like to thank my supervisor Ole. Working with you has taught me many lessons both in terms of physics and mathematics, but also in terms of communication. For that I am very grateful.

Thank you to my supervisors Christian and Niels. You have been constantly supportive and encouraging. I appreciate that you have always had the time for questions and discussions. Furthermore, most of the lab-skills I have is due to working with the two of you.

During my PhD I got to spend 4 months working with the Applied Optics Group at the University of Kent, supervised by Professor Adrian Podoleanu, and Lecturer Manuel Marques. I was happy to get to be a part of the career celebration of Adrian. It is impressive to see the impact and network that can be obtained from a long and dedicated career. The research stay gave me renewed motivation and joy in my research, and it gave me a lot of memories that I will certainly cherish for a long time. Thank you for having me.

Thank you to all my coworkers, past and present. I hope we can meet up for beers and fussball in the future as well.

A few times during my project we have decided that some electron microscopy images would be a nice addition to a project. This has always pleased me, as it has provided the opportunity to visit Ole Trinhammer and Nanoteket at DTU Physics.

My friends and family are a constant source of encouragement. This has given me calmness and has been a reminder that the job is after all not the most important thing. Thank you, not just for being part of my life, but for being my whole life.

My parents, Inger and Ole, have read this thesis and given me feedback and corrections, in spite of not really understanding the content - thank you. The congruence and commas would not have been the same without your help. An even bigger thank you for all of our good times, for our memories, and for your love.

Thank you to Simone, Amalie, Jeppe, Natasha, Adam, my brother Simon, and my parents for visiting me in Kent. Getting to share a bit of the experience with you amplified the energy and joy it provided me

Mark, you have been my strongest support, especially in the toughest of times. Strongest is an appropriate choice of words both in the figurative sense, but also in the literal sense of being able to lift heavy things.

My most significant acknowledgement goes to Asbjørn. Although the completion of this thesis is a joyful moment, it marks the unfortunate fact that our more than 8 years of collaboration and friendship shall now be replaced by just friendship. I truly believe that working with you makes us better than the sum of our individual parts - or at least better than two times my part. As such, any quality that a reader of this thesis hopefully finds, can be partly attributed to our numerous collaborations and endless discussions.

List of Publications

Primary Publications

[I] Rasmus Eilkær Hansen, Rasmus Dybbro Engelsholm, Christian Rosenberg Petersen, and Ole Bang
"Numerical observation of SPM rogue waves in normal dispersion cascaded supercontinuum generation,"

J. Opt. Soc. Am. B 38, 2754-2764 (2021).

[II] Rasmus Eilkær Hansen, Thorsten Bæk, Simon Lehnskov Lange, Niels Møller Israelsen, Markku Mäntylä, Ole Bang, and Christian Rosenberg Petersen,
"Non-Contact Paper Thickness and Quality Monitoring Based on Mid-Infrared Optical Coherence Tomography and THz Time Domain Spectroscopy,"

Sensors **2022**, 22(4), 1549.

[III] Rasmus Eilkær Hansen, Callum Robertsen Smith, Asbjørn Moltke, Christian Rosenberg Petersen, Sidharthan Raghuraman, Seongwoo Yoo and Ole Bang,
"Mid-IR supercontinuum noise reduction using a short piece of normal dispersion fiber - a general mechanism"

Response to reviewers submitted to Laser & Photonics Reviews.

[IV] Rasmus Eilkær Hansen, Asbjørn Moltke, and Ole Bang,
"High power supercontinuum lasers with a flat blue spectrum through pump modulation"

Accepted in Optics Letters.

Secondary Publications (Minor Contributions)

[V] Marcello Meneghetti, Christian R. Petersen, Rasmus E. Hansen, Abubakar I. Adamu, Ole Bang, and Christos Markos,
"Thermally tunable dispersion modulation in a chalcogenide-based hybrid optical fiber,"

Opt. Lett. 46, 2533-2536 (2021).

[VI] Niels M. Israelsen, Peter John Rodrigo, Christian R. Petersen, Getinet Woyessa, Rasmus E. Hansen, Peter Tidemand-Lichtenberg, Christian Pedersen, and Ole

Bang,
"High-resolution mid-infrared optical coherence tomography with kHz line rate,"
Opt. Lett. 46, 4558-4561 (2021).

Conference Contributions

[VII] Rasmus E. Hansen, Christian R. Petersen, and Ole Bang
"Giant Raman wave from SPM sidelobes in ANDi fiber,"
Conference on Lasers and Electro-Optics (2021).

[VIII] Rasmus E. Hansen, Christian R. Petersen, and Ole Bang
"Noise suppression through extreme self-phase modulation in cascaded mid-IR supercontinuum generation,"
Conference on Lasers and Electro-Optics Europe & European Quantum Electronics Conference (CLEO/Europe-EQEC) (2021).

[IX] Rasmus E. Hansen, Christian R. Petersen, and Ole Bang
"Statistics of SPM rogue waves," Conference on Lasers and Electro-Optics Europe & European Quantum Electronics Conference (CLEO/Europe-EQEC) (2021).

[X] Christian R. Petersen, Niels M. Israelsen, Getinet Woyessa, Kyei Kwarkye, Rasmus E. Hansen, Christos Markos, Amir Khodabakhsh, Frans J.M. Harren, Peter Rodrigo, Peter Tidemand-Lichtenberg, Christian Pedersen, and Ole Bang "Supercontinuum based mid-infrared OCT, spectroscopy, and hyperspectral imaging" Conference on Lasers and Electro-Optics Europe & European Quantum Electronics Conference (CLEO/Europe-EQEC) (2021).

[XI] Christian Rosenberg Petersen, Narayanan Rajagopalan, Niels Møller Israelsen, Rasmus Eilkær Hansen, Christos Markos, Claus E Weinell, Søren Kiil, and Ole Bang "Laser-Based Non-Destructive 3D Scanning of Marine Coatings" 7th World Maritime Technology Conference 2022

List of Abbreviations

ANDi all normal dispersion. 11, 30, 65

AR anti-reflective. 44, 45, 63, 64

DOF depth of field. 57

DW dispersive wave. 13, 14, 16, 21, 22, 27, 30, 31, 35, 38, 44, 50, 51, 54, 55

FD Fourier-domain. 60

FEM finite element modelling. 10, 11

FFT fast Fourier transform. 7, 8, 61

FFTW fastest Fourier transform in the west. 8

FWHM full width at half maximum. 13, 17, 31, 35, 49, 57, 61, 65, 67, 80

GNLSE generalised non-linear Schrödinger equation. 3, 5, 6, 8, 9, 14, 16, 25, 31, 35, 52

IR infrared. 2, 3, 10, 14, 16, 18, 25, 29–31, 35, 43–45, 50, 52, 55, 56, 59, 62–64, 66–68, 73, 75, 77, 78, 85

JWST James Webb Space Telescope. 1

MI modulational instability. 13, 23, 30, 43, 53, 65

NA numerical aperture. 11, 25, 31, 39, 50, 57

NLSE nonlinear Schrödinger equation. 5, 6

OCT optical coherence tomography. 1–3, 16, 30, 31, 39, 44, 50, 55–69, 72–82, 85, 86

OPD optical path difference. 2, 60–62, 66, 67, 81

OSA optical spectrum analyser. 13, 46, 49, 51

OWB optical wave breaking. 13, 14, 27, 30, 34–36, 38, 43

PCF photonic crystal fiber. 9–11, 16, 62

PES polyethersulfone. 25

PSD power spectral density. 13, 16–24, 27, 28, 30, 34, 49, 53

RIN relative intensity noise. 16, 17, 20–22, 30, 43, 46–51, 53, 54, 65, 85

RKF45 Runge-Kutta-Fehlberg-45. 8

S-OCT spectroscopic optical coherence tomography. 3, 75, 83

SC supercontinuum. 2, 3, 5, 6, 8, 11, 14–16, 25, 28–31, 33, 43–48, 50, 52, 55, 62–65, 74, 75, 85

SEM scanning electron microscope. 9, 77, 78

SLD superluminescent diode. 1, 73

SNR signal-to-noise ratio. 60, 66

SPM self phase modulation. 5, 13, 14, 27, 30, 34–38, 41–43

SRIN spectrally averaged RIN. 17, 20, 21

SRS stimulated Raman scattering. 36, 38–40

SS swept source. 57, 60–63

SSFS soliton self-frequency shift. 14, 16, 18, 27, 41

TD time-domain. 57, 59, 60, 68

UV ultraviolet. 16, 56, 62

ZDW zero dispersion wavelength. 11, 13, 15, 25, 27, 30, 31, 33, 35–40, 43–45, 50, 51, 53–55

Contents

CHAPTER 1

Introduction

Imaging is a fundamental tool to understand everything around us, from the distant universe to the smallest elements of matter. In the year 2022 this was especially apparent with the first images from the James Webb Space Telescope (JWST) [1].

While the scale and purpose of various imaging modalities differ widely, the parameters we care about are often the same: Resolution, integration time, and colour. By increasing the size of the mirrors on the JWST, increased resolution and reduced integration time can be achieved. Thereby, smaller objects can be observed while simultaneously being able to cover a bigger part of the universe. The JWST is equipped with detectors that observe light in a spectral range between 0.6 μm and 26 μm. The broad bandwidth allows observation of the early universe, temporally resolving the signal from distant galaxies, and measuring the absorption spectrum of exoplanets [2]. The measurement of absorption spectra of gases is known as spectroscopy, which is a powerful technique that, in the case of JWST, enables determination of the composition of the atmosphere of an exoplanet. A similar functionality in optical coherence tomography (OCT) systems has put the "spectroscopic" in "spectroscopic optical coherence tomography".

OCT was first introduced in 1991 [3]. They used a superluminescent diode (SLD) and obtained an axial (depth) resolution of 17 μm. The illuminating light source in OCT is particularly important because it sets the axial resolution, δz, through the relation

$$\delta z \propto \frac{\lambda_c^2}{\Delta\lambda}, \tag{1.1}$$

where λ_c is the centre wavelength of the source, and $\Delta\lambda$ the bandwidth. The constant of proportionality is of a magnitude ~ 1 and depends on the spectral shape of the light source. Because of the intimate relation between resolution and bandwidth, that is not shared with most other imaging modalities, the development of OCT and appropriate broadband light sources have gone hand-in-hand [4]. The choice of light source can mean the difference between a resolution of tens of microns to sub-micron [5], and all the way to the extreme case of doing OCT with soft x-rays, resulting in 2 nm resolution [6]. In terms of integration time, the light source can mean the difference between Hz line rates all the way up to 40 MHz [7].

A commonly used analogy to OCT is ultrasound imaging, which is conceptually very similar. However, the application of ultrasound in medical imaging, and in particular in fetal imaging, has rendered ultrasound imaging a very familiar concept for most people. The main difference between ultrasound imaging and OCT is that the echo of sound is measured in ultrasound imaging, while the reflection and scattering of light is measured in OCT. The conceptual similarity between the two has one important

caveat: The return time of the "echo" of a short pulse of light is extremely short, unless long distances are considered, which makes it challenging to detect. This is due to the light travelling 1 million times faster than sound in normal atmospheric conditions. Therefore, the return time of optical pulses in OCT is not measured directly, but instead relatively to the return time of something else. Specifically, a so-called Michelson interferometer as shown in Figure 1.1 is used. The amplitude of light exiting

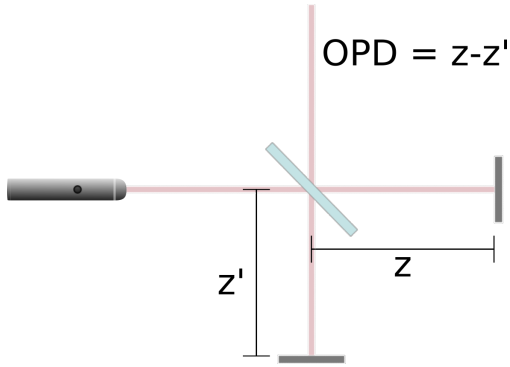

Figure 1.1: A Michelson interferometer. A beam splitter is used to split incoming laser light into two orthogonal paths with path lengths z and z'. The difference in time it takes light to travel the two distances is called the optical path difference (OPD).

a Michelson interferometer is extremely sensitive to the optical path difference (OPD), $(z - z')$, of the two arms of the interferometer. In the most extreme cases, changes of $\sim 10^{-18}$ m have been observed in a four km long arm of an interferometer to confirm the existence of gravitational waves [8]. Similarly, an interferometer can be used in OCT to measure the difference in return time of light from a sample situated in one arm of an interferometer, by comparing it with light reflected from a mirror in the other arm.

The inverse relation between axial resolution and bandwidth of the light source meant that supercontinuum (SC) lasers were quickly recognised as promising light sources for OCT, providing record breaking axial resolution at many different centre wavelengths [5, 9, 10]. SC laser sources also find a wide range of applications, outside of OCT including spectroscopy [11], confocal microscopy [12], and histopathology [13]. SC sources are extremely broadband laser sources, that can often span multiple octaves [14, 15]. Furthermore, SC laser sources can reach wavelength regimes, with continuous and flat spectra at high repetition rates (MHz in the mid-infrared (IR)), which is hard to achieve with other laser sources. Therefore, SC laser sources are very promising in spectral ranges that have so far not been explored in depth - and in particular the mid-IR.

This work focuses on OCT in the mid-IR using an in-house built SC laser source with a spectrum that spans past 4.5 μm. The OCT system takes advantage of almost 1 μm of the bandwidth of the SC laser centred approximately at 4 μm. The broad spectrum allows spectrally resolving the OCT images, which along with a centre wavelength

within the molecular fingerprint region has allowed the novel application of performing both spatially and temporally resolved imaging of the presence of gaseous CO_2.

All of the results within OCT in this thesis have been enabled by SC lasers, and the quality of the OCT images is directly linked to the performance of the SC laser source. Therefore, a large part of the text will concern the spectral dynamics leading to mid-IR SC generation, the noise performance of SC lasers, and high performance numerical simulations of SC generation.

1.1 Outline

The end goal of my PhD project is given in the title: Mid-Infrared Supercontinuum based Spectroscopic OCT. To build towards the goal the first three chapters of the thesis introduce SC generation such that the mid-IR SC laser in our OCT setup can be described and understood. There is a heavy emphasis on SC theory that is not strictly necessary to understand mid-IR spectroscopic OCT, but it is needed to understand the SC light source that enabled it.

Chapter 2 will introduce the so-called generalised non-linear Schrödinger equation (GNLSE) that is used to perform numerical simulations of SC generation. The inputs to this equation are the important fiber parameters, that will be thoroughly described both in terms of obtaining and understanding them. A computationally efficient implementation of the GNLSE will be introduced, and a simulated result will be used to showcase most of the nonlinear dynamics that are relevant in the remaining thesis.

In Chapter 3, two applications of the GNLSE implementation are presented. The first is an approach to a more flat blue part of an SC spectrum where the peak powers of the input pulses are modulated, also described in paper [IV]. The second involves simulating the SC dynamics in a fiber where the dispersion is modulated and switches sign many times as a function of wavelength, as described in paper [V].

Chapter 4 concerns SC generation on a more practical level. For OCT we use a cascaded SC laser, therefore such lasers will be described in this chapter. The two final sections of the chapter describe work I have done to understand and improve mid-IR SC generation. First, new nonlinear dynamics resulting in an efficient redshifting of power and the appearance of a novel type of optical rogue wave is described in section 4.1. This work was first reported in paper [I]. In section 4.2, work from the paper [III] is covered. In this paper we experimentally showed SC noise reduction by adding only a short piece of normal dispersion fiber to an SC source. The GNLSE was used to explain the origin of the noise reduction.

In chapter 5, mid-IR OCT will be introduced. The application of the OCT system in paper thickness and quality monitoring using our mid-IR OCT system, will be covered in section 5.3. This work was also covered in paper [II], sometimes referred to as ”the paper-paper”

The thesis culminates in Chapter 6, where S-OCT is introduced. S-OCT is applied to temporally and spatially resolve the presence of CO_2 inside channels in an epoxy resin cube. This chapter concerns a work that is still in progress, therefore the tone of

the chapter reflects the fact that the analysis is only one approach out of many that could be imagined.

Finally, in Chapter 7, I will conclude the thesis and present an outlook.

CHAPTER 2

Supercontinuum Generation - Theory and Simulations

Nonlinear dynamics in optical fibers are well described with numerical simulations [16]. Many of these processes can be understood with the nonlinear Schrödinger equation (NLSE)

$$i\partial_z A = -\gamma A|A|^2 + \frac{\beta_2}{2}\partial_t^2 A, \tag{2.1}$$

where $A = A(z,t)$ is the envelope of an optical pulse travelling along the z-direction in an optical fiber. $\partial_{z,t}$ denotes a partial derivative with respect to the sub-scripted variable, γ is a measure of the nonlinearity of the optical fiber, and β_2 is the dispersion of the fiber. When $\beta_2 > 0$ the term "normal" dispersion is used, and $\beta_2 < 0$ is denoted "anomalous" dispersion. In supercontinuum generation none of the two cases is more "normal" than the other despite the labelling, but the distinction is very important as the nonlinear dynamics differ remarkably between the two regimes. Analytical solutions to the NLSE exist, including the soliton solution that is very important in SC generation. A soliton is a very stable pulse, that is capable of retaining its shape when subject to many perturbations, and can be generated from other pulse shapes during propagation in the fiber.

In the limiting case of $\gamma = 0$, an optical pulse only experiences temporal broadening or narrowing, when instead $\beta_2 = 0$ the pulse only experiences a nonlinear phase shift known as self phase modulation (SPM). Exact analytical solutions exist in both of these limiting cases, which can be used to simplify numerical simulations by solving them separately and consecutively in small steps. This is known as the Fourier split-step method [16]. More general equations than 2.1 exist, that include more nonlinear effects, higher order dispersion, and loss. These equations are typically all called the generalised non-linear Schrödinger equation (GNLSE), and in section 2.1 the full version that has been solved in this work will be introduced along with its numerical solver.

Both γ and β_2 depend on the material as well as the specific geometry of the fiber. The simplest case is step-index glass fibers, for which analytical treatment is possible. For fibers with a complicated geometry one has to refer to experiments, numerical calculations, or find an appropriate assumption to obtain the fiber parameters. A description of how to obtain these parameters is given in section 2.3.

Simulations are an excellent tool to describe and illustrate the nonlinear effects in optical fibers. Therefore, most of the nonlinear effects that dominate in SC generation will be introduced already in section 2.4 to ease the discussion of the effects in later chapters.

2.1 The Generalised Nonlinear Schrödinger Equation

Equation 2.1 is the NLSE in its shortest form. This form allows exact analytical solutions such as the soliton solution. More complicated dynamics, such as loss, higher order dispersion, Raman response, and frequency dependent nonlinearity, can be described through additional terms and corrections. The version of the GNLSE used in this project was derived by Rasmus Dybbro Engelsholm in his PhD-Thesis [17]. The original version included multiple optical modes and arbitrary input polarisation. All simulations in this project assume scalar propagation of a single mode. In my masters project [18] [1] I showed how this reduces the complexity of the equation such that the equations that solve for the frequency-, Ω, and z-dependent pulse envelope $G(\Omega, z)$ can be stated as:

$$\begin{aligned}&\frac{\partial}{\partial z}\left[\exp(i\beta_{eff}z)^* G(\Omega,z)\right] = i\gamma(\Omega)K(\Omega)\exp(i\beta_{eff}z)^* \\ &\mathcal{F}\left\{\mathcal{F}^{-1}[G(\Omega,z)K(\Omega)]\mathcal{F}^{-1}\left[\tilde{R}(\Omega)\ \mathcal{F}\left[\mathcal{F}^{-1}[G(\Omega,z)K(\Omega)]^*\mathcal{F}^{-1}[G(\Omega,z)K(\Omega)]\right]\right]\right\},\end{aligned} \tag{2.2}$$

[1] Available through DTU findit: https://findit.dtu.dk/en/catalog/5e550f03d9001d0164073e90

where

$$\begin{aligned}
\beta_{eff} =& \beta_{eff}(\Omega,\Omega_p,\Omega_0) = \beta_{eff}(\Omega,\Omega_p,\Omega_0) \equiv \beta - \beta_1|_{\Omega=\Omega_p}(\Omega-\Omega_0) - \beta_0|_{\Omega=\Omega_0} + i\frac{\alpha(\Omega)}{2},\\
\beta =& \frac{n_{eff}(\Omega)\Omega}{c},\\
\gamma(\Omega) =& \frac{n_2\Omega}{c\mathrm{A_{eff}}(\Omega_0)}\frac{n_{eff}^2(\Omega_0)}{n_{eff}^2(\Omega)},\\
\mathrm{A_{eff}}(\Omega) \equiv& \frac{\left(\int\int|\boldsymbol{\mathcal{E}}(\Omega,x,y)|^2\mathrm{d}x\mathrm{d}y\right)^2}{\int\int|\boldsymbol{\mathcal{E}}(\Omega,x,y)|^4\mathrm{d}x\mathrm{d}y},\\
K(\Omega) =& \left[\frac{\mathrm{A_{eff}}(\Omega_0)}{\mathrm{A_{eff}}(\Omega)}\right]^{\frac{1}{4}},\\
\tilde{R}(\Omega) =& 1 - f_R + f_R\tilde{h_R}(\Omega),\\
\tilde{f}(\Omega) =& \mathcal{F}\{f(t)\} = \int_{-\infty}^{\infty} f(t)\exp(-i\Omega t)\mathrm{d}t,\\
f(t) =& \mathcal{F}^{-1}\{\tilde{f}(\Omega)\} = \frac{1}{2\pi}\int_{-\infty}^{\infty}\tilde{f}(\Omega)\exp(i\Omega t)\mathrm{d}\Omega.
\end{aligned} \tag{2.3}$$

In the above equations c is the speed of light, Ω_0 is the centre of the frequency grid, Ω_p can be chosen freely but is conveniently chosen to be the centre frequency of the input pulse, such that the simulation is performed in a moving frame of reference following the input pulse, $\alpha(\Omega)$ is the intensity attenuation, $n_{eff}(\Omega)$ is the real part of effective refractive index, n_2 is the nonlinear refractive index, $\mathrm{A_{eff}}(\Omega)$ is the effective area of the pulse mode, $\boldsymbol{\mathcal{E}}(\Omega,x,y)$ is the transverse mode profile, f_R is the fractional contribution of the Raman response to the total nonlinear strength, and $\tilde{h_R}(\Omega)$ is the shape of the Raman response. $\mathcal{F}\{..\}$ and $\mathcal{F}^{-1}\{..\}$ are the Fourier transform and inverse Fourier transform, respectively, which numerically are performed using the fast Fourier transform (FFT). The pulse envelope $G(\Omega,z)$ has been normalised such that $|G(\Omega,z)|^2$ has units W.

All of the parameters that are marked in red are the fiber geometry and material dependent parameters that are needed as input to the simulations. In section 2.3 I will show examples of these parameters, and cover how they can be obtained. In the following section the numerical solver will be briefly introduced.

2.2 Numerical Solver

The numerical implementation that was used for almost all the GNLSE results presented in this thesis was developed as a collaboration between Asbjørn Moltke and I. We decided to implement our own solver for two reasons: To have a more efficient solver such that more computationally heavy problems could be solved. These problems include highly nonlinear fibers, big parameter spaces in input pulse parameters,

and supercontinuum noise estimation. Secondly, it was during the COVID shutdown, so lab-work was not an option. The numerical implementation was inspired heavily by one made by Rasmus Dybbro Engelsholm [17, 19]

The program has been written in C, which has the advantage compared to other languages, such as Matlab or Python, that the user operates at a much lower level. The lower level of operation means that extra effort can be put into performance enhancement by choosing appropriate data types, memory handling, and compilation of the code. As an example we found that the Intel C compiler (icc) increased the speed of the code by a factor of 2 compared to the clang compiler (gcc).

The high number of FFTs in equation 2.2 come at a significant computational cost. Therefore, the implementation of the FFT is very important for the performance of the solver. For this purpose we chose the open source library fastest Fourier transform in the west (FFTW) [20]. One of the main attributes of the FFTW implementation is that it will spend some time choosing an FFT algorithm specifically for the hardware on which it runs in an optimisation step called FFTW-planning. Once an FFTW-plan has been generated, it can be saved, such that it can be reused. FFTW comes with its own set of data types and algebraic functions. Here we used the data-type "fftw_complex" for all complex valued arrays, and the function "cexp()" for complex exponentials.

Traditional Fourier split-step algorithms [16] introduce an error that goes with the square, $\mathcal{O}(h^2)$, of the step size h. Instead the GNLSE is here solved in the "interaction-picture" introduced in [21], which allows solving the equations with higher accuracy. In the interaction picture, the numerical accuracy can be chosen to be any power in h, however high accuracy typically comes at the expense of high computational cost of each step. In our implementation we chose the Runge-Kutta-Fehlberg-45 (RKF45) algorithm [2]. The RKF45 solves the problem with both $\mathcal{O}(h^4)$ and $\mathcal{O}(h^5)$ accuracy in each step while reusing most of the intermediate calculations. The two solutions, with different accuracy, enable continuously adjusting the step size according to the relative difference between them.

Depending on the problem at hand, the question of latency vs throughput should be considered. Latency refers to the amount of time it takes to finish one simulation, whereas throughput refers to the number of simulations that can be performed in a given unit of time. To reduce the latency of the simulations, the code has been parallelised using OpenMP. However, the performance of each computing core generally reduces with the number of cores running in parallel. With OpenMP, the calculation can be performed on as many CPU cores with shared memory that are available. Higher degree of parallelisation can be achieved by including computing cores that do not share memory, for example using MPI. Another approach is to use GPU parallelisation, as was done in [17]. However, both of these options come at a significant increase in complexity of the code. We chose CPU parallelisation due to the availability of up to 300 computing cores in the DTU computing cluster. Doing noise calculations on SC spectra is an "embarrassingly parallel"[3] problem, as each simulation is independent of

[2]See for example: https://en.wikipedia.org/wiki/Runge%E2%80%93Kutta%E2%80%93Fehlberg_method
[3]This is in fact the defining term: https://en.wikipedia.org/wiki/Embarrassingly_parallel

all other simulations.

2.3 Parameters for the GNLSE

As an example of the parameters for the GNLSE two silica photonic crystal fiber (PCF) designs are considered. A scanning electron microscope (SEM) image of the

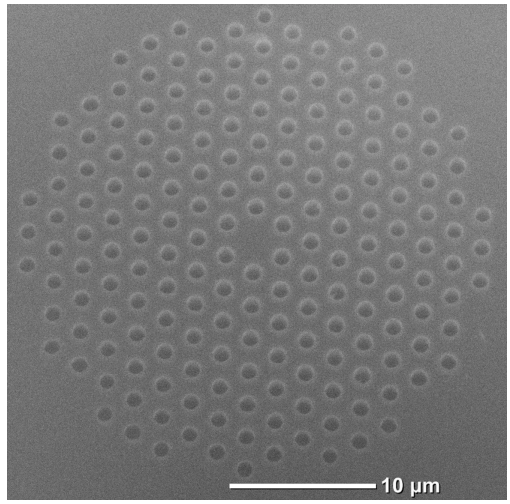

Figure 2.1: SEM image of the end facet of the "Extreme" PCF. Air holes are placed in hexagonal pattern in SiO_2 around a solid SiO_2 core.

end facet of a PCF is shown in Figure 2.1. The geometry of the PCF is defined by the hole diameter and the distance between holes (pitch). The two PCFs will be denoted "Extreme" (pitch = 2600 nm, pitch-to-hole ratio = 0.52), and "ANDi" (pitch = 1440 nm, pitch-to-hole ratio = 0.39). The geometry parameters for the "ANDi" fiber were given in [22]. All of the frequency dependent parameters are shown in Figure 2.2. In general, the refractive index, nonlinear refractive index, fiber material loss, and the Raman gain will have to be measured in order to accurately simulate pulse propagation using the GNLSE. Luckily, these parameters were available in the literature in most cases for the fiber materials that I considered, and otherwise assumptions could be made to approximate them.

Naturally, the ideal approach is to measure the input parameters. However, as it can be laborious and tedious, it is often more practical and sufficient to estimate or calculate

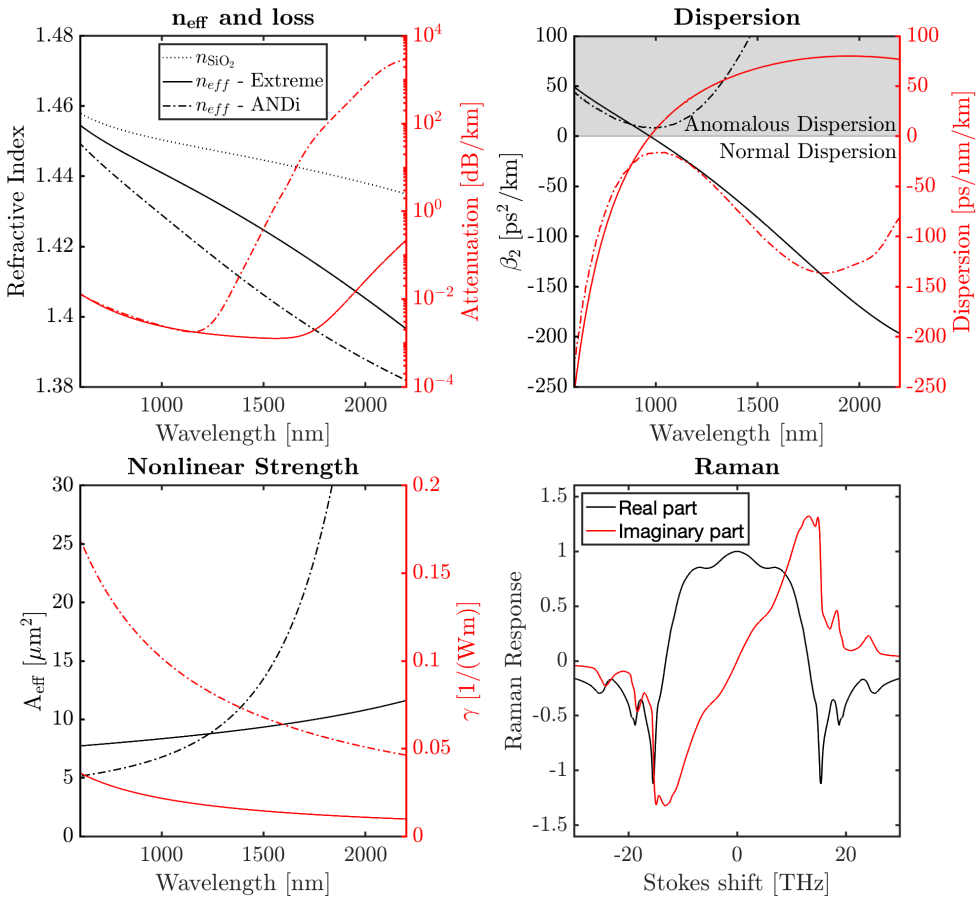

Figure 2.2: Input parameters for simulating the two silica PCFs "Extreme" (solid lines) and "ANDi" (dashed).

the parameters based on other peoples work. The following list will go through this procedure:

- $n_{eff}(\Omega)$: The effective index can be calculated by solving the transverse problem of the optical fiber [23]. This can be done for an arbitrary fiber geometry with finite element modelling (FEM), which in this work was performed with COMSOL. The refractive index of the fiber materials must be known. For the two example PCFs, the only needed material index is that of silica, assuming that the refractive index of air is 1, which is a good assumption in the for visible and near IR light. The refractive index of silica glass can be obtained from a Sellmeier equation provided in [24] [4].

[4] A good resource to find the refractive index of many material is given on refractiveindex.info

For a step-index fiber this can be done much more efficiently using analytical results (see for example chapter 9 in [23]). The biggest shortcoming of the analytical result is that the cladding is assumed infinite, such that confinement loss cannot be taken into account. Confinement loss is the light that leaks out of the the fiber due to poor confinement. Unless otherwise specified, the core refractive index, n_{co}, of all step-index fibers has been obtained from a Sellmeier equation, while the cladding refractive index, n_{cl}, is found by assuming a constant numerical aperture (NA), such that it is simply given by

$$n_{cl} = \sqrt{n_{co}^2 - \mathrm{NA}^2}. \tag{2.4}$$

While the effective index is the input parameter for the simulations it is not easy to interpret. Therefore the dispersion, D, or frequency dependent version of β_2, are usually reported instead

$$D = -\frac{\lambda}{c}\frac{\mathrm{d}^2 n_{eff}}{\mathrm{d}\lambda^2} = -\frac{2\pi c}{\lambda^2}\beta_2 \tag{2.5}$$

The spectral point where $D = 0$ is called the zero dispersion wavelength (ZDW). Due to the significant difference between the dynamics in normal and anomalous dispersion, the position of the ZDW plays an important role in SC generation. One of the remarkable feats of PCFs is the ability to engineer the dispersion properties of the fiber [25]. Experimentally, the dispersion is typically what is measured, rather than the effective index. A dispersion measurement can, for example, be done with the technique given in [26].

Through Eq. 2.5 it is technically possible to obtain the effective index from the dispersion by integrating twice, however this introduces two unknown integration constants. The effective propagation constant, $\beta_{eff}(\Omega, \Omega_p, \Omega_0)$ is independent of the integration constants, so the only place to be careful is in $\gamma(\Omega)$, which depends on the effective index and the slope of it.

Both the material index and the effective indices, and dispersion (both D and β_2) of the two fibers are shown in Figure 2.2. The most notable difference between the two fibers is that the "ANDi" fiber has normal dispersion in the entire transmission band, which is where the name all normal dispersion fiber comes from.

- $\alpha(\Omega)$: The fiber loss is generally available to some extent in the literature, or from the website of the fiber manufacturers. If one uses the material loss, rather than a measured loss curve for the specific fiber, it can be necessary to obtain the confinement loss through FEM analysis as well. These two contributions to the loss are directly added together. For the example fibers, the material loss was taken from a parametrisation given in [27] [5].

  For the ANDi fiber the effect of confinement loss is evident in Figure 2.2, where the loss sharply starts deviating around 1200 nm from the material loss of the Extreme fiber.

[5] There is an error in the provided parametrisation, the parameter λ_{ir} is reported as 478 μm it should be 47.8 μm

- A_{eff}: The effective area is also found by solving the transverse optical fiber problem. The effective area and the nonlinear strength are shown in Figure 2.2. The light is squeezed to a much smaller area in the ANDi fiber than in the extreme fiber, up to the wavelength where the light cannot be properly confined in the core. This point is also apparent in the loss curve as the point where confinement loss kicks in. Note that the effective area appears in the factor $K(\Omega)$ as well as in $\gamma(\Omega)$. The frequency dependence of the effective area is called mode profile dispersion. The implementation of mode profile dispersion was given in [28], where it was shown that it has the benefit that the photon number,

$$P_n \propto \int \frac{n_{eff}(\Omega)|G(\Omega,z)|^2}{\Omega} \mathrm{d}\Omega, \tag{2.6}$$

  is a conserved quantity, when fiber loss is disregarded. This allows efficient debugging of the code.

- $\tilde{h_R}(\Omega)$: When searching the literature for the Raman response, it will most often be the Raman gain, $g_R(\Omega)$, that is provided. The Raman gain can be converted into the Raman time response through the relation [6]

$$h_R(t) = \frac{3P_F\Theta(t)c}{4\pi\Omega_p f_R n_2} \int_0^\infty g_R(\Omega)\sin(\Omega t)\mathrm{d}\Omega \tag{2.7}$$

  Where P_F is a factor that depends on the relative input polarisations of the pump and signal of the light sources used to measure the gain. $P_F = 1$ for parallel polarisations, $P_F = 10$ for orthogonal polarisations, and $P_F = 2$ if either or both light sources are unpolarised [29]. $\Theta(t)$ is the Heaviside function, and Ω_P is the pump frequency.
  The full Raman response (both real and imaginary part) can be obtained by Fourier transforming equation 2.7, and the fractional Raman response, f_R is found by normalisation of equation 2.7:

$$\int_{-\infty}^{\infty} h_R(t)\mathrm{d}t = 1. \tag{2.8}$$

  The full Raman response of silica [16] is also given in Figure 2.2. This is the only frequency dependent input parameter that is independent of the fiber geometry and therefore only depends on material properties.

With a numerical model, numerical implementation, and simulation parameters at hand the last piece is the nonlinear effects, which will be covered in the next section.

2.4 Nonlinear Effects in the GNLSE

Based on the two example fibers and their parameters, given in the previous section, the nonlinear effects that are important for the remainder of the thesis will be introduced

[6] This relation is hard to find in the literature, but a derivation of it is given in an appendix in [18]

in this section. Simulated results will be presented in three different ways: The power spectral density (PSD) can be plotted as a function of wavelength λ. The PSD is given by

$$\mathrm{PSD}(\lambda, z) = \frac{c|G(\lambda, z)|^2 \mathrm{RR}}{\lambda^2} \tag{2.9}$$

Where RR is the repetition rate of the laser, which in this case, is assumed to be 80 MHz. Typically, a running average will be applied to the PSD to make the results more easily comparable to a spectrum measured using an optical spectrum analyser (OSA). A running average whit a step size of 1 nm and a bandwidth of 5 nm was applied on the PSD. The second way the results will be illustrated is by mapping the PSD to a colourscale as a function of both wavelength and propagation length. Finally, the most detailed description of the pulse is given in spectrograms, which are calculated as a windowed Fourier transform of $G(t, z)$. All spectrograms in this work are calculated with a Gaussian, $\exp\left(-t^2/(2\sigma^2)\right)$, window. The window width σ should always be reported as it has a direct influence on the appearance of the spectrogram.

In Figure 2.3, the propagation in 1.5 meters of Extreme fiber, followed by 0.25 meters of ANDi fiber is shown. For a more clear visualisation of the effects in the ANDi fiber, the loss in this one has been set to zero. Furthermore, the nonlinear refractive index has been set to $10.4 \cdot 10^{-20}\ \frac{\mathrm{m}^2}{\mathrm{W}}$ to make the SPM and OWB more pronounced. Generally, the value $2.6 \cdot 10^{-20}\ \frac{\mathrm{m}^2}{\mathrm{W}}$ will be used for silica, as it falls within the range of measured values that are reported in [16]. For silica the fractional Raman response is $f_R = 0.18$. All other fiber parameters for this simulation are given in Figure 2.2.

The input pulse is a bandwidth limited Gaussian shaped pulse, with 7 ps full width at half maximum (FWHM) in intensity, centred at 1064 nm, and with 10 kW peak power. The simulation uses 2^{19} grid points, a temporal resolution of 0.92 fs and a grid central wavelength, Ω_0, of 461.22 nm. By order of appearance, starting from the bottom in the spectral dynamics in Figure 2.3, the nonlinear effects are:

- **Modulational instability:** In the regime of ps pulse duration or longer, modulational instability (MI) appears in the anomalous dispersion regime [30]. In the spectrogram entitled MI in Figure 2.3, the appearance of MI is visible. The high power centre part of the pulse is broken up, and a spectral side lobe appears on each side. This process can also occur multiple times, such that each side lobe create new ones.

- **Soliton generation and dynamics:** Still in the anomalous dispersion regime, the remnants of the input pulse as well as the side lobe generated by MI can be considered a "sea" of light from which solitons emerge. The solitons of order 1 are relatively stable, and they start interacting with each other and the medium. The spectral evolution shows rapid spectral broadening at this point.

- **Dispersive wave generation:** Each generated soliton create a phase matched dispersive wave (DW) across the ZDW, that stay phase matched through an effect called radiation trapping [31].

- **Raman redshift:** Raman scattering in SC generation primarily allows an energy transfer of light to longer wavelengths. This occurs for different frequency components with a temporal overlap, or through amplification of quantum noise, which can limit the noise performance of ANDi SC generation [32]. Importantly, the non-zero Raman response at low frequency shifts in silica allows solitons to Raman redshift through an interaction with itself in a process called soliton self-frequency shift (SSFS) [33]. SSFS and the corresponding blue-shift of the trapped DWs continue until the solitons lose their energy, for example at the IR loss edge.

- **SPM and OWB:** In the last 25 cm of the spectral evolution, the fiber parameters are changed to those of the ANDi fiber. After 1.5 m of propagation in the Extreme fiber, there are a lot of spectrally and temporally distributed solitons. These have high peak power and short pulse durations. However, when coupled into the ANDi fiber, the soliton is no longer a stable solution, which means that the phase shift, and accompanying spectral broadening due to SPM, is no longer cancelled out by the dispersion. The two top spectrograms show a zoom-in of four solitons at the output of the extreme fiber, and after 1 cm of propagation in the ANDi fiber. SPM appears as the initial spectral broadening. At some point the spectral edges have temporally shifted due to dispersion, such that they temporally overlap with the input pulses. At this point, energy is transferred from the centre of the pulse past the spectral edges in a process called optical wave breaking (OWB) [7]. SPM and OWB are the two most important nonlinear processes in the coherent supercontinuum that can be generated in ANDi fibers [22, 32].

The output of both fibers is shown on top of the spectral evolution. This illustrating example has resulted in a SC which spans from 500 nm to 2400 nm.

Two applications of the GNLSE are shown in the next chapter. The applications highlight how simulations act as an excellent tool to optimise SC generation, and to test the impact that fiber parameters has on the nonlinear dynamics without the need for laborious experiments.

[7] Optical "wave breaking" is one of two analogies to oceanic waves that are occurring in this thesis, the other being rogue waves. In fiber optics, there is no "breaking" of the wave as is known for oceanic waves on the beach, it rather describes the steepening in the leading edge of the pulse, which in the case of fiber optics leads to an energy transfer between different spectral components

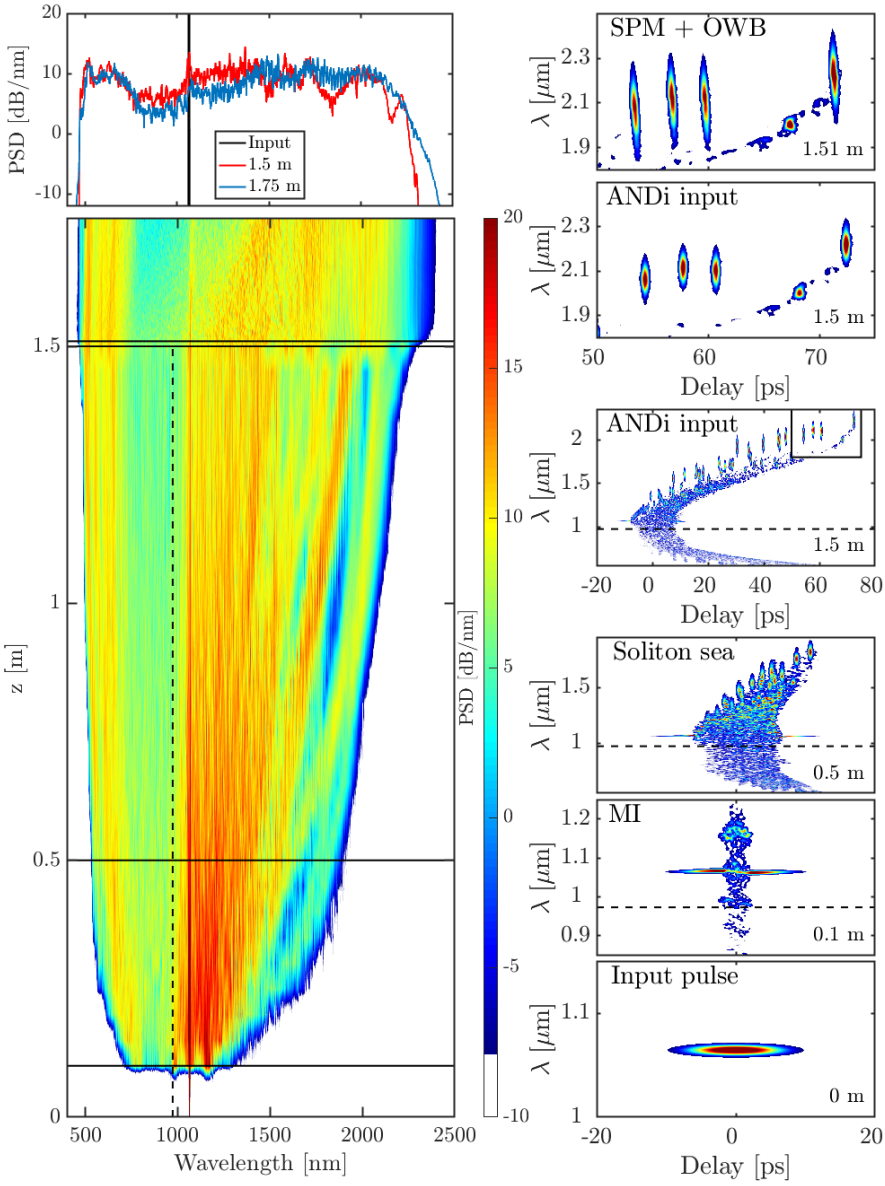

Figure 2.3: The nonlinear effects in the example case of SC generation. **Left)** The spectral evolution in 1.5 meters of Extreme fiber, and 25 cm of ANDi fiber. At the top the input to the extreme fiber as well as the spectrum at the output of both fibers are shown. The dashed vertical line shows the ZDW in the Extreme fiber. **Right)** Series of spectrograms, using a window width of 200 fs indicating the spectral-temporal composition at the points indicated by horizontal black lines in the spectral evolution, including $z = 0$.

CHAPTER 3
Applications of the GNLSE

The two sections of this chapter are dedicated to some of the results purely based on solving the GNLSE. In section 3.1 results from paper [IV] will be described. In this work we showed that a flatter blue part of a supercontinuum spectrum can be achieved by modulating the peak power of the input pump pulses into 2-3 sub-pulses. In section 3.2, results from paper [V] will be described. In this work, simulations of SC generation were used to illustrate the effect of a modulated dispersion in SC. These two applications show the wide range of systems that can be investigated with the GNLSE. Furthermore they underline the potential for doing optimisation and predictions before doing laborious experiments.

3.1 Flat Blue SC Spectrum Through Pump Modulation, Paper [IV]

The first pure application of the GNLSE is a pump modulation scheme to generate a flatter blue part of the spectrum in the PCF denoted "Extreme" in Chapter 2. A more flat blue part of the spectrum, under the constraint of some minimum PSD, can be beneficial for many applications that use the blue part of an SC source, including confocal microscopy [12], and visible light OCT [34–36].

Tailoring of SC spectra through fiber design and pump modulation has been an active field for more than two decades. In 2001 a genetic algorithm and a spatial light modulator were used to achieve active feedback control of nonlinear pulse propagation [37]. Later works used machine learning and similar active control to favourise specific parts of an SC spectrum [38], which allowed to tailor an SC spectrum for fluorescence microscopy [39]. In [40] pump modulation was applied to broaden the DW peak in ultraviolet (UV) and blue SC generation in gasfilled hollow-core fibers - a work which was targeted for applications within scatterometry such as described in [41].

In our work a simple pump modulation scheme is considered, where the peak power of 2-3 consecutive pulses is modulated without any feedback. We go one step further and show the influence that pump modulation has on the relative intensity noise (RIN), particularly we show that the flatness comes at the expense of slightly increased RIN.

In section 2.4, the dynamics in this system was described in great detail, but it is worth reemphasising that the spectral edge in the IR is set by the loss edge, as solitons stop redshifting through SSFS when they lose too much power. Interestingly, the blue edge is not set by the loss, but rather by the phase matching wavelength to the solitons

on the red edge.

All the necessary fiber parameters in this application are those given for the Extreme fiber in Figure 2.2, and the numerical grid is exactly the same as the one in Figure 2.3. However, the pulse parameters are not exactly the same. In this work a bandwidth limited 7 ps FWHM duration in intensity, Gaussian pulse with a centre wavelength of 1064 nm is considered. A repetition rate of 80 MHz has been assumed in the unmodulated case to calculate the PSD. This corresponds to an input average power of approximately 6.6 W. Fifty simulations have been performed for all input peak powers between 4 and 11 kW in steps of 1 kW, and both 1% RIN and one-photon-per-mode noise [42] are added at the input.

A simulation of a pulse with 11 kW peak power propagated in an 8 m piece of fiber is considered the baseline that all the following results are compared to. The specific measure that is optimised is the flatness:

$$\text{flatness} = F = \frac{\max(\text{PSD}) - \min(\text{PSD})}{\max(\text{PSD}) + \min(\text{PSD})} \tag{3.1}$$

The flatness is optimised in the range $455 - 650$ nm under the constraint of raising the min(PSD) of the baseline. Simultaneously, the RIN and the spectrally averaged RIN (SRIN) are calculated according to:

$$\text{RIN}(\omega, M) = \frac{\sigma(\omega)}{\mu(\omega)}, \quad \text{SRIN}(M) = \frac{\int \sigma(\omega)\mathrm{d}\omega}{\int \mu(\omega)\mathrm{d}\omega}, \tag{3.2}$$

where $\sigma(\omega)$ is the spectrally resolved standard deviation, and $\mu(\omega)$ is the spectrally resolved mean. The parameter M refers to the number of pulses in one cycle in the modulated pulse train, and it is introduced to create a systematic way to compare the RIN between unmodulated and modulated pulse trains. Therefore, $M = 1$ for an unmodulated pulse train, such that the definition in equation 3.2 is reduced to the standard measure of pulse to pulse RIN. For $M > 1$ the RIN is calculated by directly adding the PSD of the different pulses in the modulation scheme. As such, the RIN is no longer calculated on a *pulse-to-pulse* level but rather *cycle-to-cycle*. Therefore, when comparing the RIN between different modulation schemes, a fair comparison should instead be between $\sqrt{M_1} \cdot \text{RIN}(\omega, M_1)$ and $\sqrt{M_2} \cdot \text{RIN}(\omega, M_2)$.

When a pulse modulation scheme using a cycle of three pulses is considered, the optimum configuration will sometimes have two pulses of the same input peak power. In this case, 50 additional simulations have been performed with this input peak power, as the spectra will otherwise be correlated, which will falsely lower the calculated RIN.

Two approaches to pulse modulation will be considered; in section 3.1.2 it will be shown that improved flatness cannot be achieved without increasing the average power, and in 3.1.3 the two and three pulse modulation schemes show significant improvements to flatness when increasing the average power. First, the baseline will be introduced in section 3.1.1.

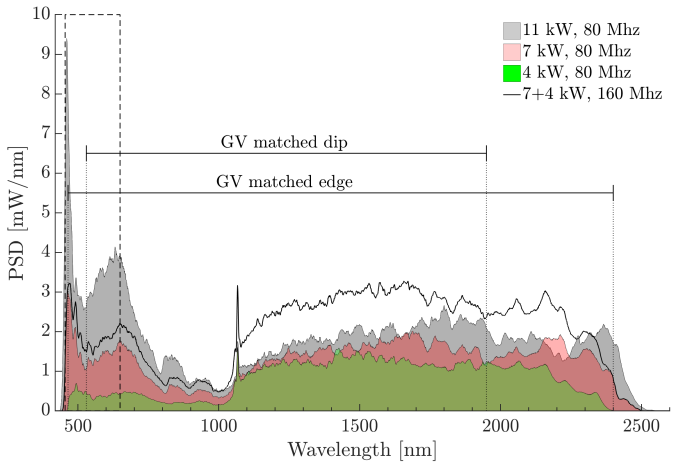

Figure 3.1: PSD of the baseline (grey), a 7 kW peak power input pulse (red), and 4 kW peak power input pulse (green). The black line shows the sum of the 7 kW and 4 kW spectra. The dashed rectangle in the blue edge of the spectrum shows the region in which the flatness will be optimised. The two scale bars show two sets of phase matched wavelengths.

3.1.1 Baseline

Figure 3.1 shows the full simulated spectrum of the baseline. The spectrum spans approximately 450 nm to 2500 nm. However, the targeted region for improving flatness is only in the range $455 - 650$ nm as indicated by the dashed rectangle. The baseline has a min(PSD) of 2.54 mW/nm, and a max(PSD) of 9.40 mW/nm, which gives a flatness of 0.574.

Two sets of group velocity matching conditions are shown by scale bars. The blue edge of the spectrum is phase matched to the IR loss edge, while the dip in the spectrum that should be filled out to improve the flatness is phase matched to light at 1950 nm. In order to fill out this dip some of the solitons undergoing SSFS should be stopped before redshifting further. This can be achieved by decreasing the input peak power, or by using a shorter fiber - both of these approaches will be explored.

3.1.2 Modulation at constant average power

When using simple repetition rate doubling to 160 MHz at constant average power, only two configurations are possible from the generated data set: $7 + 4$ kW and $6 + 5$ kW. The sum of 7 kW and 4 kW peak power input pulses, is shown as the black curve in Figure 3.1. This combination of pulses does not achieve a higher min(PSD) than the baseline. However, if this constraint is disregarded the flatness is actually improved to a value of 0.436. This motivates that better flatness is possible, if the repetition rate was not constrained by doubling or tripling but rather set free. A tunable repetition rate can, for example, be achieved with a directly modulated diode laser. Optimisation under no constraint on the repetition rate is considered in section 3.1.4.

The constituents are shown as red (7 kW) and green (4 kW). The spectrum when pumping with the 4 kW peak power input pulse does not reach the 455 nm target and neither does a 5 kW or 6 kW peak power input pulse. Therefore, no configuration using constant average power satisfies the constraint of achieving a higher min(PSD).

3.1.3 Modulation at increased average power

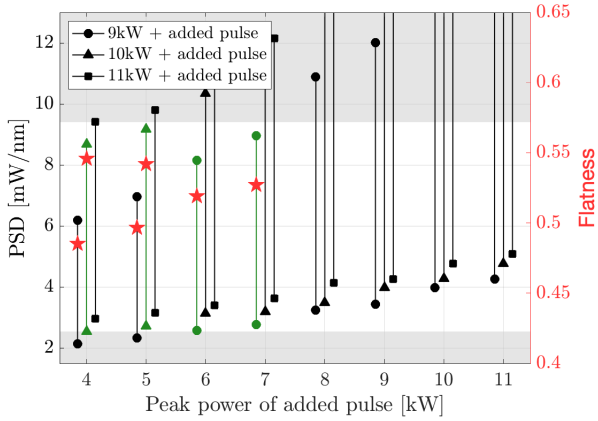

Figure 3.2: Linked min and max PSD (left y-axis), and flatness (right y-axis) when using a two pulse modulation scheme in an 8 m long fiber. On the x-axis the input peak power of one of the pulses is indicated, while the input peak power of the other is indicated by either circles (9 kW), triangles (10 kW), or squares (11 kW). The region with a white background is within the boundaries set by the min(PSD) and max(PSD) of the baseline. All pulse configurations with min(PSD) higher than the baseline and an improved flatness are marked in green, while all others are marked in black. The configurations with an improved flatness compared to the baseline have their flatness indicated by a red star.

The simplest case of modulation using a two pulse scheme at a fiber length of 8 m is first considered. The results are shown in Figure 3.2. The x-axis shows the input peak power of one of the pulses, while the input peak power of the other pulse is indicated by the shape of the markers as shown in the legend. The min(PSD) and max(PSD) are shown using linked markers in each case. A total of four configurations, indicated by green markers, achieve a range of PSD values within the boundaries set by the baseline. The lowest flatness among these four cases is 0.519 (marked by red starts, and read on the right y-axis), and it is achieved by using $P_0^{(1)} = 6$ kW and $P_0^{(2)} = 9$ kW. If the requirement on the min(PSD) is disregarded the lowest achieved flatness is 0.485, and it is achieved with $P_0^{(1)} = 4$ kW and $P_0^{(2)} = 9$ kW. On top of the improved flatness the pump peak power is lower than in the baseline, which could potentially lead to reduced fiber degradation.

When the fiber length is also a free parameter, as is the case in Figure 3.3, the results become even more interesting. As the parameter space is now a lot larger,

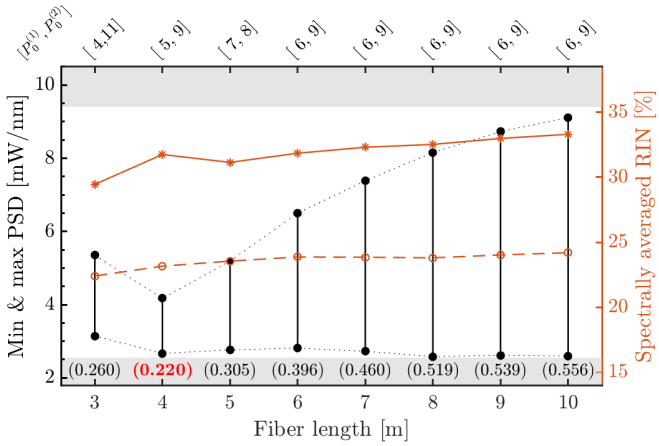

Figure 3.3: Linked min and max PSD (left y-axis) of the optimum pulse configuration as a function of the fiber length in a two pulse modulation scheme. The region with a white background is within the boundaries set by the min(PSD) and max(PSD) of the baseline. The pulse configuration is written above the chart, while the achieved flatness is written in the bottom of the chart. The optimum flatness is marked in red. The spectrally averaged RIN of the baseline (dashed) and optimum pulse configuration (solid) at each length is given on the right y-axis.

only the pump pulse configuration that gives the best flatness is shown for each fiber length. The two optimum pump pulse peak powers at each length are shown above the plot, and the achieved flatnesses are written in the bottom part of the figure. The flattest spectrum, with a flatness of 0.22, is achieved after 4 m of propagation by using $P_0^{(1)} = 5$ kW and $P_0^{(2)} = 9$ kW. Generally, a much improved flatness can be achieved compared to the baseline by choosing a shorter fiber length. However, the flatness is mostly improved by lowering the maximum PSD - not by raising the minimum. The SRIN of the baseline has been divided by $\sqrt{2}$ to show a fair comparison. When the scaling is taken into account, the SRIN of the modulated pulse train is higher than the baseline in all configurations.

In Figure 3.4, the same analysis as in Figure 3.3 has been done for the case of three modulated pulses in each cycle. The linked min(PSD) and max(PSD) of the optimum cases are once again shown on the left y-axis, while the right y-axis shows the SRIN. The slightly more complicated pulse modulation scheme is worthwile as an even better flatness of 0.183 is obtained. The optimum configuration has 4 m of fiber and the pump pulse peak power configuration: $P_0^{(1)} = 5$ kW, $P_0^{(2)} = 6$ kW, and $P_0^{(3)} = 11$ kW. Interestingly, the flatness is not achieved only by reducing the max(PSD), but also by raising the min(PSD). Thus, a min(PSD) of 4.6 mW/nm is obtained, which is 81 % higher than the min(PSD) of the baseline. The RIN of the baseline has been divided by a factor of $\sqrt{3}$ in this case for a fair comparison, and once again the flatter spectrum comes at the expense of a higher RIN than the baseline.

The final spectra of the baseline and the optimised modulated pulse trains are shown

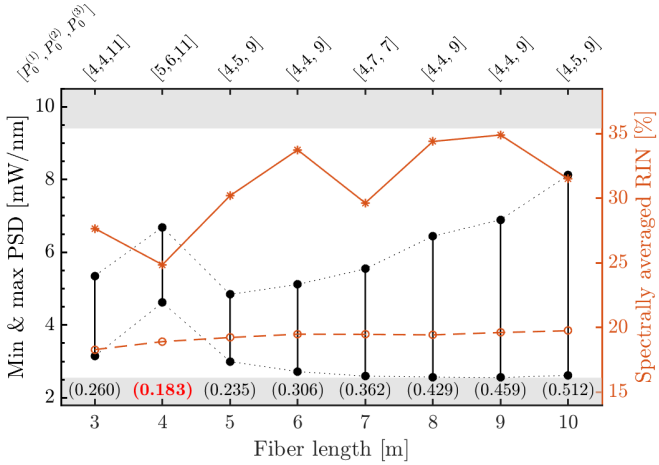

Figure 3.4: Linked min and max PSD (left y-axis) of the optimum pulse configuration as a function of the fiber length in a three pulse modulation scheme. The region with a white background is within the boundaries set by the min(PSD) and max(PSD) of the baseline. The pulse configuration is written above the chart, while the achieved flatness is written in the bottom of the chart. The optimum flatness is marked in red. The SRIN of the baseline (dashed) and optimum pulse configuration (solid) at each length is given on the right y-axis.

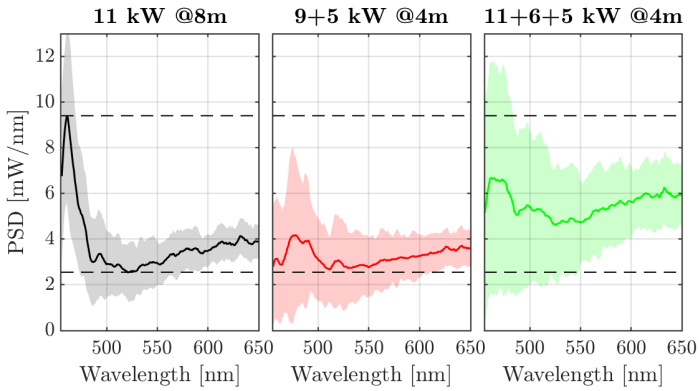

Figure 3.5: The three optimised spectra for the unmodulated, two pulse, and three pulse modulation schemes, respectively. The solid lines indicate the average PSD, while the shaded areas show $\mu(\lambda) \pm \sigma(\lambda)$. The dashed lines show the min(PSD) and max(PSD) of the baseline.

in Figure 3.5. The shaded areas signify the confidence intervals given by $\mu(\lambda) \pm \sigma(\lambda)$. In this figure, the RIN of the two pulse modulation scheme has been multiplied by $\sqrt{2}$ and the three pulse modulation scheme by $\sqrt{3}$. Figure 3.5 shows clearly that the improved flatness in the two pulse modulation scheme comes from removing the high DW peak close to the blue edge, where the 3 pulse modulation scheme also manages to raise the entire spectrum.

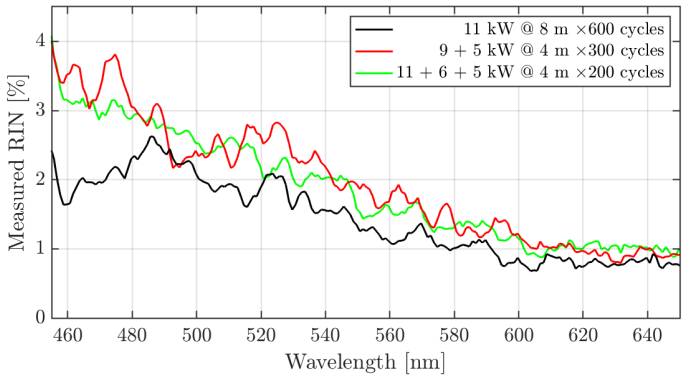

Figure 3.6: The RIN spectra in the unmodulated and optimised configurations, that would be measured in a spectrometer based experiment using a constant integration time, such that 600 cycles are measured in the unmodulated case.

In a real spectrometer based application, the integration time of the spectrometer will result in averaging of output pulses. This introduces the concept of "measured RIN" which differs from the pulse-to-pulse RIN by a factor of $1/\sqrt{N}$, where N is the number of pulses that is averaged over. This consideration allows an apparent reduction of the RIN of a laser source by increasing the repetition rate of the laser. To illustrate this, the measured RIN is shown in Figure 3.6 for a spectrometer based application that averages over 600 pulses of the baseline laser source. 600 pulses of the baseline laser source corresponds to 300 cycles of the 2 pulse modulation scheme and 200 cycles of the 3 pulse modulation scheme. The full RIN curves show that the most significant difference between the baseline and the modulation schemes in terms of noise performance comes close to the blue edge of the optimised region. This is probably due to the fact that the reduced fiber length only allows very few DWs to reach the blue edge of the spectrum for the 11 kW input pulses and none of the 5 kW or 6 kW in the three pulse modulation, and similarly for the two pulse modulation scheme.

3.1.4 Free repetition rate

So far, the repetition rate has been fixed by pulse rate doubling or tripling of an 80 Mhz pump laser. However, it is interesting to consider if a lower flatness can be achieved if the flatness is a free parameter that can simply be scaled to achieve the same min(PSD) as the baseline.

In Table 3.1 the optimum cases using three pulses in the pump modulation scheme are shown for 3-10 m of propagation. Interestingly, the optimum configurations after 3, 4, 6, and 7 m of propagation remain the same even when an arbitrary repetition rate is allowed. The overall optimum configuration remains the one achieved after 4 meters of propagation, which is the one illustrated as the green curve in Figure 3.5. The optimum configuration can achieve the same min(PSD) as the baseline using a

L [m]	3	4	5	6	7	8	9	10
F	0.260	0.183	0.229	0.306	0.354	0.403	0.453	0.481
RR [MHz]	194.7	132.6	287.7	225.0	394.5	398.4	406.4	181.8
$P_0^{(1-3)}$ [kW]	4,4,11	5,6,11	4,4,8	4,4,9	4,4,7	4,4,7	4,4,7	4,4,11
P_{avg} [kW]	9.18	7.24	11.42	9.49	14.69	14.83	15.13	8.6

Table 3.1: Optimum cases of the three pulse modulation scheme when the repetition rate is considered a free parameter, chosen such that the min(PSD) reaches that of the baseline. F is the flatness, RR the required repetition rate, and P_{avg} is the resulting average power of the input laser.

repetition rate of 132.6 MHz, resulting in an increase in input average power of only 9.7 %. This means that the flatness can be achieved at an average power that is typical for the MI and soliton based laser sources as produced by, e.g, NKT Photonics [1].

In the remaining cases new optimum configurations are found. The optimum case after 5 m has a flatness of 0.229. This is achieved while the highest input peak power in the modulation scheme is only 8 kW. Similarly, after 8 meters of propagation, the optimum pulse combination does not include an input pulse with a higher peak power than 7 kW - both of these cases would be very interesting in terms of reduced fiber degradation, while still offering a significant improvement in flatness compared to the baseline. However, it comes at the expense of almost 300 MHz, and almost 400 MHz repetition rates, respectively, while also requiring much higher input average powers of 11.42 kW, and 14.83 kW, respectively.

3.1.5 Discussion and outlook

For specific applications one might consider different measures of flatness. Two other possible choices are:

$$\text{(i)}\ \frac{\sum_i |\mathrm{PSD}(\lambda_i) - \overline{\mathrm{PSD}}|}{\sum_i \mathrm{PSD}(\lambda_i)} \quad \text{(ii)}\ \frac{\exp\{\frac{1}{N}\sum_i \ln \mathrm{PSD}(\lambda_i)\}}{\frac{1}{N}\sum_i \mathrm{PSD}(\lambda_i)}, \tag{3.3}$$

where $\overline{\mathrm{PSD}}$ refers to the average value of the PSD. They each have specific strengths and weaknesses. For example, the flatness measure in equation 3.1 would result in very poor flatness for a flat spectrum with just one spectral point that is significantly higher or lower than the rest. Both measures in 3.3 would show excellent flatness in this case. However, both measures agree with the applied flatness measure that the optimum configuration comes after 4 m of propagation with the pulse configuration $P_0^{(1-3)} = 5, 6, 11\mathrm{kW}$.

A lot of other measures than the flatness in a specific wavelength range can be improved using a similar analysis - and even using the same simulated data set. Such measures include: High PSD at a specific wavelength, broadest spectrum with a certain

[1] Their website: https://www.nktphotonics.com/products/supercontinuum-white-light-lasers/superk-fianium/

limit between the max(PSD) and the PSD at each wavelength, and obtaining as high as possible PSD in some spectral region. Finally, the flatness can be improved even more if increasingly complicated modulation schemes are considered. Two such examples are a flatness of 0.294 using an 8 m fiber by modulating using one 11 kW peak power input pulse and nine 4 kW peak power input pulses, and a flatness of 0.1605 of using a 4 m fiber with a pulse configuration $P_0^{(1-4)} = [11, 6, 5, 4]$ kW.

3.2 Spectral Dynamics in Modulated Dispersion Chalcogenide Fiber, Paper [V]

This section concerns the paper [V]. My contribution was to provide simulations of the GNLSE to investigate the potential impact on SC generation from the modulated dispersion in a highly nonlinear chalcogenide fiber.

A fiber with a 15 μm diameter As_2Se_3 glass core and a 420 μm diameter cladding made of polyethersulfone (PES) was drawn with two additional holes running through the length in which tungsten wires were inserted. These dimensions make the fiber heavily multi-moded in the considered wavelength range. The tungsten wires were added as a means of tuning the fiber properties through running a current through them. A 15 cm piece of this fiber was cleaved and polished. The dispersion of this piece of fiber was measured with low-coherence interferometry based on an NKT SuperK mid-IR supercontinuum source and a Mach-Zehnder interferometer [26]. The dispersion showed a strong dependence on the electrical power level in the tungsten wires, resulting in strong oscillations with an electrical power dependent amplitude and period. An approximation to the dispersion as used in the simulations with no current (blue) and with current (orange) is shown in figure 3.7 (a).

No definite explanation of the modulated dispersion was obtained. However, many effects were excluded: The oscillations were independent of whether the current was run in parallel or anti-parallel directions in the wires, which excluded influence of magneto-optic effects or strain induced by the magnetic fields. Furthermore, the oscillations did not occur when simply heating the fiber using a heating plate which ruled out purely temperature-dependent effects.

No matter the origin of the oscillations, it was interesting to investigate what impact such oscillations would have on supercontinuum generation. For this purpose, all the input parameters for GNLSE simulations, described in section 2.3, were needed. The effective index was calculated using COMSOL, where the core index, n_{co}, was obtained from the Sellmeier equation in [43]. The numerical aperture (NA) was assumed to be NA $= 2.5$ and the cladding index n_{cl} was assumed to follow the expression

$$n_{\mathrm{cl}} = \sqrt{n_{\mathrm{co}}^2 - \mathrm{NA}^2} + 10i \tag{3.4}$$

The imaginary part signifies loss in the PES cladding, and it was treated as a fitting parameter to match the measured ZDW of 4.725 μm (extrapolated from measured data) at room temperature.

An effective refractive index that results in an oscillating dispersion was then created by adjusting the non-oscillating effective refractive index by

$$n_{\mathrm{eff\ -\ oscillating}} = n_{\mathrm{eff-nonoscillating}} + \sum_{i=1}^{2} a_i \cos\left(\frac{2\pi\lambda}{\Lambda_i} + \phi_i\right)/\lambda \tag{3.5}$$

Where the coefficients were $a_1 = 1.5 \cdot 10^{-5}$, $a_2 = 7.5 \cdot 10^{-6}$, $\Lambda_1 = 300$ nm, $\Lambda_2 = 600$ nm, $\phi_1 = \pi$, and $\phi_2 = 0$. These coefficients were simply chosen to make qualitative correspondence to the measured curves.

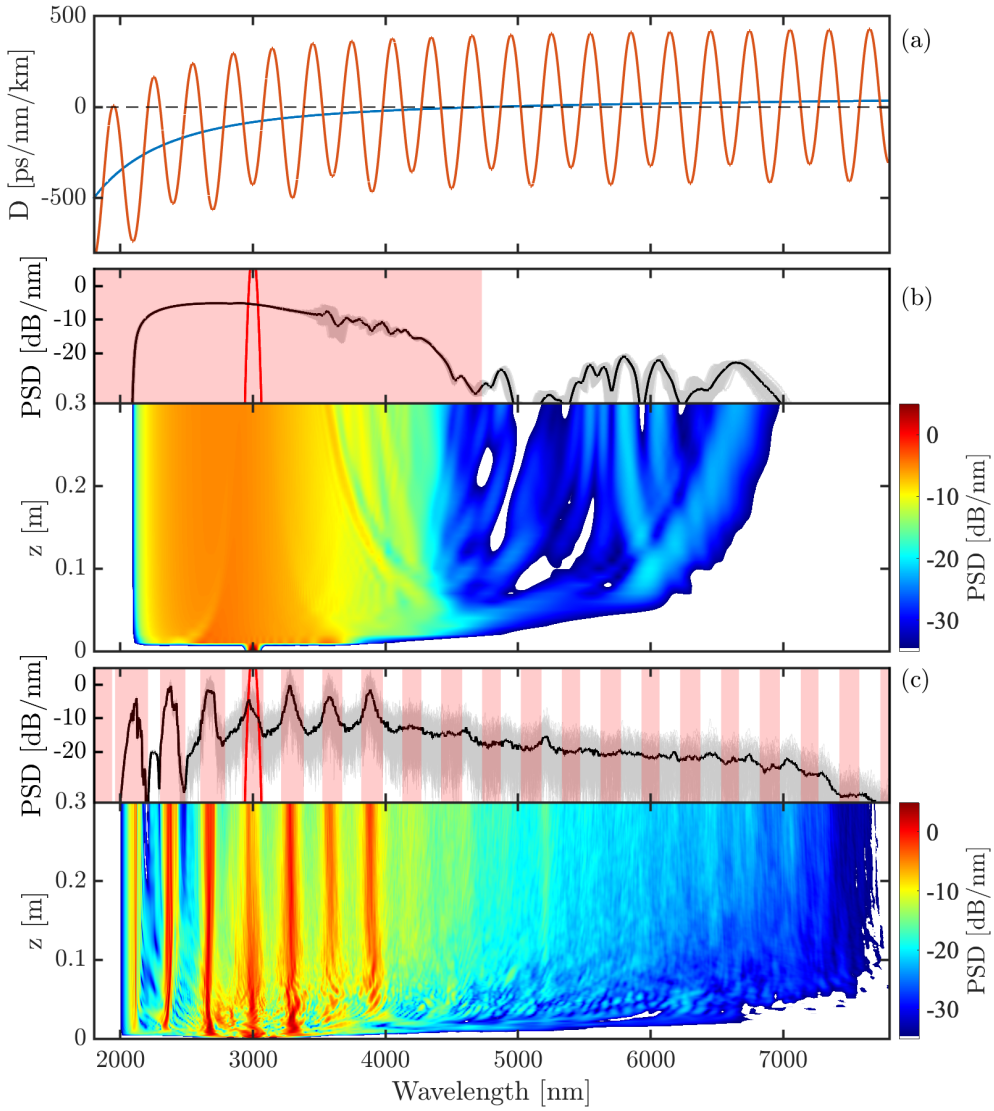

Figure 3.7: (a) The dispersion of the simulated fibers. (b) The spectral evolution of the fiber when no voltage is applied with the input (red) and average output (black) spectrum shown on top. (c) The spectral evolution in the fiber when the dispersion is modulated with the input (red) and average output (black) spectrum shown on top. In both (b) and (c) the grey curves signify each individual simulation, and the red-shaded background shows spectral ranges with normal dispersion.

The nonlinear refractive index of As_2Se_3 is $n_2 = 1500 \cdot 10^{-20}$ m^2/W [16], and for simplicity the effective area was set to a constant value of $A_{\text{eff}} = 210$ μm^2. The Raman response and loss was assumed to simply be those of As_2Se_3 glass, as given in [44], and [45], respectively. And the fractional Raman response was calculated to be 0.0103, according to equation 2.8.

The input pulse is a bandwidth limited Gaussian with centre wavelength of 3 μm, 40 kW peak power, and a 1/e pulse duration in intensity of 250 fs. Laser noise with 1% RIN in intensity as well as one-photon-per mode noise [42] was added to the simulations. For statistics purposes, 60 simulations with different noise seeds were performed in both cases of dispersion. A repetition rate of 22 MHz was assumed for the PSD.

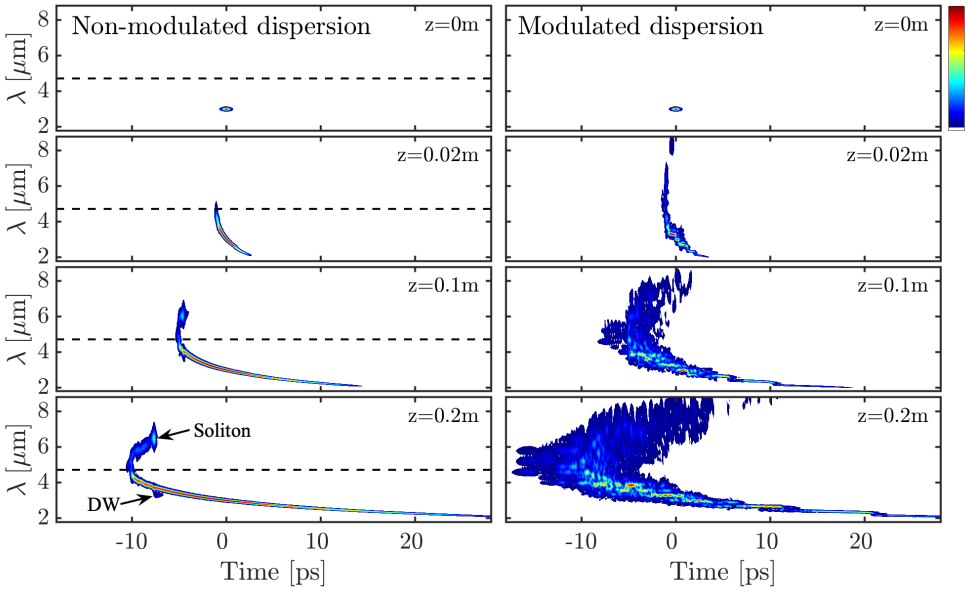

Figure 3.8: Spectrogram series for a single seed of the simulations in the non-modulated case (left) and modulated case (right). A window width of 100 fs was applied.

The results of the simulations are shown in Figure 3.7 (b) and (c) for the non-modulated and modulated dispersion, respectively. For further details, a series of spectrograms is shown for each case in Figure 3.8. In the case of non-modulated dispersion, the input pulse is in the normal dispersion regime. The strong peak power and non-linearity of the glass result in strong immediate SPM and OWB. Within few centimetres of propagation, power has moved across the ZDW and solitons are generated. These solitons create DWs in the normal dispersion, and spectral broadening happens through SSFS and DW trapping. As SPM and OWB are the initial dynamics that introduce spectral broadening, most of the spectrum is very stable. This can be seen from the fact that the grey lines that represent individual spectra of the 60 seeds coincide with the average. Only the soliton and corresponding DW dynamics show spectrally dependent differences in PSD between each input seed.

The dynamics in the modulated dispersion are remarkably different. The initial broadening is still very rapid. High peaks in the spectrum appear quickly in each normal dispersion band and stay there until the output of the fiber. The edges of the spectrum extend the range $2 - 8$ μm. However, the grey lines show that there is much more variation at the output between each individual input seed. The spectrograms show that the light is quickly temporally dispersed, and each peak in the PSD become quite broad temporally, such that the intensity is too low for further nonlinear effects.

The simulations highlight an extreme case of spectral shaping through dispersion control, and shows that active dispersion control, in this case induced by a current, can be used to actively change the nonlinear dynamics and lead to a tunable SC spectrum.

CHAPTER 4

Cascaded Supercontinuum Generation

Cascaded SC generation is the process of re-coupling an already generated SC into a fiber of another type of glass or geometry, in order to take advantage of different loss properties and nonlinear dynamics. In cascaded mid-infrared (IR) SC generation each subsequent fiber typically has an IR loss edge further into the mid-IR, such that the SC can be pushed towards longer wavelengths.

The mid-IR SC laser source is enabled by the development of glasses with a transmission band that reaches further into IR than the loss edge at approximately 2.5 μm of amorphous SiO_2. Two types of such glasses are considered in this work: Fluoride glasses and chalcogenide glasses.

SC spectra spanning past 4 μm can be generated in fluoride glass fibers. Typically, two types of fluoride glass are considered: In ZBLAN glass (ZrF_4-BaF_2-NaF-NdF_3), SC spectra spanning past 4 μm can be generated while handling more than 10 W of average power [46]. In InF glass fibers the loss edge is at slightly longer wavelengths. Although, the minimum loss in ZBLAN is lower, the longer wavelength loss edge of InF has, in one study, allowed an SC spectrum that spanned to 5.4 μm [47].

The chalcogens are the group 16 elements of the periodic table, but typically a chalcogenide glass only refers to glass containing one of the elements: Sulfur (S), selenium (Se), or tellurium (Te). Pure chalcogenide glasses transmit light far into the mid-IR (past 20 μm in Te glasses) with nonlinear refractive indices orders of magnitude higher than silica glass [48]. The specific chalcogenide glass fibers considered in this chapter are an $As_2S_3/As-S$ core/clad fiber from Art photonics GmbH with a reported loss edge close to 6 μm [49], a similar As_2S_3 based fiber from IRflex also with a loss edge close to 6 μm [50], and an As_2Se_3 based fiber from IRflex with a loss edge at approximately 10 μm [51]. Both IRflex fibers have loss curves published in [45].

Initially, broadband mid-infrared (IR) sources were achieved by direct pumping of chalcogenide glass fibers with high energy pulses, with quite a few examples of SC spectra well past 10 μm [15, 52, 53]. Simultaneously, cascaded SC generation was introduced. This approach to mid-IR SC generation is considered a promising approach to compact, high average power, and commercially viable mid-SC lasers [54]. Early results on cascaded SC generation with ns duration pulses showed spectra spanning

to the loss edge at approximately 4.5 μm of ZBLAN [55]. The first cascaded SC using chalcogenide fiber was reported in 2012, where a spectral edge of 4.8 μm was achieved at an average power of 565 mW [56] in an As_2S_3 fiber. A later work showed broadening up to 7 μm in a As_2Se_3 fiber, while highlighting the importance of the dispersion properties of the ZBLAN fiber for further cascading [57]. The importance of the dispersion of the ZBLAN fiber will be showcased multiple times in this chapter. The current state-of-the art cascaded mid-IR laser sources in terms of both spectral broadness and average power include a spectrum spanning to 10.5 μm with 86.6 mW average power [58], and a spectrum past 11 μm with 417 mW on-time average power at a duty cycle of 33 % [59].

In [I] we described an important redshifting mechanism, where significant energy is shifted towards the ZDW, when a soliton rich spectrum is coupled to normal dispersion in a highly nonlinear As_2Se_3 fiber. Furthermore, we showed the appearance of a novel type of optical "rogue wave". These results will be the focus of section 4.1.

Usually, the initial propagation is in anomalous dispersion in cascaded SC propagation, which means that the noise performance is heavily influenced by MI and soliton dynamics, assuming that the input pulse is ps or longer. The poor noise performance of such MI-based SC sources can often be detrimental to the intended applications. In OCT it has been shown that the use of a low noise ANDi source with 90 MHz repetition rate, instead of an MI based source with 80 MHz repetition rate, can lead to a 12 dB higher sensitivity at 1370 nm [60]. In spectrometer based applications, the high noise of conventional ps pulse based SC sources can be reduced by averaging over a high number of pulses, which can be achieved by increasing the repetition rate of the source. Still, a decrease in pulse-to-pulse RIN is highly desirable.

A few different approaches to achieve a decreased pulse-to-pulse RIN that are reported in the literature include: Aligning solitons and DWs at a second ZDW either in a uniform fiber, or by fiber undertapering as done in [19], seeding of MI [61], or spectral alignment through gain bands in active fibers [62]. In paper [III] we showed a novel type of noise reduction in cascaded SC generation in which a soliton rich SC is coupled into normal dispersion, such that the soliton is no longer a solution, which means they are instead spectrally broadened by SPM and OWB. Once the spectral tails of the broadened pulses overlap, the result is an averaging of PSD on an intra-pulse level, which results in efficient noise reduction. These results will be the topic of section 4.2.

4.1 Collective Redshift in Cascaded SC Generation and Normal Dispersion Rogue Waves, Paper [I]

The last purely numerical project that will be described in this thesis is the observation of a novel type of optical rogue wave that can appear in normal dispersion in cascaded SC generation. On the way to this result, a collective redshift of intrapulse sub-structures will be described. This collective redshifting can play a key role in generating SC sources further into the mid-IR. The results in this section are based on results published in paper [I].

The term optical rogue wave is analogous to oceanic rogue waves which are rare, high amplitude, ship-wrecking, oceanic waves [63]. The term optical rogue wave was first coined in 2007 [64], it was attributed to an L-shaped distribution of pulse energies, when measuring a narrow spectral band close to the red edge of the SC. These high-power waves have typically been observed in anomalous dispersion, where they appear from a high number of soliton collisions, and they were first observed in numerical work [65]. They have also been observed in normal dispersion, when the appearance of high power solitons create DWs across the ZDW, both numerically [66] and experimentally [67]. In many works, including the last two cited, the rogue wave is recognised by its high power compared to the remaining structures, as well as the L-shaped distribution of pulse energies. These are the two characteristics that are also used here to underline the rogue wave nature, as well as the ability to swallow the energy from many other waves.

4.1.1 Parameters for the GNLSE

The system that is investigated with the GNLSE is cascaded SC generation based on near-IR pumping. The cascade consists of four fibers, each designed to push the SC spectrum further towards the mid-IR. In Figure 4.1 the fiber cascade is illustrated. The seed laser provides low power seed pulses at a repetition rate of 1 MHz, with a FWHM pulse duration of 40 ps (in intensity) at the centre wavelength 1.56 μm. The seed pulses are amplified in a 5 metre Er-doped step-index silica fiber, and subsequently in a 1.5 metre step-index Thulium-doped silica fiber, at which point the SC spectrum spans to 2.8 μm with an average power of approximately 800 mW. The process of generating an SC inside a gain fiber is referred to as in-amplifier SC generation [62], and it is the same principle that is used in our SC laser for mid-IR OCT, which is described in the next chapter. The last two fibers in the cascade are a ZBLAN fiber and a chalcogenide glass fiber, based on the composition As_2Se_3.

For the purpose of brevity, and because SC generation in silica fibers was covered in Chapter 2, the spectrum out of the ZBLAN fiber will simply be treated as initial conditions in the following. In [18] a suggestion of how to treat gain fibers in the GNLSE is given, along with a discussion on the significant challenges it poses.

In table 4.1 the constant fiber parameters are given. The core radius and NA were used to calculate the effective index and area, whereas the nonlinear refractive index and fractional Raman response are direct input to the GNLSE, as detailed in section

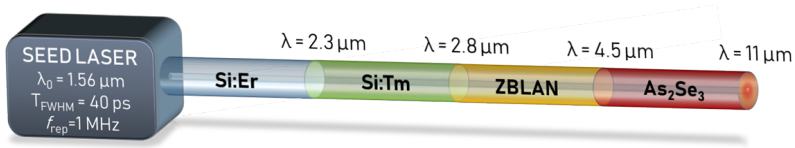

Figure 4.1: Illustration of the considered fiber cascade. At the output of each fiber the IR edge of the supercontinuum is indicated.

Fiber	a [μm]	NA	$n_2 \cdot 10^{20}$ [m^2/W]	f_R	Company
ZBLAN	3.5	0.265	2.1	0.0969	FiberLabs
As_2Se_3	6	0.76	1500	0.0103	IRflex

Table 4.1: Constant fiber parameters in the simulations, where "a" is the fiber core radius..

2.3. Notice that the nonlinear refractive index of the As_2Se_3 fiber is three orders of magnitude higher than in the ZBLAN fiber. This leads to extremely rapid nonlinear dynamics, which can make up for the high losses in the glass.

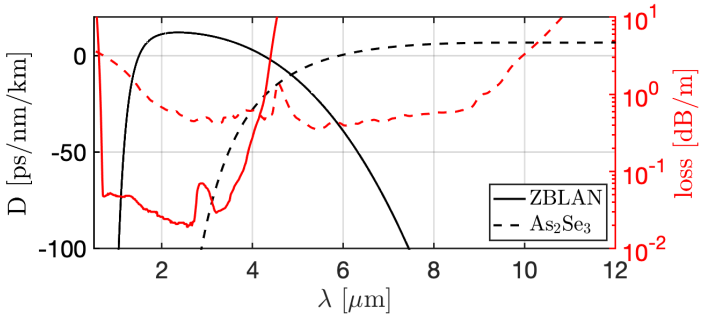

Figure 4.2: The dispersion and loss of the ZBLAN and As_2Se_3 fibers. The dispersion of the ZBLAN fiber is given in [57], and the material index of the As_2Se_3 fiber is obtained from [68]. The loss in the ZBLAN fiber was measured by former PhD-student Kyei Kwarkye, and the result is unpublished. The loss in the As_2Se_3 fiber is provided in [45].

The dispersion and fiber loss are given in Figure 4.2. The ZBLAN fiber transmits light slightly above 4 μm, while the As_2Se_3 glass has a much broader transmission window to past 10 μm, but a minimum loss more than an order of magnitude higher. In Figure 4.3, the Raman gain functions are shown for silica, ZBLAN, and As_2Se_3 glass. The silica and ZBLAN gain have been scaled by a factor of 100 to show it on the same scale as the As_2Se_3 glass.

In all simulations 2^{19} grid points, separated by 1.5 fs, and a central angular frequency of $\Omega_0 = 2\pi \cdot 350 \cdot 10^{12}$ rad $\cdot$ s^{-1} $\approx$ 857 nm, are used. 1 % input RIN and one-photon-per mode noise [42] were included at the input to the silica fiber, and all spectrograms

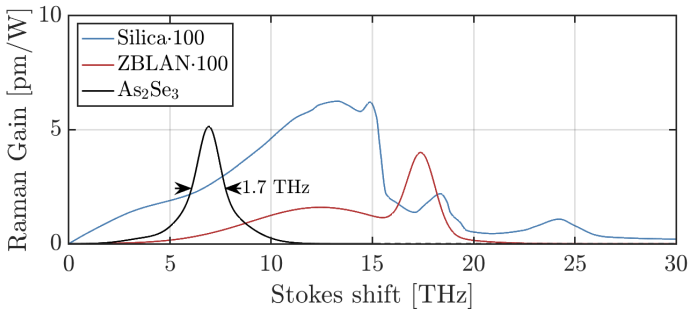

Figure 4.3: The Raman gain of the ZBLAN and As_2Se_3 compared to that of silica. Note that the ZBLAN and silica gain have been scaled by a factor of 100. The ZBLAN Raman gain is provided in [69], and the As_2Se_3 in [44].

were calculated with a window width of 150 fs.

4.1.2 Collective redshift

In the fiber cascade described in the previous section, the output of the ZBLAN fiber is a soliton rich SC. The solitons have been spectrally and temporally distributed through Raman redshift and dispersion, respectively. The presence of all these high-power sub-pulses means that dynamics happens very rapidly when the light is coupled into the As_2Se_3 fiber. The spectral evolution is shown in Figure 4.4, using an average of an ensemble of ten pulses in the output spectra.

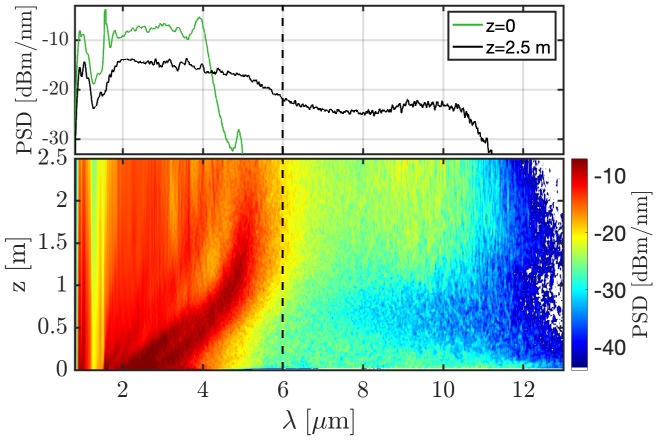

Figure 4.4: The spectral dynamics in the As_2Se_3 fiber. On top the output spectrum of the ZBLAN (green) and the As_2Se_3 fiber (black) are shown. The dashed line shows the ZDW.

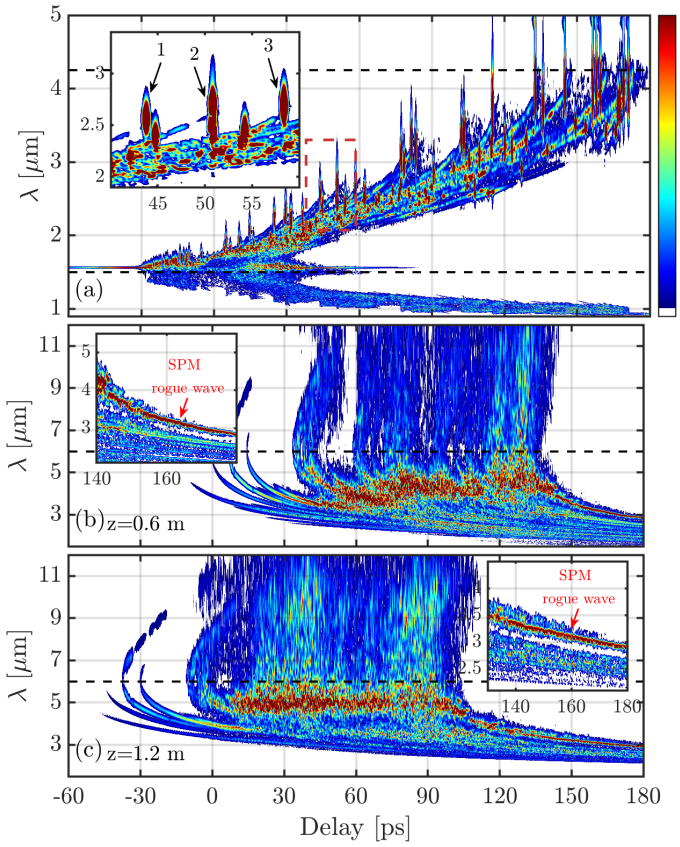

Figure 4.5: Spectrograms showing snapshots of the nonlinear dynamics in the As_2Se_3 fiber. The top spectrogram shows the output from the ZBLAN fiber, while the other two spectrograms show snapshots after 0.6 m and 1.2 m, respectively. In the inset in the top figure three solitons have been marked. These are highlighted to show the redshifting more clearly in the following. The insets in the two bottom figures show the high power SPM rogue wave at the trailing edge of the pulse, which will be treated in the next section. Note that the wavelength axis has been changed between the top spectrogram and the two below.

The top figure shows the input and output spectra of the As_2Se_3 fiber. The output spectrum spans past 10 μm, which as described previously, is enabled by the broad transmission window and high nonlinearity of the As_2Se_3 fiber. The bottom part of the figure shows the nonlinear dynamics that leads to such a broad spectrum. It is evident that there are two different relevant length scales on the figure. On the short length scale, a very broad spectrum is achieved almost immediately. As will be shown later, this is due to SPM and OWB of the high-power input solitons. In fact, this initial dynamics is the reason behind the noise reduction, that is the topic of section 4.2. The high loss in the fiber becomes immediately apparent, as the PSD starts falling in the

red edge. On the longer length scale a high-power structure starts redshifting towards the ZDW on a length scale of metres. Once it gets close enough to the ZDW power is radiated across it, which means that after 1 metre of propagation the spectrum once again spans past 10 μm. This redshifting structure was also observed in [18, 70] but without a thorough description and explanation.

The nonlinear dynamics in the As_2Se_3 fiber is shown in spectrograms in Figure 4.5. The top spectrogram, showing the input, resembles that obtained at the output of the "Extreme" fiber in Chapter 2. Between the two ZDWs of the ZBLAN fiber the dispersion is anomalous, and therefore this part of the spectrum contains many solitons. Three solitons have been specifically highlighted in the inset, as these three will be used in the following to illustrate the dynamics more clearly. Across both ZDWs DWs have been created.

In the middle spectrogram, after 0.6 m of propagation, the solitons have spectrally broadened through SPM and OWB, which has pushed the spectrum towards the ZDW, leading to radiation of energy far into the mid-IR. Simultaneously, the bulk part of the energy is localised in a spectral band between 3 and 5 μm. The high power structure is spread out temporally across almost 100 ps with energy at longer wavelengths in the trailing edge of the pulse, and shorter wavelengths at the leading edge.

#	P_0 [kW]	T_{FWHM} [fs]	λ_0 [μm]	γ [1/(Wm)]	β_2 [ps^2/m]	z_{OWB} [mm]
1	42.8	50	2.55	0.58	523	1.3
2	78.6	30	2.72	0.54	476	0.6
3	44.2	90	2.68	0.55	487	2.5

Table 4.2: Parameters for solitons 1-3 marked in Fig. 4.5 (a). The relevant parameters are: Peak power P_0, temporal FWHM T_{FWHM} (measured in intensity), centre wavelength λ_0, dispersion β_2, fiber nonlinearity γ, and optical wave breaking (OWB) distance z_{OWB} calculated from the analytical formula given in [71], all evaluated at λ_0.

After 1.2 m, as shown in the bottom spectrogram, the entire band of energy has been moved close to the ZDW, and at the same time significant energy has been shifted across it. This shows that the shift of energy in the energy band is responsible for the majority of the power in the desired long wavelength range. At the trailing edge of the pulse, one single remnant of an input soliton has swallowed significant energy and is now slightly isolated from the remaining spectrum, as shown in the inset. In the next section it is shown how this can be considered a novel type of rogue wave.

The spectral dynamics shown in Figures 4.4 and 4.5 consist of so many simultaneous effects that a full description would be too complicated. Therefore, a simplification to better describe the novel part of the dynamics is appropriate. Instead of continuing with the full ZBLAN output, the three solitons marked by 1-3 in the inset at the ZBLAN output in Figure 4.5 will be used as an input to the simulations. Relevant parameters for the solitons are given in Table 4.2.

When only the three solitons are used as an input to the GNLSE, the result is strikingly similar dynamics as the full ZBLAN output. The dynamics are shown in

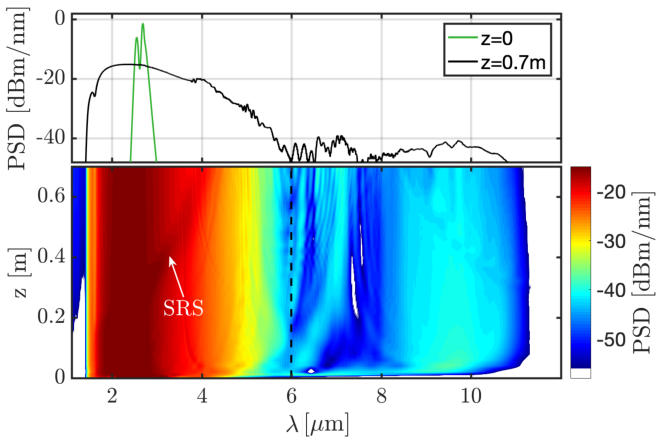

Figure 4.6: The spectral evolution of solitons 1-3 with the same fiber parameters as in Figure 4.4. The top shows the spectrum at the input and after 0.7 m propagation.

Figure 4.6. Due to this, the seemingly more simple spectral dynamics in Figure 4.6 can be considered to understand the full spectral dynamics. Once again, spectral broadening happens almost immediately through SPM and OWB. After approximately 20 cm of propagation, significant energy starts redshifting in the anomalous dispersion towards the ZDW. In Figure 4.7 it is shown that the shift in energy is due to stimulated Raman scattering (SRS) between the three now spectrally broadened and temporally dispersed input pulses.

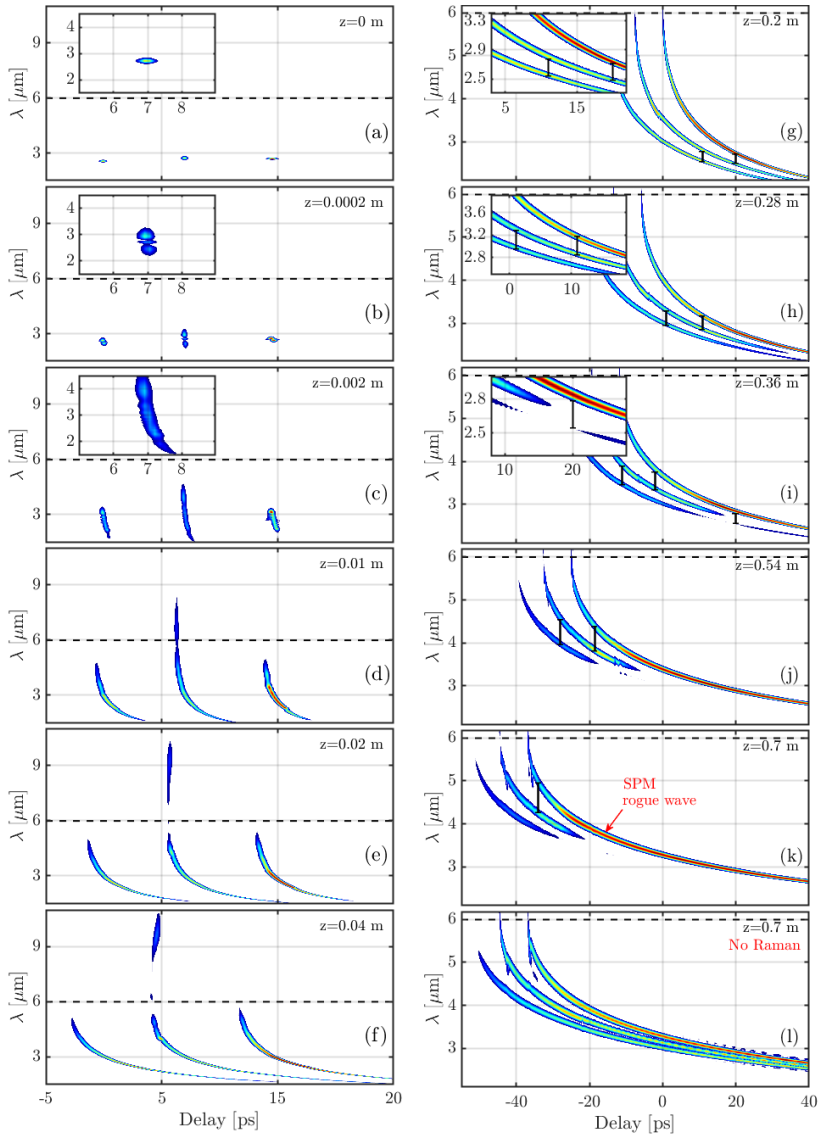

Figure 4.7: Spectrogram series showing snapshots of the propagation of solitons 1-3 in the As_2Se_3 fiber. Insets in (a)-(c) and (g)-(i) show a close up of certain parts. Scale bars indicating the spectral shift possible through the Raman effect are shown on top of the spectral components in (g)-(k). In (k) the SPM rogue wave has been indicated. In (l) the same spectrogram as in (k) is shown if the Raman effect is turned off (by setting $f_R = 0$). Dashed lines indicate the ZDW. Note that the time and wavelength axes change between the two columns.

In the following I will break down the dynamics seen in the spectrogram series in

Figure 4.7.

1. **0-2 mm** (a)-(c): The output of the ZBLAN fiber is taken to be the 3 solitons, that are highlighted in Figure 4.5 (a). Within 2 mm of propagation these undergo SPM, and soliton 1 and 2 have undergone OWB as highlighted for soliton 2 in the insets. This is in good agreement with the OWB length scales given in Table 4.2.

2. **1-4 cm** (d)-(f): The three pulses do not spectrally broaden further but are dispersed temporally, with long tails in the short wavelength edge due to the very high absolute value of the dispersion in this spectral range. Soliton 2 has reached close enough to the ZDW, that a DW has been created, which pushes the spectrum past 10 μm.

3. **20-70 cm** (g)-(k): As the pulse tails are dispersed, a temporal overlap is created between different spectral components in the three pulses. When this temporal overlap occurs, within the Raman gain band, energy is redshifted from the leading pulse towards the trailing pulse. The overlap of the Raman gain with the neighbouring pulses is shown with black scale bars that have been put on relevant spectral components. The energy transfer is first apparent in (h) where the pulse tail originating from soliton 2 has been swallowed by the pulse tail from soliton 3. In (i) it is shown that this leaves a pulse tail from soliton 1, that can still not transfer energy due to no Raman overlap as shown by the scale bar that does not reach all the way between soliton 1 and 3. In (j) the dispersion has created an overlap for this part as well, and now most of the energy, that was initially in soliton 1 and 2, has been swallowed by soliton 3, which has created a high energy structure, that is identified as an SPM rogue wave.

4. **70 cm** (l): The spectrogram shown in (l) is the same as in (k) with the Raman effect turned of, by setting $f_R = 0$. The fact that all pulse tails are still present underlines that it is indeed SRS, that is responsible for the energy transfer.

The amount of energy that is shifted only grows stronger from the amount of pulse tails, and thereby input pulses that are present. Due to the strong dispersion in the fiber, the pulse tails will inevitably end up transferring energy due to the Raman effect, as long as the fiber is long enough and the fiber loss is not too significant. If the fiber is not long enough, the energy transfer will depend on the number of closely spaced solitons present at the output of the previous fiber.

As the shifting temporal overlap is necessary for the collective redshift, the dispersion is a key parameter for the rate of the redshift. Furthermore, the ZDW limits the redshift, as this is the point where neighbouring spectral components have the same group velocity. Ultimately, this means that the rate of redshift and the final position of the localised SRS structure can be tuned by changing the fiber geometry and thereby the dispersion properties. This dependence will now be investigated further.

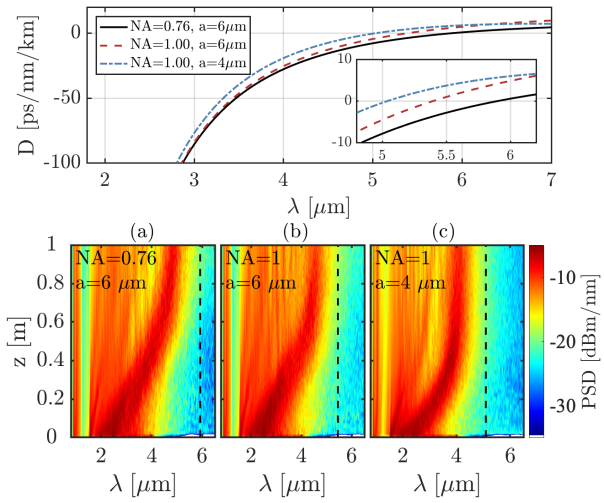

Figure 4.8: Bottom: The dynamics in 3 As_2Se_3 fibers with different ZDW of approximately 6 μm (original fiber, NA=0.76, core radius=a=6 μm), 5.5 μm (NA increased to 1 by reduced cladding index), and 5.1 μm (NA=1 and a= 4 μm), respectively. Top: Dispersion of the three fibers, where the inset shows the dispersion close to the ZDWs.

4.1.3 Manipulating the SRS structure through dispersion control

The dependence on the ZDW is shown in Figure 4.8, where the full output of the ZBLAN fiber, as shown in Figure 4.4, is the input to three different As_2Se_3 fibers with different core radii and NA. The change in fiber parameters shifts the ZDW between approximately 6 μm (original fiber (a) with a = 6 μm and NA=0.76), 5.5 μm (higher NA (b) with a = 6 μm and NA = 1), and 5.1 μm (smaller core (c) with a = 4 mum and NA = 1).

The simulations in Figure 4.8 show that the SRS structure never crosses the ZDW, but instead slowly approaches with the rate depending on the magnitude of the dispersion. Close to the ZDW, the magnitude of the dispersion is approximately given by $\beta_3|_{\Omega=\Omega_{\mathrm{ZDW}}}(\Omega - \Omega_{\mathrm{ZDW}})$, where $\beta_3 = \frac{\partial \beta_2}{\partial \Omega}$. Therefore, β_3 will indicate how close to the ZDW the SRS structure will come. Indeed, the SRS structure comes closest to the ZDW in (b) which has the largest dispersion slope at the ZDW of β_3=2.4 ps^3/km, where fibers (a) and (c) have β_3=2.1 ps^3/km and β_3=1.9 ps^3/km, respectively. Figure 4.8 really shows the power of performing simulations, as the only effort needed to perform this comparison is calculating new dispersion profiles for different fiber parameters. By controlling the dispersion, the high power SRS structure can be spectrally positioned to target specific applications - such as a 4 μm OCT system.

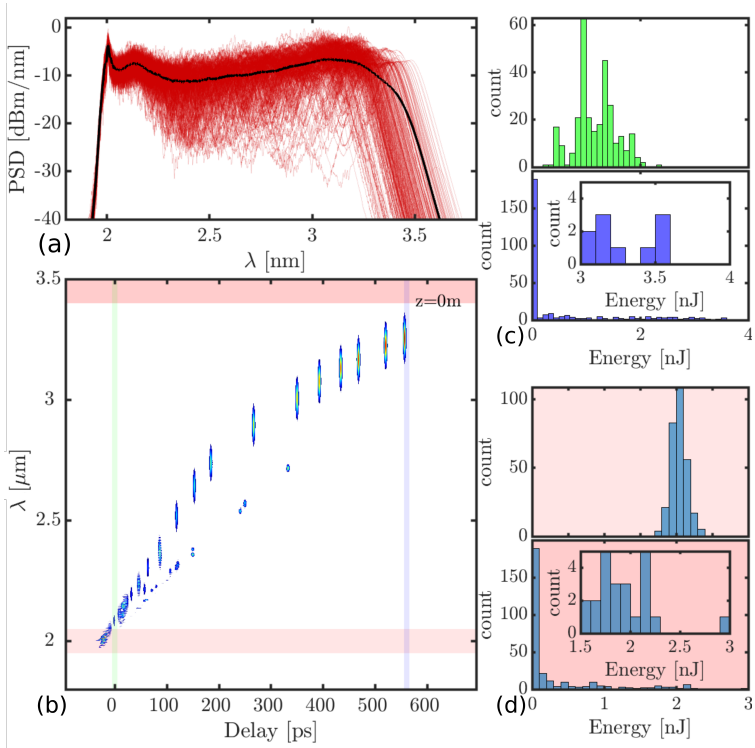

Figure 4.9: Output of 295 simulations in the 40 m ZBLAN fiber. (a) The output spectrum, with each simulation shown in red, and the mean shown in black. (b) A spectrogram showing the output of a single simulation. (c) Histograms of the distribution of pulse energies across the 295 simulation in the green and purple bands shown in (b). (d) Similar histograms showing the pulse energy distributions in the two red-bands in (b). Where the insets show the most extreme occurrences in the long tail. Notice that the red shading is different in the two bands, to distinguish the two histograms.

4.1.4 Rogue wave statistics

To demonstrate the rogue wave nature of the SRS structure, a large number of simulations are needed, as the L-shaped statistics cannot otherwise be shown. Therefore, a simpler system is now considered. The radius of the ZBLAN fiber is changed to 8 μm, such that there is only one ZDW, which is at 1556 nm. Furthermore, the ZBLAN fiber is now 40 m long, and it is the first fiber in the cascade. Finally, the ZBLAN fiber is pumped by a Gaussian shaped pulse at 2000 nm with peak power 4 kW, and pulse duration 10 ps in intensity. Vacuum fluctuations are included in the form of one-photon-per-mode noise [42]. These simplifications allowed simulating 295 different noise seeds, as shown in Figure 4.9.

In Figure 4.9 (a) the output spectra of all 295 simulations are shown as individual red lines along with the mean shown in black. Evidently, there is significant variation

between each simulation - especially at the infrared edge of the spectrum. This is typical for many cases where rogue waves are observed [72–74]. In (b) a spectrogram of a single

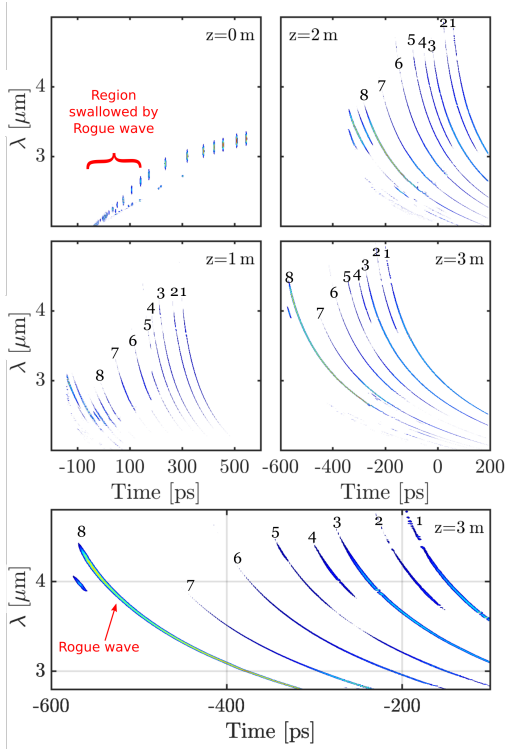

Figure 4.10: Spectrogram series showing the appearance of the SPM rogue wave. The first spectrogram shows a single simulation at the output of the ZBLAN fiber. All the pulses marked by the curly bracket get absorbed by the SPM rogue wave within 3 m of propagation. The next three spectrograms are separated by 1 m in the As_2Se_3 fiber. The bottom spectrogram shows a close up of the same spectrogram as shown above after 3 meters.

simulation is shown. A lot of solitons have been created, and they have been spectrally distributed through the peak power dependent SSFS. The spectral distribution further leads to a temporal spread due to the wavelength dependent dispersion, which in turn means that the most high power solitons will be associated with the biggest delay.

Two spectral bands indicated by light red shading between 1.95 and 2.05 μm, and darker red shading above 3.45 μm, correspond to spectral filters used to create the histograms in (d). Similarly, the green and purple temporal bands indicate temporal filters resulting in the histograms in (c). The bottom histogram in (d) shows the L-shaped distribution of pulse energies, appearing after spectral filtering, that typically shows the occurrence of rogue waves. Whereas the other spectral filter, around the input pulse centre wavelength, produces the more symmetric distribution shown in the top histogram. In (c) it is shown that applying 10 ps long temporal filters gives

the same tendencies. When applied far in the trailing edge of the pulse, where rogue waves exist, it leads to a similar L-shaped statistics as in (d). As the pulses are better separated in time than in frequency, the similarity in statistics will be used in the following to look for rogue waves with temporal filters instead of spectral filters.

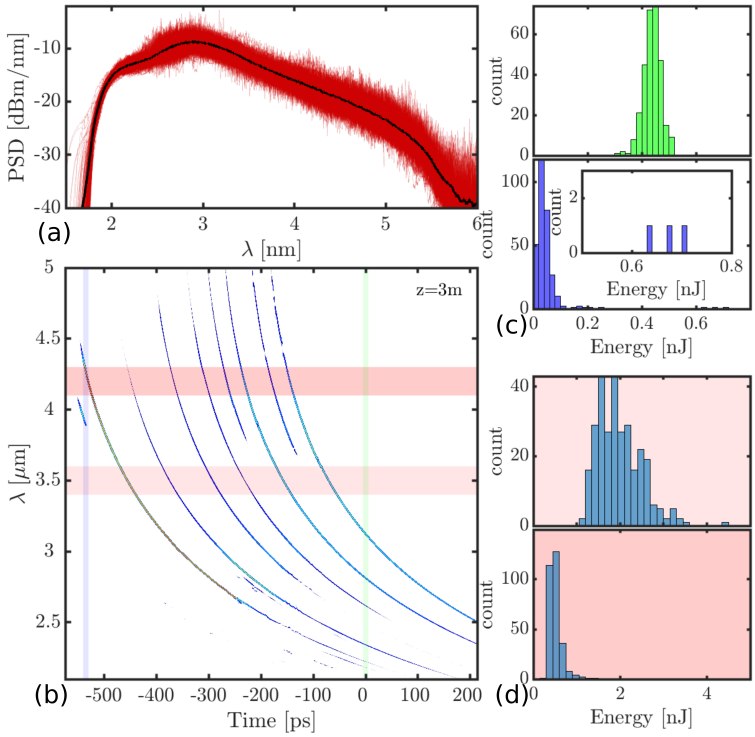

Figure 4.11: Output of 295 simulations in the 3 m As_2Se_3 fiber. (a) The output spectrum, with each simulation shown in red, and the mean shown in black. (b) A spectrogram showing the output of a single simulation. (c) Histograms of the distribution of pulse energies across the 295 simulation in the green and purple bands shown in (b). (d) Similar histograms showing the pulse energy distributions in the two red-bands in (b). Where the insets show the most extreme occurrences in the long tail. Notice that the red-shading is different in the two bands, to distinguish the two histograms.

Before investigating the L-shaped statistics of the SPM rogue wave, the dynamics that can lead to it in 3 m of As_2Se_3 fiber is illustrated with spectrograms in Figure 4.10. The 8 most redshifted pulses out of the ZBLAN fiber are labelled, in order to demonstrate that the 7 largest and most redshifted pulses are not the ones that become the SPM rogue wave. The SPM rogue wave is pulse number 8, which initially has only 6.2 % of the energy. It is able to absorb the energy of a large number of neighbouring pulses at shorter wavelengths and ends up as an SPM rogue wave with 51.2 % of the total energy after 3 m of propagation.

In Figure 4.11, the statistics of all 295 simulations of the As_2Se_3 fiber is shown. The

output of the simulations shows a significantly broadened spectrum, and interestingly, the fluctuations around the mean are much smaller. The reduced fluctuations will be explored in much greater detail in section 4.2. The histograms of the pulse energies after spectral filtering (two shades of red) show no clear evidence of rogue waves. The reasoning for this is apparent in the spectrogram, in which the spectral filter includes many pulses. However, in the temporal filtering, coloured in a purple shading, the rogue-wave like L-shaped distribution of pulse energies is apparent. The rogue wave now appears at the leading edge of the pulse, rather than the trailing edge which was the case in Figure 4.9.

Thereby, it has been shown that the SPM rogue wave contains high energy compared to the remaining structure, and that it follows an L-shaped probability distribution of pulse energies. Furthermore, it appears by absorbing energy from the remaining spectrum, which is analogous to the commonly observed rogue waves that appear through soliton interactions. Finally, it is worth noting that the L-shaped distribution could be shown even more clearly by designing a filter in both time and frequency using the dispersion curve of the fiber, such that the entire energy of the spectrally broadened and temporally dispersed pulse could be displayed in the histograms.

The next section will investigate the reduced fluctuations shown in Figure 4.11. It will be shown that this is in fact due to a spectral averaging of all the input pulses, which leads to a reduction of the RIN

4.2 Supercontinuum Noise Reduction Using a Short Piece of Normal Dispersion Fiber, Paper [III]

The dominating technology in both near-IR and mid-IR SC lasers is still based on ps pulses and MI. Therefore, efficient noise reduction of these sources is very relevant. On top of the already mentioned spectral alignment through a second ZDW, a completely novel approach to noise reduction is presented here. The novel noise reduction mechanism is based on coupling a noisy soliton rich spectrum into a short piece of normal dispersion fiber. In Figure 2.3 it was shown how normal dispersion leads to SPM and OWB of the input solitons. If the spectral broadening of each soliton is sufficient, and the number of solitons is also sufficient, the once spectrally distributed pulses will now spectrally overlap, such that the pulse-to-pulse fluctuations are washed out on an intra-pulse level. Both noise reduction mechanisms are experimentally verified in a cascaded mid-IR laser based on a ZBLAN fiber, and an arsenic sulfide (As-S) fiber.

4.2.1 SC source and fiber parameters

Two mid-IR SC sources are considered in order to compare the two noise reduction mechanisms. The only difference between the two sources is the choice of ZBLAN fiber, denoted ”ZBLAN A” and ”ZBLAN B”. The main difference between the two fibers in terms of SC generation is that ZBLAN B has a second ZDW. The second ZDW stems from a reduced core size of ZBLAN B compared to ZBLAN A. Relevant fiber

Fiber	D [μm]	NA	$n_2 \cdot 10^{20}$ [m^2/W]	f_R	Manufacturer
Tm/Ge:Si	12	0.28	6.0	0.18	In-house
ZBLAN A	7.5	0.26	2.1	0.097	FiberLabs Inc
ZBLAN B	6.5	0.265	2.1	0.097	FiberLabs Inc
As-S	8	0.25	420	0.01	Art photonics GmbH

Table 4.3: Constant fiber parameters. D is the fiber diameter, NA is the numerical aperture, n_2 is the nonlinear refractive index that was assumed in the numerical simulations, and f_R is the fractional Raman response used in the simulations.

parameters for the fibers are given in Table 4.3. The nonlinear refractive index and fractional Raman response are calculated parameters for the simulations, while the core diameter and numerical aperture are provided by the manufacturer.

The dispersion of the three fibers along with the other fiber parameters, that are neccessary for simulations, are shown in Figure 4.12. The second ZDW of ZBLAN B is at 3.55 μm, which allows DW generation in the normal dispersion region bordering the IR loss edge of ZBLAN. The dispersion of ZBLAN B is a measurement, while the dispersion of ZBLAN A and the As-S fiber are calculated with the analytical method described in section 2.3, with the core refractive index for ZBLAN given in [75]. For the As-S fiber the core index is given in [68]. The effective areas are also calculated analytically, and the effective area of ZBLAN A has been assumed for both ZBLAN fibers. This assumption was made because the measured dispersion of ZBLAN B could not be properly reproduced in the analytical models. As such, it is questionable whether the effective area would be calculated correctly either.

The loss and Raman response of ZBLAN are the same as discussed in section 4.1.1. The loss of the As-S fiber is assumed equal to that provided in [45], and the Raman gain that in [76].

Noise reduction through spectral alignment of solitons and DWs from a second ZDW is an already known noise reduction mechanism [19]. As this type of noise reduction is applied in the mid-IR OCT laser, it is relevant to compare the novel noise reduction mechanism to this.

A sketch of the two considered mid-IR SC cascades, along with the noise measurement setup, is given in Figure 4.13. An already generated SC based on 0.5 ns pulses at a repetition rate of 3 MHz is delivered by a custom built laser (Connet laser Technology, Ltd.). A 30 cm Tm/Ge doped silica fiber is spliced to the output, which pushes the spectrum to 2800 nm with an average power of 870 mW. The Tm/Ge doped silica fiber was fabricated at Nanyang Technological University. It has a core/cladding diameter of 12/125 μm, and a dopant concentration of 0.15/20 wt% for Tm and Ge, respectively [77]. The light is further coupled into either ZBLAN A or ZBLAN B with a 15 mm focal length reflective collimator and an anti-reflective (AR) coated ($1.8 - 3$ μm) aspheric lens. ZBLAN A is 2.8 m long, and 450 mW of average power is delivered with an IR spectral edge close to 4 μm. In ZBLAN B, 1.05 m of fiber is enough to generate an SC that spans to 4.5 μm with the same average power as ZBLAN A. This is in accordance

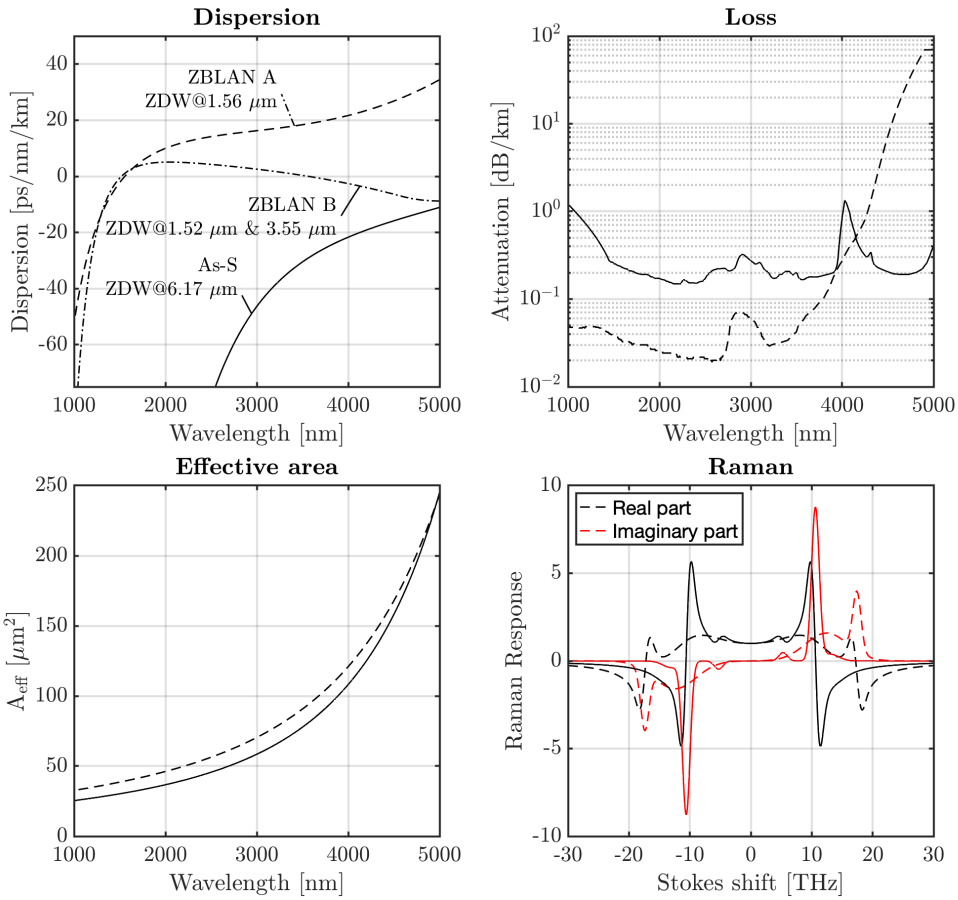

Figure 4.12: Fiber parameters for the two ZBLAN fibers, denoted ZBLAN A and ZBLAN B, and the As-S fiber. The effective area is assumed to be the same for the two ZBLAN fibers, while the loss and Raman response are assumed to only depend on the core glass. In all cases the solid lines refer to the As-S fiber, while dashed lines indicate the ZBLAN fibers.

with the literature, where it was found that the second ZDW allows a broader SC [57]. However, ZBLAN A has the advantage that the IR edge of the spectrum still contains solitons, which is better suited for further redshifting in a subsequent fiber, and as it turns out also for the novel noise reduction mechanism presented here.

Finally, the output of the ZBLAN fibers can be free space coupled to a 72 cm piece of As-S fiber with two $3-5$ μm AR coated aspheric lenses. In both options there is 180 mW average power at the output. The significant reduction in average power is partly caused by a ~ 17 % Fresnel reflection at each end facet.

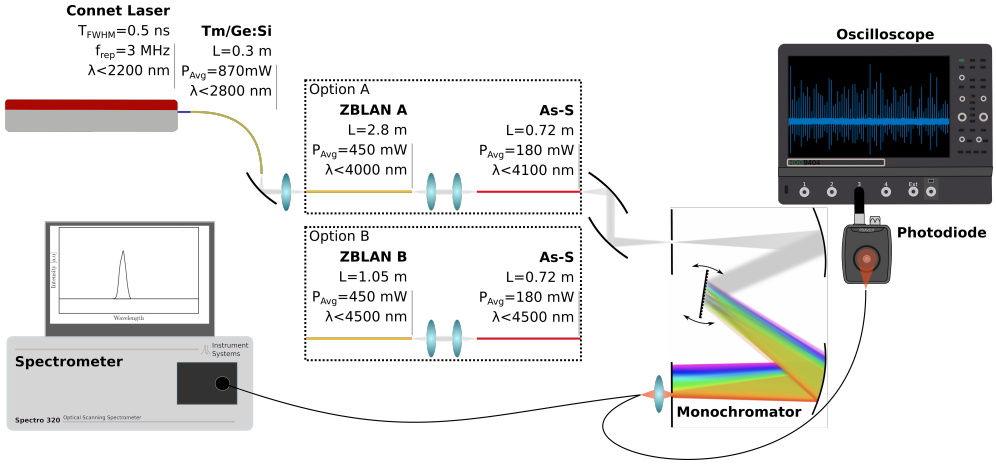

Figure 4.13: Sketch of the setup consisting of a cascaded SC laser with two different options for the ZBLAN fiber. The SC is free space coupled to a Czerny-Turner monochromator. The output of the monochromator is either measured in an OSA or on a photodiode connected to an oscilloscope.

4.2.2 Noise measurement setup

The setup for noise measurements is shown after the SC fiber cascade in Figure 4.13. The SC light is focused through a narrow entrance slit of a Czerny-Turner design monochromator (Horiba iHR320). The monochromator consists of a grating that can be rotated to choose the centre wavelength, and an adjustable output slit to choose the bandwidth. An array of long pass filters allows filtering out higher harmonics of the filtered signal. The output of the monochromator is coupled to an InF_3 patch cable which can either be directed at an MCT photodiode (PDAVJ10, Thorlabs, Inc.) connected to an oscilloscope (HDO9404, Teledyne Lecroy), or coupled into an OSA (Instrument Systems, Spectro320, covering $0.2 - 5$ μm).

4.2.2.1 Photo diode considerations

As detailed in the [78], care should be taken in regards to the photo diode in a time domain RIN measurement. When operating in the linear response regime of the photo diode, the measured voltage, $V_{Diode-Linear}(t)$, is given by:

$$V_{Diode-Linear}(t) \propto \int_{-\infty}^{\infty} P_D(t-t')P_{Pulse}(t')\mathrm{d}t', \tag{4.1}$$

where $P_D(t-t')$ is the photo diode response function, and $P_{Pulse}(t')$ is the temporal shape of the measured pulse.
If the pulse is much shorter than the photo diode response time, typically quoted as the rise time of the photo diode, the pulse shape can be considered a delta function $P_{Pulse}(t') = E_P\delta(t-t')$, where E_P is the pulse energy. Under this assumption the

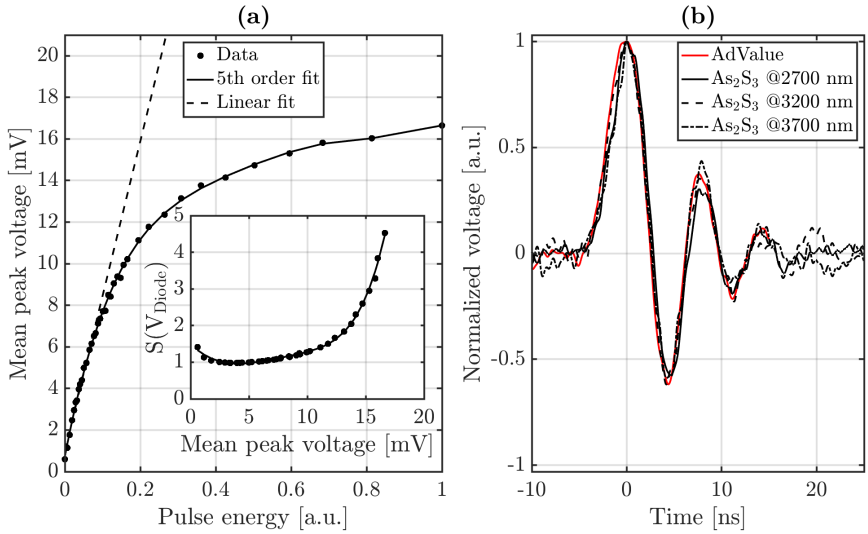

Figure 4.14: Characterisation of the usability of the PDAVJ10 photodiode. **(a)** The relationship between the measured mean peak voltage measured by the photo diode and the pulse energy of the laser source (on an arbitrary scale). This measurement was made with the 2 μm, 1.9 ps AdValue laser. The inset shows the ratio between the 5th order polynomium fit to the linear fit, thus describing the nonlinearity of the photo diode response. **(b)** The temporal shape of the photo diode response function $P_D(t-t')$ as measured with the AdValue laser (red curve). Along with the shape of the photo diode response function is the measured voltage response at three different monochromator settings from the RIN measurements at the output of the As_2S_3 fiber in option A.

measured voltage, within the linear regime, can instead be stated as

$$V_{Diode-Linear}(t) \propto E_P P_D(t). \tag{4.2}$$

Therefore, the peak value of the measured voltage of each spectrally filtered pulse corresponds directly to the pulse energy. However, to apply this expression, it must be ensured that the filtered pulses are in fact much shorter than the photo diode response time. The rise time of a photo diode is approximately given by $\frac{0.35}{f_{BW}} = \frac{0.35}{100\text{ MHz}} = 3.5$ ns [1], where $f_{BW} = 100$ MHz is the bandwidth of the PDAVJ10 photo diode. With an input pulse duration of 0.5 ns it is not directly evident that the spectrally filtered SC pulses are short enough for the assumption to hold. Instead, the assumption is validated by comparing the shape of the measured voltage with that from a 1.9 ps pulse duration laser at 2 μm from AdValue (AP-TM-ML01, Ad-Value Photonics).

In Figure 4.14 **(b)**, a comparison is shown between the shapes of the measured voltage for the AdValue laser and the output of the As_2S_3 fiber in option A. The output of the As_2S_3 fiber in option A represents the longest possible fiber length, and

[1]This approximate formula is provided on the manufacturer's, Thorlabs, website https://www.thorlabs.com/newgrouppage9.cfm?objectgroup_id=11689&pn=PDAVJ10 - accesed 23/02/2023

also the configuration with the most dispersion, which means it can be considered the most extreme case in terms of temporal broadness. The comparison is shown for three different centre wavelengths on the monochromator, and in all three cases the shape of the measured voltage matches that from the AdValue laser. Therefore, it is concluded that equation P_{pulse} can safely be considered a delta function in this context.

A second consideration in terms of the photo diode response time is that it must be much faster than the repetition rate of the laser, such that the pulses are nicely separated on the oscilloscope. At a repetition rate of 3 MHz each pulse arrives with a spacing of 333 ns, which is about an order of magnitude higher than the entire shape of the measured voltage as shown in Figure 4.14 **(b)**.

A final important consideration when using the photo diode is that the relation between the power and the measured voltage is not linear for all powers. In [78] this is treated by measuring the relationship between input pulse energy and the peak values of the measured voltage. Once this relationship is known, a region of measured peak voltage can be defined for which the relationship is considered linear. A similar measurement for the PDAVJ10 photo diode is shown in Figure 4.14 **(a)**. Due to high laser noise, high electronic noise, and an asymmetric distribution of pulse energies in the SC laser, the approach of operating only in the linear regime of the photo diode was unviable in this experiment. However, since the full relationship between the measured peak voltage and the pulse energy has been measured it is possible to take the nonlinearity of the response into account. This is done by introducing the scaling function $S(V_{Diode})$ as seen in the inset in Figure 4.14 **(a)**. $S(V_{Diode})$ is the ratio of the fifth order polynomial fit to all the data points and the linear fit, which only uses data points up to 6.6 mW. After taking $S(V_{Diode})$ into account equation 4.2 can instead be stated as

$$\mathrm{S}(V_{Diode})V_{Diode} \propto E_P P_D(t). \tag{4.3}$$

The scaling function corrects a severe underestimation of the RIN, which originates from the saturation of the measured response. In the case of ZBLAN A, the scaling function means the difference between 27 % and 35 % RIN at 3 μm. The scaling function has been applied to all the measured RIN curves in the following. Note that the scaling function can only be introduced because it has already been shown that P_{pulse} can be considered a delta function - otherwise the nonlinearity of the response would have also affected the shape of the measured voltage response.

4.2.2.2 Data acquisition and processing

The final aspect that has to be taken into account before performing the noise measurements is that the observed RIN depends on the mean measured voltage on the photo diode. This issue is illustrated in Figure 4.15, where the RIN is shown as a function of the mean of the peak voltages in a measured pulse train. The mean of the peak voltages has been adjusted by mounting the InF_3 patch cable on a stage, such the distance between the patch cable and the photo diode can be varied, while keeping the diverging beam centred on the photo diode. These measurements were performed over two different days, and with and without an attenuating filter to show the robustness of the result. A clear dependence is seen, and therefore it is important to keep the

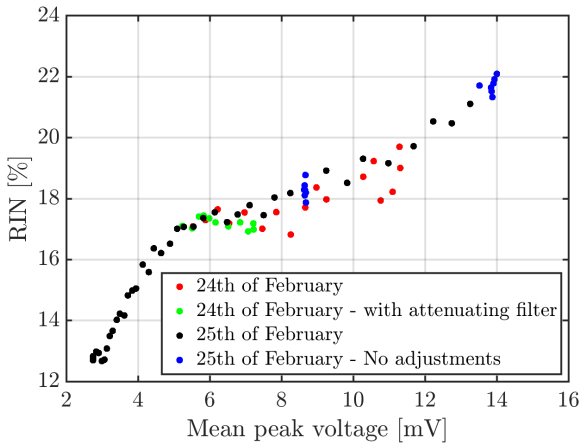

Figure 4.15: The influence on the RIN of the mean peak voltage measured by the photo diode. The scaling $S(V_{Diode})$ has been applied to the data. The data has been acquired over two days and with and without an attenuating filter to show the stability of the measurements.

mean peak voltage comparable between measurements. For this purpose a mean peak voltage in the $6-7$ mV range was chosen. This choice gives a variation in the measured RIN that is of the same magnitude as the variance between subsequent data sets at identical measurement configurations, as shown by the blue data points.

The noise measurements were performed in three steps:

1. Set the monochromator to the desired centre wavelength.
2. Average over 100 pulses on the oscilloscope and adjust the distance between the patch cable and the photo diode to achieve an average peak voltage in the $6-7$ mV range.
3. Record a pulse train of 3000 subsequent pulses. This approach is preferable to recording 3000 triggered pulses, as the triggering will result in pulses below the triggering value to be discarded. Thereby, triggering can result in an underestimation of the RIN as all pulses above the trigger value will be more alike, than a set of 3000 randomly chosen pulses.

After obtaining a full RIN curve the patch cable was moved to the OSA to measure the spectrum at the same position, such that the true centre wavelength and FWHM after the monochromator could be monitored. The bandwidth across almost all data points was 19 nm, except for a part of the spectral range at the output of the As_2S_3 fiber in option B, where the bandwidth was instead 38 nm. The increased bandwidth was necessary because the PSD in this range was too low to reach the $6-7$ mV level on the photo diode. The peak value of this measurement is reported as the spectral intensity of the source in the following. The 19 nm bandwidth was generally preferable

as the spectral resolving of the RIN is more accurate when using a narrower band. If a wider and wider bandwidth is considered it would in the limiting case result in simply measuring power fluctuations of the laser. The power fluctuations of the laser is probably a much lower value than the spectrally resolved RIN - or the spectrally averaged RIN, as introduced in section 3.1.

The pulse energy of each pulse in the pulse train was found in a few steps: The data was divided into 3000 bins each containing the measured voltage corresponding to a single pulse. Then the average value of the data floor is found, by considering the first 25 % of the data points in each bin. The average of the data floor is subtracted from each bin to remove any zero-offset. We found that a universal value for the average of the data floor could not be found due to a drift on the measured voltage on a longer time scale than the separation between pulses. Finally, the maximum of each bin is found and scaled by $S(V_{Diode})$, thus obtaining 3000 pulse energies E_P. Finally, the RIN is calculated as

$$\mathrm{RIN} = \frac{\sigma_{E_P}}{\mu_{E_P}}, \tag{4.4}$$

where σ_{E_P} is the standard deviation of the pulse energies, and μ_{E_P} is the average.

4.2.3 Results

The results of the RIN measurements are shown in Figure 4.16. The top row is the normalised spectra, and the bottom row the measured RIN. The columns show option A and option B as indicated by the titles. The difference between option A and option B is the use of ZBLAN A and ZBLAN B, respectively. The region where the 38 nm bandwidth was used is marked by crosses instead of dots.

The ZBLAN spectra clearly illustrate the impact of the different dispersion curves. In ZBLAN A, the spectrum spans to approximately 4 μm, while it spans to 4.5 μm in ZBLAN B. The broad bandwidth in option B is attributed to DW generation, and this process leaves a significant dip observed in the spectrum around the ZDW. In fact, the ZBLAN output in option B shows the spectrum of the SC laser in our 4 μm OCT setup that will be discussed in the next chapter. Two significant dips in the spectrum are observed within the DW, in the range $\sim 4.2 - 4.4$ μm which is probably due to CO_2 absorption in the free-space part of the setup.

As expected, the As_2S_3 spectra show no significant broadening for option B, as the DWs are temporally broad and therefore nonlinear effects are weak However, for option A the lack of broadening is unexpected as the spectrum from the ZBLAN fiber consists of high power solitons. The lack of broadening is presumably due to the low NA and large core diameter of the As-S fiber.

Spectral broadening was not the purpose of the experiments, but rather noise reduction, which is definitely achieved. The RIN of the entire spectrum above 2.7 μm is reduced, and from 3 μm to the IR-edge of the spectrum the reduction is most significant as a RIN of more than 35% is reduced to below 25%. The impact of such a noise reduction can result in a $\sim 50\%$ reduction in integration time in a spectrometer based application with similar noise performance. In option B, the RIN only changes slightly from the propagation in the As-S fiber. This is expected, as the very limited nonlinear

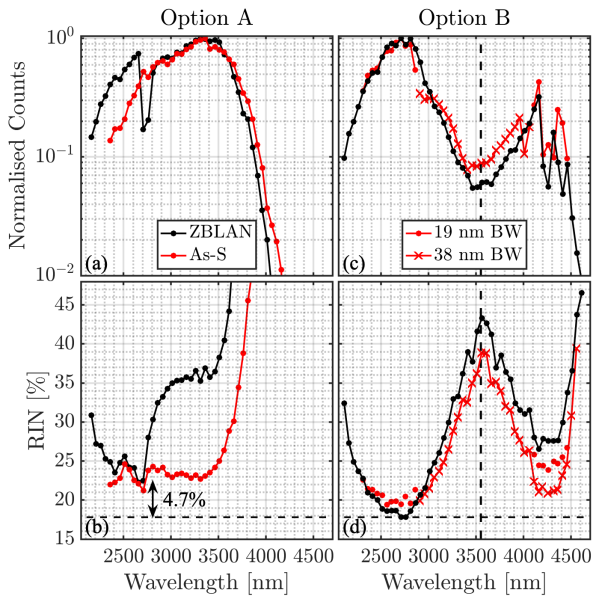

Figure 4.16: Measured spectra and noise curves of all configurations. Close to the ZDW, at approximately 3500 nm, in option B a bandwidth of 38 nm (crosses) had to be used, while 19 nm (dots) bandwidth was used in the remaining spectrum. The measurements were made with both bandwidths in the spectral region 4100-4500 nm in option B to highlight the influence of the bandwidth on the measured RIN. The dip in the spectrum in the As-S fiber in option A at 2700 nm is a measurement artefact from an optical density filter in the OSA. The vertical dashed lines indicate the ZDW. The horizontal dashed line in the RIN curves indicate the lowest measured RIN in option B, while the double arrow indicates the difference between the lowest obtained RIN at the output of the ZBLAN fibers.

dynamics should not produce a significant change in RIN. The RIN is highest close to the ZDW, at the dip in the spectrum, while the noise reduction through spectral alignment of DWs gives a lower noise than in option A for the remaining part of the spectrum.

It is interesting to investigate what impact the noise reduction has on the distribution of pulse energies. In Figure 4.17 this is shown for two wavelengths, representing the bulk part of the spectrum and the edge of the spectrum, namely 3510 μm (top) and 3910 μm (bottom), respectively. In option A (left column), a significant narrowing of the distribution is seen between the ZBLAN output and the As_2S_3 output, which is directly related to the noise reduction. In option B (right column), no similar narrowing is observed. In option A, 3910 nm is at the edge of the spectrum, which is evident through a very long tailed distribution, similarly to the numerical results in section 4.1, which is characteristic of rogue waves. The long tail is shortened significantly at the output of the As-S fiber, which agrees well with the observed noise reduction. Once again the distribution is left almost unchanged in option B.

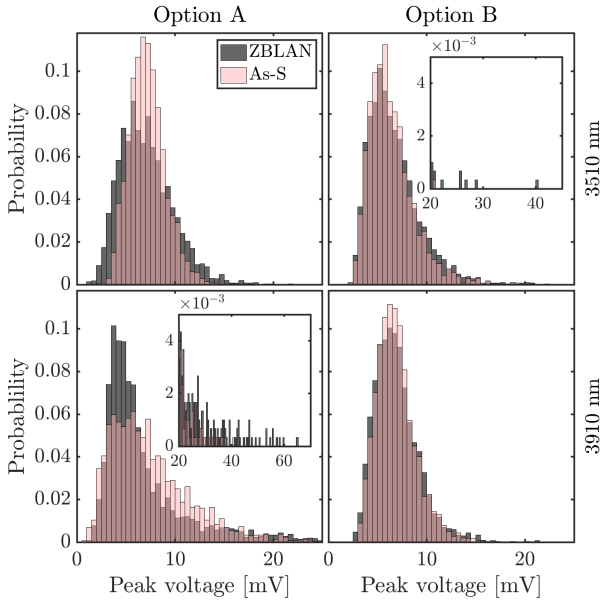

Figure 4.17: The distribution of measured peak voltage in all configurations. The peak voltage corresponds to filtered pulse energy. The insets show the long tail of the two L-shaped distributions that show rogue wave statistics.

4.2.3.1 Numerical results

The simulated results are performed with the implementation of the GNLSE, and the fiber spectrally dependent parameters given in Figure 4.12, the constant parameters in table 4.1, and additional parameters for the standard step-index SMF-28 silica fiber. The purpose of the simulations is to illustrate the noise reduction mechanism - not to match the experimentally observed spectra exactly. Since the actual fiber cascade is based on in-amplifier SC generation, and on an input pulse with 0.5 ns pulse duration, it is necessary to apply three simplifications.

1. The silica fibers are replaced by the parameters of a single 2.5 m SMF-28 fiber, except that the nonlinear refractive index was set to $6 \cdot 10^{-20} \frac{\mathrm{m}^2}{\mathrm{W}}$ such that the the IR edge of simulated spectrum matches that of the measured spectrum.

2. The input pulse is replaced by a Gaussian shaped input pulse at 1550 nm with 15 kW peak power, and 25 ps pulse duration in intensity. A 25 ps pulse was a necessary change to the 0.5 ns of the simulations because a broader, bandwidth limited, input pulse would be so spectrally narrow, that it could not be resolved on the numerical grid - in spite of the high amount of grid points. At a repetition rate of 3 MHz this input pulse corresponds to an input average power of 1.06 W. These pulse and fiber parameters mean that the initial dynamics is based on

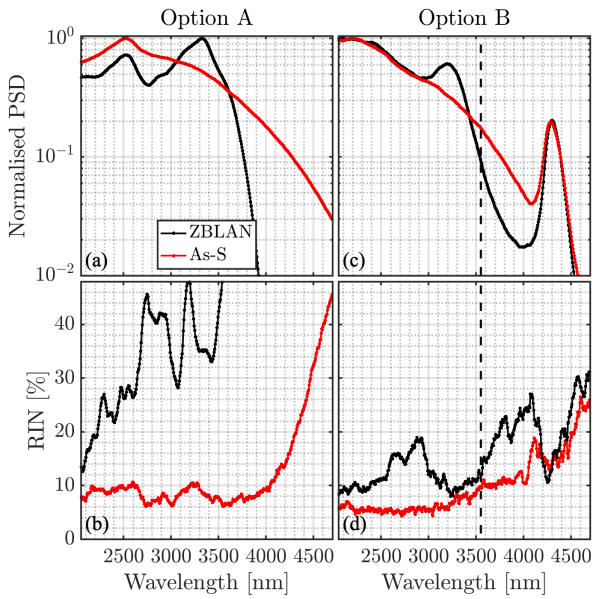

Figure 4.18: Simulated spectra and RIN curves. A running average with a bandwidth of 18 nm has been applied to the PSD so that the simulated data corresponds to the measured data. The vertical dashed line in option B shows the ZDW.

MI and soliton dynamics, such that good resemblance with the experiment is achieved.

3. The fiber lengths of ZBLAN fibers was set to 10 m for ZBLAN A and 2 m for ZBLAN B to develop the spectra to a point where they matched the experimentally observed ones. Finally, a 40 % coupling efficiency with no spectral dependence was assumed between the ZBLAN fibers and the As-S fiber to better match the observed average powers at the output

The simulations use $N_t = 2^{19}$ temporal points separated by 1.5 fs, and a central angular frequency of $\Omega_0 = 2\pi \cdot 350 \cdot 10^{12}$ rad $\cdot$ s$^{-1} \approx 857$ nm. At the input to the silica fiber, 1% input RIN and one-photon-per mode noise [42] were included in an ensemble consisting of 50 simulations. A running average with a bandwidth of 19 nm has been applied to the results to make it more comparable to the experimental results.

Simulated results are shown in Figure 4.18, that correspond to the measured results in Figure 4.16. There is generally good agreement between the results. The output of ZBLAN A spans to approximately 4 μm, and we shall see that it consists of many solitons. Significant spectral broadening is observed in the As-S fiber in this case, which is not in agreement with the experiments, but is in good accordance with what is often seen in the literature [58, 59]. Even stronger noise reduction is observed in the simulations than in the experiment, which probably comes from the same reason as the much stronger spectral broadening, which is unfortunately not known exactly.

The stronger noise reduction in the simulations indicate that there is a potential for optimising the cascade to reach even better noise reduction.

In ZBLAN B a DW peak is generated similarly to the experiment, although it is much more narrow. A possible reason for this could be that the core radius of the ZBLAN fiber is not exactly constant, which means that the ZDW changes during propagation, resulting in a z-dependent phase matching. Furthermore, the CO_2 absorption lines are, of course, not present as there is no free space part in the simulations. Contrarily to the experiment, there is actually a change in the spectral shape in the As-S fiber in the simulations. Most significantly, there is a peak around 3.2 μm in the ZBLAN spectrum that is spread out spectrally in the As-S fiber, such that the dip in the spectrum is partially filled out. This effect is also reflected in the simulations where there is significant noise reduction in the spectral regions on both sides of the peak in the ZBLAN fiber. The RIN at the DW remains unaffected by the As-S fiber which is in good agreement with the experiment.

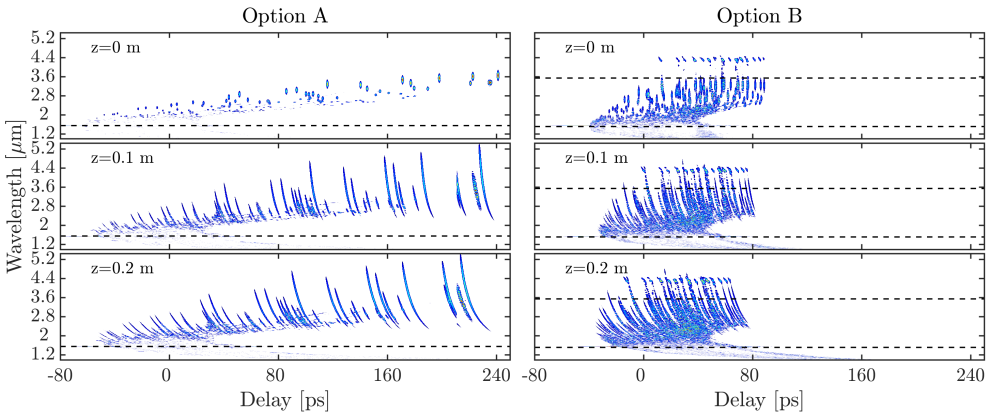

Figure 4.19: Spectrogram series showing the dynamics in the As-S fiber in option A (left) and option B (right). The spectrograms are calculated with a window width of 0.5 ps. The horizontal dashed lines show the ZDWs of the ZBLAN fibers.

In Figure 4.19, the purpose of the simulations is shown: A breakdown of the nonlinear dynamics in the As-S fiber in spectrograms, such that the two noise reduction mechanisms can be illustrated clearly. In the left column the dynamics in option A is shown. At the input there is a set of temporally and spectrally distributed pulses, that were solitons in the ZBLAN fiber. After just 10 cm of propagation the solitons have broadened spectrally, such that there is a significant spectral overlap between each soliton. Between 10 cm and 20 cm there is only limited broadening and instead the broadened pulses are just temporally dispersed - more quickly at shorter wavelengths. This shows, that only few centimetres of fiber - or as short as what can practically be handled - are necessary to achieve the noise reduction. If the pulses are allowed to propagate further they would start temporally overlapping with each other, until they initiate the collective redshift described in section 4.1.

In option B the input is much more localised temporally, due to the lower magnitude

of dispersion and the shorter length of ZBLAN fiber B. The region between the two ZDWs is anomalous dispersion. A collection of DWs have been created across the ZDW and a dip in power between the DWs and the remaining spectrum is clearly seen. In anomalous dispersion, a lot of pulse-like structures are present still, and after 10 cm of propagation, many of these have broadened spectrally. This effect was not present in the experiments, which suggests that the remainders of the solitons in anomalous dispersion in the experiment had lower peak power at the output of the ZBLAN fiber. Between 10 cm and 20 cm, there is once again no more spectral broadening, and in this case also much slower temporal "compression" due to the lower magnitude of the dispersion. The spectrograms underline the importance of having a large number of high peak power solitons at the input for efficient noise reduction.

This concludes the chapter on cascaded SC generation. Cascaded mid-IR SC generation is enabling for mid-IR OCT, which is the topic of the next two chapters. The results in this chapter have significant relevance for mid-IR OCT: The collective redshift shown in section 4.1 and the tunable aspect of it allows to target the majority of the SC power to the spectral range that is relevant for an OCT system. Furthermore, any noise reduction of the SC source will result in improved sensitivity in OCT, which will allow sharper images and/or a reduction in integration time, and thereby open the door to a bigger set of imaging applications.

CHAPTER 5

Optical Coherence Tomography

Since OCT was first introduced in 1991 [3], it has seen a significant development. The application of OCT in medical imaging, as a tool performing an "optical biopsy" has spearheaded the development [79]. Of particular importance for the development of OCT is the application in ophthalmology, which was realised ex-vivo already in the first OCT paper [3], and in-vivo already 2 years later [80, 81]. The application of OCT in dermatology is of growing interest [4], and is also being pursued in our own research group [82]. In 1996 it was shown that tissue imaging with OCT is optimal at 1300 nm, rather than the 800 nm region that was used for ophthalmic imaging due to reduced scattering [83]. Generally, the optimal centre wavelength of an OCT system depends on the sample under consideration. A few examples of this include: spectroscopic analysis of nano layers in semiconductor devices and stacks of 2D materials using UV OCT [84], true colour spectroscopic OCT of paint layers in art by using visible colours [36], the ability to penetrate paint layers with high sensitivity using near-IR light [85], and further improved penetration of paints and coatings by using mid-IR light [86]. A comparison of five different OCT centre wavelengths ranging from 800 nm to 1700 nm showed better penetration at longer wavelengths in both plastic, rubber and enamel [87]. On our own OCT system with a centre wavelength at 1270 nm, we have shown more than 0.2 mm penetration in tooth enamel as shown in Figure 5.1.

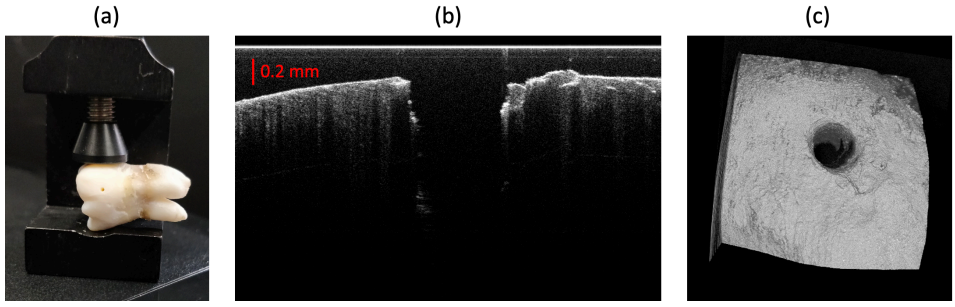

Figure 5.1: OCT image of tooth using a centre wavelength of 1270. (a) Photograph of tooth in sample holder, where drill hole is visible. (b) B-scan of tooth. (c) Full OCT volume of tooth seen from above the drill hole.

Assuming that imaging is not limited by wavelength dependent sample absorption,

it is a general trend that scattering reduces as $\frac{1}{\lambda^4}$, which leads to better penetration of samples for longer wavelengths. However, using a longer centre wavelength comes at a significant cost in terms of both axial resolution, δz, and transverse resolution, δx, given by

$$\delta z \propto \frac{\lambda_c^2}{\Delta\lambda}, \quad \delta x = 0.37\frac{\lambda}{\mathrm{NA}}, \quad \mathrm{DOF} = \frac{0.884\lambda}{\left(\sqrt{1-\mathrm{NA}} - \sqrt{1+\mathrm{NA}}\right)^2}, \tag{5.1}$$

where NA is the numerical aperture of the imaging lens.
The axial resolution is especially reduced by going to longer wavelengths, although it also allows a light source with a broader FWHM bandwidth $\Delta\lambda$, such that part of the loss in axial resolution can be compensated. The constant of proportionality in the axial resolution depends on the shape of the spectrum, for a Gaussian shape it is ≈ 0.44, and for a square shape it is ≈ 0.6. As longer wavelength light typically results in a larger depth of field (DOF) of the imaging lens, a good synergy exists with the improved penetration. Better lateral resolution is provided by using a higher NA lens, however this decreases the DOF. This limitation can be partially avoided by using non-Gaussian imaging optics such as Bessel beams [88], by using multiple foci [89], or using numerical refocusing [90].

5.1 Principle of OCT

As a mature technology OCT has been developed in several modalities, such as time-domain (TD) operation as described in section 5.1.2, spectrometer based OCT as described in 5.1.3, and swept source (SS) OCT as described in section 5.1.4. While the processing of each A-scan differs between the modalities, the A-scan itself is the same. B-scans consist of multiple A-scans, while a C-scan is multiple B-scans. Once a C-scan is acquired an "en-face" image showing a single depth at a time can be generated. A simple model of the OCT A-scan is given in the next section.

5.1.1 The OCT A-scan

This section will show a brief derivation of the OCT A-scan. The derivation is based on the derivation provided in Chapter 2 in [4]. Consider the OCT system shown in Figure 5.2 along with a complicated sample. The laser source provides broadband pulses with an electric field which, at the beam splitter, is given by $s(k)E_0$, where $s(k)$ describes the spectral shape, and E_0 the amplitude. A 50/50 beam splitter directs half of the intensity at the sample, and the other half at a reference mirror, before combining the beams again. The sample consists of a number of point reflectors located at position z_n with reflectivity $r_n = \sqrt{R_n}$, such that the sample reflectivity $r_s(z)$ can be expressed as.

$$r_s(z) = \sum_{n=1}^{N} r_n \delta(z - z_n) \tag{5.2}$$

A round trip starting from the beam splitter and returning once again from the sample, assuming only a single reflection at each interface, results in the light picking up the

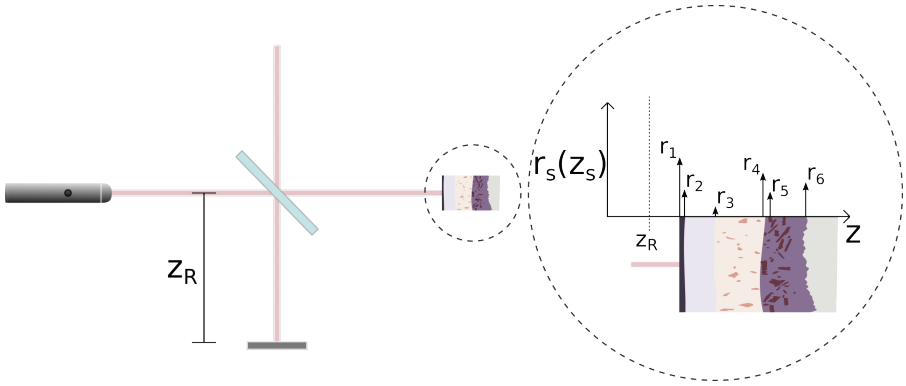

Figure 5.2: OCT system showing the presence of a complicated sample. The sample consists of several layers, and at the interface between each layer there is a point reflection.

phase of $\phi = 2kz$. In this expression it is assumed that each layer in the sample share the same refractive index. Thereby, the electric field returning to the beam splitter from the sample arm is given by

$$E_S = \frac{E_0}{\sqrt{2}} s(k) \sum_n^N r_n e^{i2kz_n} \tag{5.3}$$

The reference arm consists of only a single mirror at position z_R with reflectivity $r_R = \sqrt{R_R}$. Such that the field returning from the reference arm is

$$E_R = \frac{E_0}{\sqrt{2}} s(k) r_R e^{i2kz_R} \tag{5.4}$$

After a second pass through the beam splitter, the measured intensity is given by

$$\begin{aligned} I(k) =& \frac{1}{2}|E_S + E_R|^2 \\ =& \frac{E_0^2 S(k)}{4}\Big[R_R + r_n r_m^* \sum_n^N \sum_m^N e^{i2kz_n} e^{-i2kz_m} + \text{C.C} \\ &+ r_R e^{i2kz_R} \sum_n r_n^* e^{-i2kz_n} + \text{C.C}\Big], \end{aligned} \tag{5.5}$$

Where $S(k) = \left|s(k)^2\right|$. The complex exponentials and their complex conjugates can be collected in cosine terms, while the terms where $n = m$ have cancelling phases in the

exponentials, such that they simply evaluate to $R_1 + R_2 + ... + R_N$:

$$\begin{aligned} I(k) = & \frac{E_0^2 S(k)}{4} \Bigg[R_R + R_1 + R_2 ... R_N \qquad \text{DC} \\ & + \sum_{n \neq m=1}^{N} \sqrt{R_n R_m} (\cos(2k(z_n - z_m))) \text{ Auto correlation} \\ & + 2 \sum_{n=1}^{N} \sqrt{R_R R_n} (\cos(2k(z_R - z_n))) \Bigg] \text{ Cross correlation.} \end{aligned} \tag{5.6}$$

The three terms have been labelled "DC", "auto correlation", and "cross correlation". The reason for the naming will become obvious in the following section. It is relevant to look at the case of a single mirror in the sample arm, as this is so often used to characterise OCT systems. In this case only one sample arm term, R_S, persists in the DC term, the auto correlation term vanishes, and only one term remains in the cross correlation term, such that equation 5.6 is reduced to

$$I(k) = \frac{E_0^2 S(k)}{4} \left[R_R + R_S + 2\sqrt{R_R R_S} \cos(2k(z_R - z_S)) \right] \tag{5.7}$$

In the general case the sample arm signal is unknown, however the reference arm signal, $I_R(k) = \frac{E_0^2 S(k)}{4} R_R$, can be measured once and for all, such that most of the influence of the reference arm can be removed by

$$I_{\text{norm}} = \frac{I(k) - I_R(k)}{\sqrt{I_R(k)}} = \frac{E_0 s(k)}{2} \left[\frac{R_S}{\sqrt{R_R}} + 2\sqrt{R_S} \cos(2k(z_R - z_S)) \right]. \tag{5.8}$$

Equations 5.6 and 5.8 have made no assumption on how the light is measured or how the source light is provided. The different choices of light source and detection is treated explicitly in sections 5.1.2-5.1.4.

5.1.2 Time-domain OCT

The first OCT systems worked in the time-domain [3]. In the time domain the entire spectrum is measured on a single photo detector. The reference arm is scanned to probe the entire sample. Such that each A-scan is acquired point by point. This typically means that time-domain OCT is quite slow compared to Fourier domain OCT.

5.1.3 Spectrometer based OCT

As the mid-infrared (IR) OCT system is spectrometer based, a more thorough discussion of the analysis and interpretation is relevant in this case.

The scanning of the reference arm mirror in TD OCT imposes a severe limitation to the imaging speed of TD OCT. Spectrometer based OCT was introduced in 1995 to remedy this [91]; an entire A-scan is measured at once by encoding the depth information in the period of the interference signal. It was later shown that the spectrometer

based design additionally provided an increase in signal-to-noise ratio (SNR) proportional to the number of photo diodes in the spectrometer [92]. In one analysis, it was shown that the sensitivity increase in Fourier-domain (FD) OCT compared to TD OCT, given as the ratio between SNR and integration time, can amount to more than 20 dB [93]. FD domain describes both spectrometer based OCT and SS OCT.

The A-scan in real space is calculated through the inverse Fourier transform of equation 5.6 and the measured A-scan amounts to

$$\begin{aligned} I(z) \propto\ & E_0^2[\gamma(z)[R_R + R_1 + R_2 + ...R_n]] && \text{DC} \\ & + E_0^2 \sum_{n\neq m=1}^{N} \sqrt{R_n R_m}[\gamma[2(z_n - z_m)] + \gamma[-2(z_n - z_m)]] && \text{Auto correlation} \\ & + 2E_0^2 \sum_{n=1}^{N} \sqrt{R_R R_n}[\gamma[2(z_R - z_n)] + \gamma[-2(z_R - z_n)]] && \text{Cross correlation} \end{aligned} \tag{5.9}$$

Where $\gamma(z)$ is the inverse Fourier transform of the source spectrum $S(k)$. It shows directly how the signal from a point reflector is broadened to the width of $\gamma(z)$, which means that $\gamma(z)$ can be considered the point-spread function of an OCT system. Each interference term appear at both positive and negative OPD, as the Fourier transform cannot distinguish between the two. This leads to a decrease in the imaging depth by a factor of 2, as both positive and negative OPD has to be resolved.

Three different terms appear in the measured signal:

- **DC:** The DC term appears at $z = 0$ with the width of $\gamma(z)$. It consists of a pure reference arm term along with N terms from the sample - one from each interface. The reference arm term is proportional to the reflectance of the reference arm mirror R_R, and the N sample arm terms are proportional to the reflectance of the corresponding reflector. In most samples the reflectance of all sample arm terms is much lower than the reflectance of the mirror in the reference arm, such that R_R dominates the DC term. However, with the normalisation described in equation 5.8, the dependence on the reference arm can be completely removed from this term.
- **Auto correlation:** The auto correlation terms are proportional to the product of the square root of the reflectance of different sample reflectors. The auto correlation terms appear in the images at distances $2(z_n - z_m)$ from zero OPD, which means that they can be easily recognised as terms that do not move when the OPD is changed by varying the sample or reference arm length.
- **Cross correlation:** The cross correlation terms are the desired terms in OCT, as they contain information about the depth of each sample interface. The cross correlation terms are much stronger than the auto correlation terms in most samples, for the same reasons as for the sample terms in the DC case, namely that $R_n \ll R_R$.

A spectrometer uses a diffraction grating to spatially resolve the incoming light, which is then measured on a line-array of photo diodes. It is similar to the monochromator

design shown in Figure 4.13, if an array of diodes were positioned instead of the output slit of the monochromator. In a ideal grating, the diffraction angle varies linearly with wavelength, which means that the pixels in an ideal spectrometer are linearly spaced in wavelength by $\delta\lambda$ [23]. The FFT requires an array that is linearly spaced in wave number, k, which means a numerical mapping is needed between wavelength and wave number. If the line camera in the spectrometer has M pixels, the mapping results in an array with M elements with spacing δk. The mapping is measured by placing a mirror in the sample arm, measuring an interferogram at two different OPDs, and extracting the phase shift between them. Any unbalanced dispersion in the interferometer, such as the one introduced by the lens in the sample arm, is typically numerically compensated for, simultaneously. This defines a physical sampling resolution of

$$\delta z_{samp} = \frac{\pi}{M\delta k} \approx -\frac{\lambda_0^2}{2M\delta\lambda}, \tag{5.10}$$

where λ_0 is the central wavelength of the spectrometer, and the approximation $\delta k \approx -\frac{2\pi\delta\lambda}{\lambda_0^2}$ was applied.
The defining parameters of the spectrometer should be chosen such that the digital sampling resolution is better than the axial resolution defined by the light source given in equation 5.1. As the FFT results in an equivalence between positive and negative OPD the total imaging depth, z_{max}, becomes

$$\pm z_{max} = \pm\frac{M\delta z_{samp}}{2} \approx \pm\frac{\lambda_0^2}{4\delta\lambda}. \tag{5.11}$$

The finite spectral width of each pixel means that the ability to properly resolve an interference signal falls off with the frequency of the signal, which in OCT is equivalent to the OPD. Therefore, the best sensitivity in spectrometer based OCT is achieved close to the top of the image. This effect is referred to as sensitivity roll-off [4, 94], and for a Gaussian shaped spectrum the roll-off function, $RO(z)$, is given by

$$RO(z) = \mathrm{sinc}^2(\zeta)\exp\left[\frac{-\zeta^2}{2\ln(2)}\frac{\delta\lambda_s^2}{\delta\lambda^2}\right], \quad \zeta = \frac{\pi z}{2z_{max}}, \tag{5.12}$$

where $\delta\lambda_s$ is the resolution of the spectrometer. The resolution of a spectrometer is defined as the FWHM of the measurement of a monochromatic light source. The roll-off function is multiplied to the OCT A-scan, which results in a significant loss in sensitivity for high OPD.

5.1.4 Swept source OCT

In SS OCT the broadband light source is replaced by a SS laser, and the spectrometer is replaced by a single photo detector. As the wavelength of the SS laser is swept in time, the first step in SS OCT is to translate from time to instantaneous wavelength of the laser. As only a single photo detector is required in SS OCT, balanced detection of the signal can be achieved. Balanced detection allows removal of auto correlation terms by recording the interference signal with a $\pi/2$ phase shift between the two channels.

Furthermore, it has been shown to provide an increase in sensitivity [95]. Balanced detection with spectrometers is a difficult task, where the extra price and complexity is often not worth the effort, although it has been shown to provide the same advantages as in SS OCT [96].

SS OCT was first introduced in 1997, just two years after spectrometer based OCT [97]. It was initially limited by the sweep rate of the laser. The sweep rate is often the same as the A-scan rate, in contrast to spectrometer based OCT where the integration time of the spectrometer is typically much longer than the pulse separation of the source. The current SS laser technology allows MHz A-scan rates with more than 100 nm bandwidth [98, 99]. To the best of my knowledge the highest A-scan rate in OCT is 40 MHz which is achieved by temporally stretching an SC spectrum.

In SS OCT the impact of roll-off is typically reduced significantly compared to spectrometer based OCT. This is evident, by looking at the factor $\frac{\delta\lambda_s^2}{\delta\lambda^2}$ from equation 5.12. In an SS OCT system the factor $\delta\lambda_s$ instead represents the instantaneous line width of the laser source, while the sampling resolution, $\delta\lambda$, is related to the sweep rate and the digitisation rate. The instantaneous linewidth of SS lasers can be much narrower than the pixel spacing in spectrometer. Thereby, the SS OCT data acquisition can be designed to reduce the impact of roll-off, although often at the expense of the A-scan rate [100, 101].

SS lasers are still limited by bandwidth, which cannot compare with the bandwidth that can be delivered by an SC laser source at any wavelength. A single PCF based SC laser source from NKT photonics can cover the bandwidth 390-2400 nm [1], which to the best of my knowledge spans past all SS based OCT systems reported [102]. Furthermore, SC laser sources are moving both into the UV [40, 103], and mid-IR [15, 59], allowing imaging of a much broader range of samples.

It is worth noting, that a data analysis approach exists, that avoids the Fourier transform, but instead calculates the cross-correlation of a measured interferogram with a set of pre-gathered mirror interferograms at different OPDs. The strength of the cross correlation is then the amplitude of the A-scan at each OPD. This approach allows much faster processing of en-face images, as the calculation can focus on a specific depth in the sample [104, 105].

With the fundamentals of OCT in place, I will now present the state-of-the-art in mid-IR OCT before showing the capabilities of mid-IR OCT in paper thickness monitoring and quality control in section 5.3.

5.2 Mid-IR OCT

Initially, OCT was developed at near-IR and visible wavelengths, due to the availability of lasers and detectors, and because of the applications within medical imaging [4, 82]. However, the improved penetration potential at longer wavelengths has been realised within the last 15 years by several groups. In 2007 a quantum cascade laser produced

[1]Website: https://www.nktphotonics.com/products/supercontinuum-white-light-lasers/superk-fianium/

a spectrum spanning $6 - 8$ μm, with holes in some parts of the spectral range, and a repetition rate of 15 kHz [106]. This allowed 30 μm axial resolution, and 30 dB sensitivity at an A-scan rate of approximately 1 Hz. A liquid nitrogen cooled Mercury-Cadmium-Tellurite detector was used.

Although SS lasers are also moving into the mid-IR [107], the current state of the art in mid-IR OCT imaging uses SC laser sources [10, 86, 108–111]. The major difference of all the SC based systems, is the manner in which the light is detected. In [108] a sensitivity of 81.7 dB was reported at an A-scan rate of 100 Hz with a pyroelectric array detector. In [109] they used a nonlinear crystal to generate mid-IR light from an 800 nm laser inside the interferometer, such that the mid-IR light illuminated the sample, but was interfered with 800 nm light which was then detected with a efficient charge coupled device (CCD) sensor. A sensitivity of 69 dB was achieved with an A-scan rate of 1 Hz, but importantly only 90 pW of power illuminating the sample. In [110, 111] they used a single InAsSb point detector after a grating and a galvoscanner, such that the spectrum is scanned in time on the detector. A sensitivity of 80.17 dB was achieved at an A-scan rate of 25 Hz.

First publication (year)	λ_c	Δz	Sens	A-scan/s	Sens/s
Cooley et al. (2007) [106]	7 μm	30 μm	30 dB	1 Hz	30 dB
Zorin et al. (2018) [108]	4 μm	50 μm	82 dB	100 Hz	102 dB
Israelsen et al. (2019) [10, 86]	4 μm	8.6 μm	60 dB	330 Hz	85 dB
Vanselow et al. (2020) [109]	3.8 μm	10 μm	69 dB	1 Hz	69 dB
Israelsen et al. (2021) [VI]	4 μm	6 μm	65 dB	3333 Hz	100 dB
Zorin et al. (2021) [110, 111]	3.7 μm	7.6 μm	80 dB	25 Hz	94 dB
Current work [II]	4 μm	11.9 μm	60 dB	3333 Hz	95 dB

Table 5.1: Performance parameters for selected works in mid-IR OCT. λ_c is the centre wavelength of the source, Δz is the axial resolution, Sens is the reported sensitivity, while Sens/s is the reported sensitivity normalised by the A-scan rate.

The OCT performance parameters for selected mid-IR OCT systems are given in table 5.1. To better compare the sensitivity of the systems, a time-normalised sensitivity is given in the last column. The time-normalised sensitivity is calculated as

$$\text{Sens/s} = \text{Sens} + 10\log_{10}(\text{A-scan/s}). \tag{5.13}$$

Our mid-IR OCT system is shown in Figure 5.3. The illuminating light source is slightly different than the SC laser source reported in [10, 86], hence the difference in performance parameters as reported in table 5.1.

The new SC laser source is the one described as Option B in Section 4.2 with a spectral edge at 4500 nm. The laser is coupled to a free-space Michelson interferometer with a reflective collimator. The spectrum below 3.2 μm is filtered away with a long pass filter. In the sample arm approximately 18 mW of average power is left. A galvoscanner in the sample arm allows 3D imaging using either a 30 mm or 75 mm AR coated BaF_2 lens. A 5 mm BaF_2 window is placed in the reference arm to crudely compensate the dispersion introduced by the lens in the sample arm. In our OCT

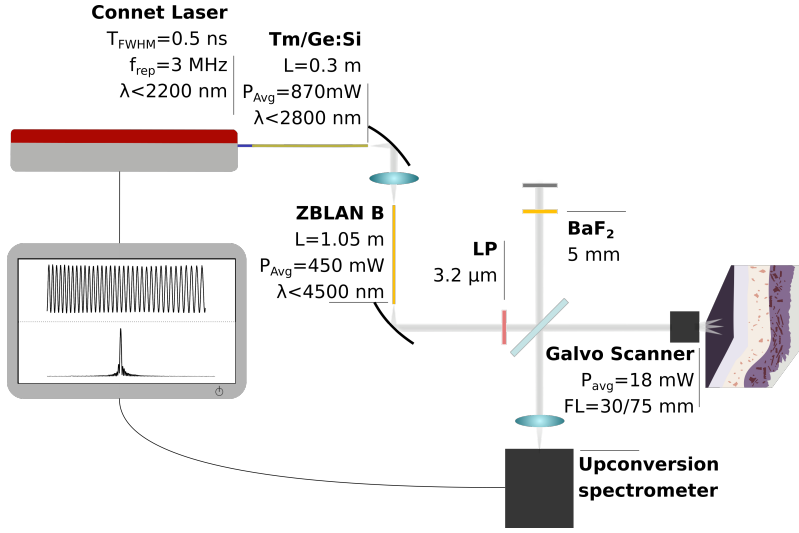

Figure 5.3: The entire mid-IR OCT setup. The SC laser source is the one described as "Option B" in Section 4.2. The laser source is coupled to a Michelson interferometer. A long pass filter (LP) is used to remove the part of the spectrum that is not used in the imaging. A galvoscanner in the sample arm allows fast volume imaging. The imaging lens is either 30 mm or 75 mm focal lenght (FL) $2-5$ μm AR coated BaF_2 lens. A 5 mm BaF_2 window is placed in the reference arm to compensate for the dispersion of the imaging lens in the sample arm. The output of the interferometer is coupled into an upconversion module, which converts to near-IR, such that the spectrum can be measured with a commercial complementary metal-oxide-semiconductor (CMOS) camera.

system the light is detected with a CMOS camera in the spectral range 796-879 nm with 4096 pixels. Light is converted to the near-IR range by sum frequency generation (see e.g. [112]) with a 1064 nm laser. Finally, the measured interferograms are normalised, linearised in wave number, dispersion compensated and Fourier transformed on a computer.

5.2.1 Characterisation of the OCT system

As the SC laser and imaging lens in the system are different than in the last reporting of the system parameters, given in [VI], it is worth doing a full system characterisation, which is given in Figure 5.4. The characterisation consists of the axial resolution **(a)-(b)**, lateral resolution **(c)**, noise analysis **(d)**, and sensitivity roll-off **(e)**. The measurement and results of each quantity is outlined in the following:

- **(a-b) Spectrum and axial resolution:** To measure the axial resolution a mirror is placed in the sample arm. Assuming that the mirror is a perfect delta-function reflector, the width of the A-scan will give the axial resolution. The full interference spectrum and reference spectrum is shown in **(a)**. The spectrum

spans from approximately 3.6 μm to 4.6 μm. Approximating the spectrum to be square shaped this gives a theoretical axial resolution of 10.1 μm. In **(b)** the A-scan obtained from the interference data in **(a)** is shown. The sampling resolution is $\delta z_{samp} = 4.37\ \mu m$, and the imaging range is $z_{max} = 8951.5\ \mu$m. To properly resolve the A-scan, the numerical array is zero-padded to an 8 times longer length, which gives a sampling resolution of 0.55 μm. The axial resolution is the FWHM of the A-scan, which is $\delta z = 11.9\ \mu$m. The four dashed lines in **(a)** are the wavelengths at which the noise analysis is performed in **(d)**.

- **(c) Lateral resolution:** The lateral resolution was measured on a 1951 USAF resolution target, and the 70 mm focal length imaging lens. A full volume scan is performed, from which the resolution can be evaluated on an en-face image. The en-face image shows several of the group 3 elements. The intensity along the red and black lines are shown on the right. The smallest resolvable elements are marked by shaded regions. In the horizontal direction element 6 can be resolved, and in the vertical direction element 4 can be resolved corresponding to lateral resolutions of 70 μm and 88.5 μm, respectively.

- **(d) OCT noise:** The noise is characterised by measuring the signal in the reference arm only. The variance of the measured data depends heavily on the total measured power. The total measured noise, σ_{tot} in each wavelength bin, represented by its spectrometer pixel index, i, in SC based OCT, is given by [113]

$$\begin{aligned} \sigma_{tot}^2[i] &= \sigma_{r+d}^2[i] + \sigma_{shot}^2[i] + \sigma_{ex}^2[i] \\ \sigma_{shot}^2[i] &= \frac{\eta(P_{ref}[i] + P_{sam}[i])\tau}{\hbar\omega[i](\Delta e)^2} \\ \sigma_{ex}^2[i] &= \left(\frac{\mathrm{RIN}[i](P_{ref}[i] + P_{sam}[i])\eta\tau}{\hbar\omega[i]\Delta e}\right)^2, \end{aligned} \tag{5.14}$$

where σ_{r+d} is read-out and dark noise from the camera, which consists of noise in the dark signal, and errors in the digitisation. The read-out and dark noise is independent of the light source. Shot noise, σ_{shot}, is the ideal noise in OCT, as it has no dependence on the RIN of the laser source, and therefore cannot be avoided by improving the noise performance of the laser. The shot noise depends on the quantum efficiency, η, of the spectrometer, the integration time, τ, the reference and samples arms powers, P_{ref} and P_{sam}, the angular frequency of the light, ω, and a dimensionless gain factor of the spectrometer Δe. The last noise term is the "excess noise", which comes from fluctuations in the laser source. As previously discussed in section 4.2 the MI and soliton based SC sources have high RIN, and therefore this noise term is often a limiting factor in SC based OCT systems. Recently, shot noise limited OCT imaging was shown with an ANDi SC laser source [60].

Shot noise limited OCT represents OCT where the total variance has a linear dependence on the reference arm power (assuming that $P_{sam} \ll P_{ref}$). Whereas, excess noise limited OCT shows a quadratic dependence on the reference arm

power. The sensitivity in OCT is defined by the smallest reflection that can be resolved. The sensitivity is typically given in dB, and it is given by

$$\mathrm{SNR}_{\mathrm{OCT}} \equiv 10\log_{10}\left(\mathrm{SNR}^2\right) = 10\log_{10}\left(\left(\frac{\max(\text{A-scan})_{\mathrm{lin}}}{\sigma_{tot}}\right)^2\right) \tag{5.15}$$

Where the total noise is measured with the sample arm closed off, and where a suitable average is taken over the index, i. From equation 5.9 it is seen that the max of each A-scan scales as $E_0^2 \propto \sqrt{P_{ref}P_{sam}}$. Therefore, turning up the reference arm power while in the excess noise regime reduces the SNR by a factor $\frac{1}{\sqrt{P_{ref}}}$, while there is no influence in the shot noise limited regime, and a positive impact in the read-out and dark noise limited regime by a factor of $\sqrt{P_{ref}}$.

In **(d)** the noise performance is shown for the mid-IR OCT system, at the four wavelengths marked in **(a)**. The considered wavelength is given as the title in each sub-figure. Two different noise regimes can be seen for each wavelength. For low counts on the x-axis the variance is independent of the mean, which shows that the noise is in the read-out and dark noise regime. For high counts the noise is in the excess noise regime, shown by a good fit to the data by curve proportional to P_{ref}^2. The optimum reference power is at the intersection of these two regimes. This point is marked in each subplot, and in all cases it turns out to be between 35 and 42 counts. The reference arm power can be adjusted by slightly angling the reference arm mirror, such that the coupling is suboptimal. Taking this into consideration a sensitivity of 60 dB was obtained at an A-scan rate of 3333 Hz.

- **(e) Roll-off:** The roll-off is measured with a mirror in the sample arm. The same A-scan is then measured with varying reference arm lengths, such that the amplitude of the A-scan can be tracked as a function of the OPD. The dashed line shows the amplitude of the A-scan at shortest OPD. The peak of the A-scan is reduced by 6 dB at 3.9 mm OPD, which is indicated by a double arrow.

This concludes the characterisation of the OCT system. In the next section, the application of the system in paper thickness and quality monitoring, as reported in [II] will be discussed.

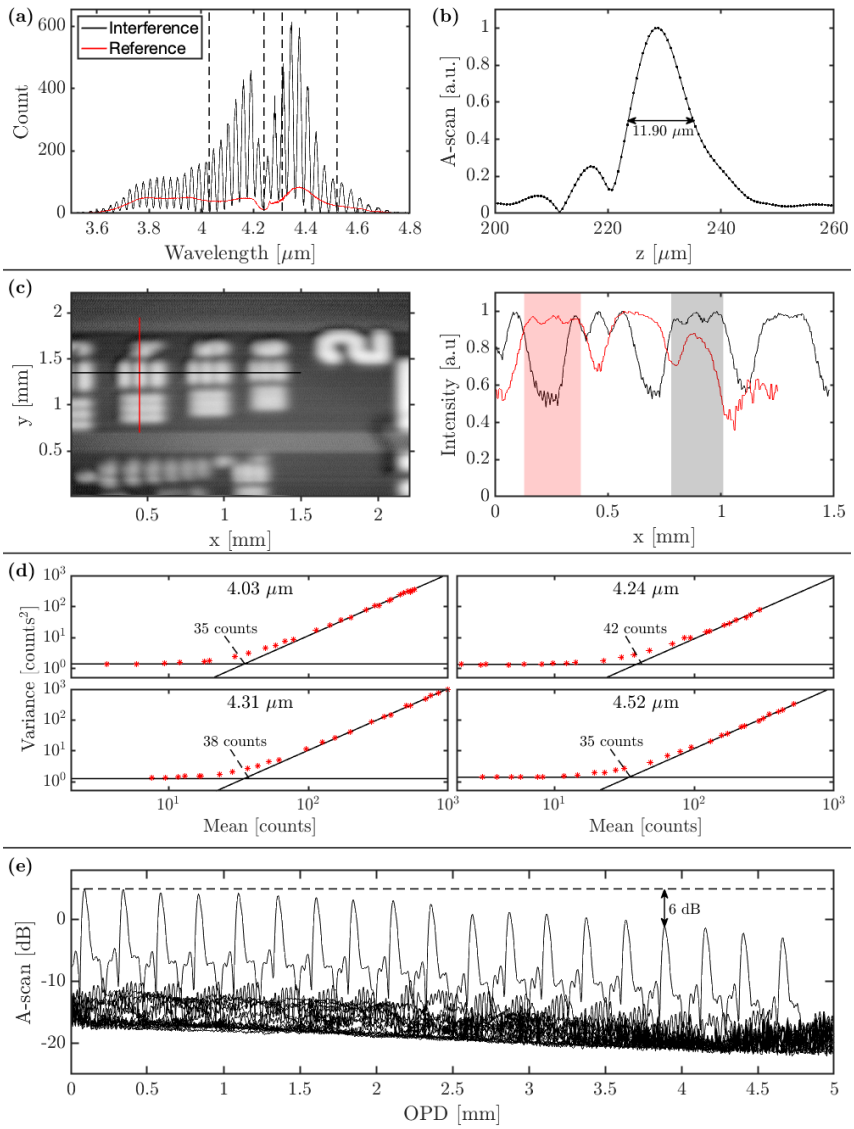

Figure 5.4: Characterisation of the mid-IR OCT system, acquired in collaboration with Coraline Lapre. **(a)** interferogram of a mirror in sample arm, and corresponding reference spectrum. The dashed vertical lines show the specific wavelengths considered in **(d)**. **(b)** A-scan corresponding to the interferogram in **(a)**. The FWHM of this A-scan is the axial resolution of the system. **(c)** En-face image of a 1951 USAF resolution target. The intensities along the red and black lines are shown on the right. The red and grey shaded areas show the region of the smallest resolvable features along the vertical and horizontal directions, respectively. **(d)** Noise analysis of the reference arm showing the dependence of the variance in the data on the mean at four selected wavelengths as indicated in **(a)**. The two black lines in the plot show fits to the data assuming read-out and dark noise (flat), and excess noise (P_{ref}^2). The point at which excess noise starts dominating is marked for each wavelength. **(e)** Roll-off curve showing the loss in sensitivity as a function of the OPD. At 3.9 mm the peak value has fallen by 6 dB as shown by a double arrow.

5.3 Non-Contact Paper Thickness and Quality Monitoring, Paper [II]

The non-destructive, non-contact nature of OCT, along with the improved penetration at longer wavelengths makes mid-IR OCT a promising tool for in-line manufacturing monitoring [111]. A good example of the need for real time quality control is in paper manufacturing.

Ideally, paper thickness monitoring can be done in a non contact fashion, as the contact can lead to tears or other defects [114]. However, the most precise measurements were initially based on magnetic reluctance measured with contact on both sides. Later it was shown that laser triangulation could accurately determine in-line changes in paper thickness with only single-sided contact, although the absolute value of the thickness depended on the roughness of the paper [115]. Previous studies of OCT based paper thickness monitoring were based on near-IR sources. Scattering was a limiting factor, and in one study they investigated paper with an optical thickness (physical thickness multiplied by refractive index) of 65 μm [116], and in another study benzyl-alcohol acted as a "clearing agent" to better penetrate the paper [117].

In the paper [II] we investigated the ability of OCT and THz time domain spectroscopy to monitor paper thickness with non-contact measurements. With mid-IR OCT, a measurement of the paper thickness can be performed with single sided contact, while the imaging system has no contact with the paper sample. Furthermore, the thickness and refractive index of the paper can be measured simultaneously if the light can penetrate all the way through the sample, which for our system was the case for paper with a thickness up to 90 μm. It was further shown that OCT can be used for defect detection, in case of a tear in the paper, and the spill of an oil droplet. THz TD spectroscopy has the advantage compared to OCT that it can penetrate through much thicker samples. However, it was found that THz TD spectroscopy did not perform as well as mid-OCT for thin paper samples. My contribution to this paper was on OCT imaging, data analysis, and interpretation. Therefore, I will not give further details on the THz TD measurements here.

5.3.1 Paper samples

The paper samples were provided by the Finnish paper manufacturer Valmet [2]. Optical microscope images of five of the paper samples are shown in Figure 5.5. Additionally to the varying thickness, the paper samples differ widely in composition and finish. Two of the papers are brown packaging paper, and the 256 μm paper has a high gloss surface finish. The thickness as provided by Valmet was supported by measuring the thickness of each paper sample with a digital caliper with an instrument accuracy of 1 μm. Each sample was measured at 6 different locations, which showed significant variation - especially for the thicker paper samples.

[2]Website: https://www.valmet.com/

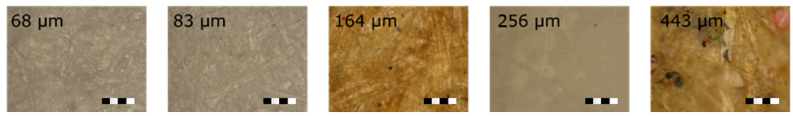

Figure 5.5: Microscope images of five of the paper samples at 20x magnification. The numbers in the top left corner are the reference paper thicknesses. The reference thicknesses were measured with single sided laser triangulation by the manufacturer Valmet. The scale bars are 100 μm.

5.3.2 Paper thickness

The current version of the OCT system, as described in section 5.2, was used for these measurements, using the 30 mm focal length lens. Ideally, the paper thickness is measured by penetrating all the way through the paper. If both air-paper interfaces can be resolved, the optical thickness can be calculated directly as the distance between the two.

The digital sampling uncertainty of the thickness in each A-scan is then $\sqrt{2}\cdot\delta z_{samp} \approx 6$ μm, where the $\sqrt{2}$ comes from the propagation of errors from subtracting two numbers. As the signal from the second interface is much weaker, due to the loss of signal from scattering and absorption inside the paper, it was enhanced by placing the paper samples on a mirror. This means that the measurement is single contact, however the reflection coefficient between paper and the mirror allows thickness measurements of much thicker papers.

The presence of air pockets between the paper and the mirror was hard to avoid, which made the measurements very sensitive to the exact position on the paper where the thickness was measured. To account for the air gap, two different post processing methods were defined, given below as Method 1 and Method 2. Part of the B-scan extended outside the paper such that the actual position of the mirror was known. The reported thickness is then the distance between the top surface of the paper and the mirror. A slightly different method called Method 3 was used for the very thick paper samples, where the presence of air below the paper was impossible to detect as the light could not penetrate the papers.

- **Method 1:** To reduce fluctuations due to noise, a running average of 10 A-scans is first applied. The interface between air and the paper is found as the maximum value of the averaged A-scans, while the interface between the paper and the mirror below is the next peak in the data. The reported paper thickness is the average value of 80-100 A-scans with the uncertainty given by the standard deviation. If it can be ensured that there is no air gap between the paper and the mirror below, this is the preferred method.

- **Method 2:** The interface between air and paper is found in each A-scan without a running average. The paper thickness is reported as the minimum distance between the top interface and the mirror, with the uncertainty calculated as the standard deviation of the minimum value and the 21 neighbouring points.

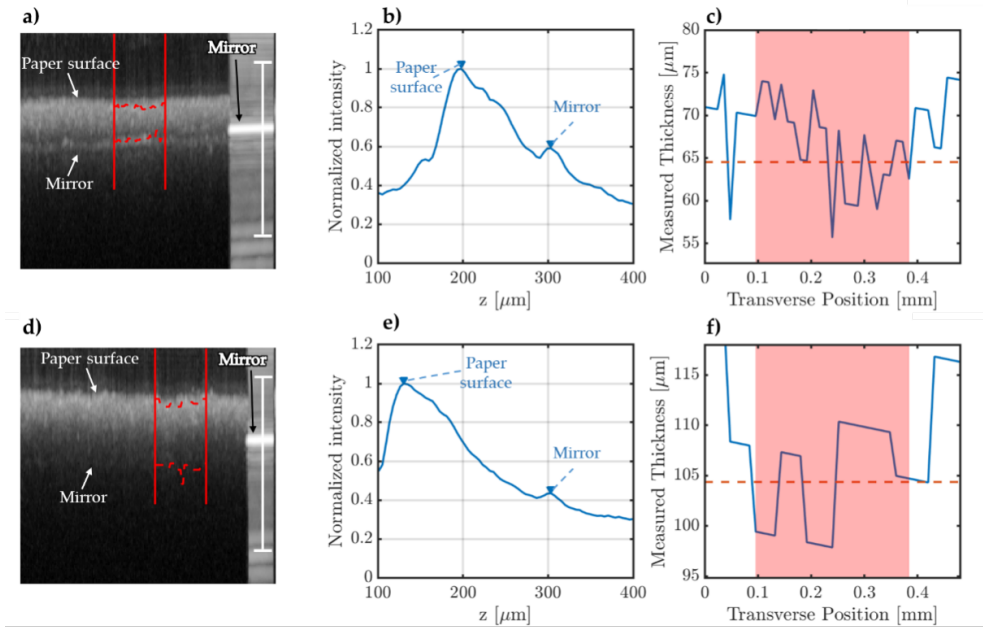

Figure 5.6: Paper thickness measurements for the 68 μm sample **a)-c)**, and the 90 μm sample **d)-f)**. **a)** and **d)** show the maximum pixel projection of 200 B-scans. The white scale bar is 0.5 mm in air. The region marked by two vertical red lines is where the thickness was calculated, and the dashed red lines between them show the extracted position of the paper interfaces. Both images are at the edge of the paper, such that the last A-scan lines show only the mirror. **b)** and **e)** show an average intensity profile across 15 A-scans. The x-axis is optical distance. **c)** and **f)** show the variations of the thickness along the dashed lines in **a)** and **d)**. The shaded regions show the minimum thickness along with the neighbourhood of 21 data points.

Method 2 is less sensitive to an air gap, as the minimum value is likely to find a point, where the paper is in contact with the mirror below. However, it is more sensitive to defects in the paper, surface roughness, and data outliers.

- **Method 3:** The distance between the top of the paper and the mirror next to the paper is the reported thickness with the minimum and maximum measured thickness given as an interval. It is highly likely that Method 3 overestimates the paper thickness, as the presence of air, defects, or a bend in the paper is not easily noticed.

The refractive index could be measured simultaneously with the thickness, when the mirror could be resolved below the paper. Thereby, the optical distance of the paper, as well as the physical distance, could be determined, allowing a calculation of the refractive index as the ratio of the two.

Each thickness measurement consisted of 200 $\times$ 200 A-scans, using a scan area of

2.4×0.4 mm^2, which corresponded to 36 s per measurement. The scan was done as a C-scan to allow averaging over B-scans, and one direction was kept much shorter than the other, such that the averaging over the small direction corresponded to points close to each other. In this way defects, anomalies, and noise could be averaged out while still visualising millimetres of paper.

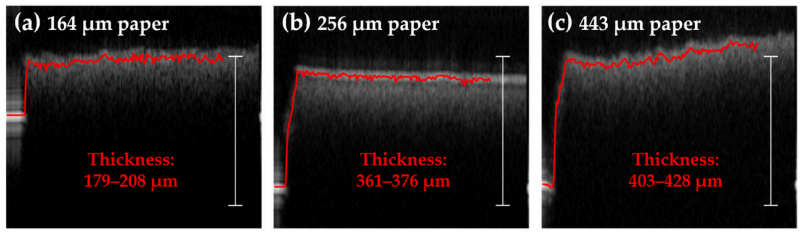

Figure 5.7: Thickness measurement for three thicker papers, that could not be penetrated fully. The reported range in thickness is the minimum and maximum physical distance between the top of the paper and the visible section of mirror. **(a)** is brown packaging paper, **(b)** has a high gloss and very smooth surface surface, and **(c)** is even thicker brown packaging paper. The white scale bars are 0.5mm in air.

The paper thickness measurement and the data processing is shown in Figure 5.6. The top row shows data for the 68 μm sample, and the bottom row for the 90 μm sample. In **a)** and **d)** maximum projections of all the B-scans along the 0.4 mm direction are shown. The paper surface and the mirror below can be resolved in both cases. However, the mirror is only barely visible in **d)**, which means that 90 μm is the limit of where the refractive index can be determined simultaneously. The slope across the B-scan was corrected for by fitting a straight line to the index of the maximum value of the A-scan lines containing the mirror. Each A-scan was then shifted by the amount of pixels dictated by the straight line. In **b)** and **e)** an intensity profile averaged across 15 A-scans is shown. The top surface of the paper is the maximum, while the interface with the mirror is the next peak in the data. The x-axis shows the optical distance, which means that the refractive index can be calculated from the measurement. In the 68 μm case the refractive index was in this way calculated to be 1.33.

The measured thickness as a function of the transverse position are shown in **c)** and **f)**. The transverse positions shown are between the red lines in **a)** and **d)**. The reported thickness and standard deviation uses the data points on the shaded regions. For the 68 μm paper Method 1 results in a thickness of 67.1 ± 2.7 μm, and Method 2 in a thickness of 55.7 ± 5.3 μm. The measurement was performed a total of six times on three different lateral positions on this paper to test for robustness of the analysis. The average value of these six measurements is the reported value in Table 5.2, along with all other thickness measurements, including some of the papers that could not be penetrated, which are shown in Figure 5.7.

Generally, the reference thickness was within 1 or 2 standard deviations of the caliper measurement. The only exception was the 90 μm paper. Method 1 and Method 2 were not in agreement in most cases, which is probably due to the presence of air between

Paper thickness [μm]				
Reference	**68**	**72**	**83**	**90**
Caliper	69.3 ± 1.8	72.5 ± 1.1	85.2 ± 1.2	93.8 ± 1.0
OCT Method 1	69.6 ± 3.2	77.4 ± 2.8	117.3 ± 3.3	105.7 ± 4.3
OCT Method 2	52.4 ± 5.6	70.5 ± 3.7	80.0 ± 7.4	97.9 ± 6.1
Reference	**164**	**256**	**443**	
Caliper	164.2 ± 2.7	255.5 ± 5.5	416 ± 14.7	
OCT Method 3	179-208	361-376	403-427	

Table 5.2: The measured thickness of the paper samples. Papers with a reference thickness up 90 μm were investigated with both Method 1 and Method 2, whereas the thicker papers were only investigated with Method 3. Reported uncertainties for the caliper measurements is the standard deviation of six measurements.

paper and mirror. For the two thinnest papers Method 1 outperformed Method 2, and vice versa for 83 μm and 90 μm papers. Method 1 had a lower uncertainty in all cases, showing that it was less sensitive to outliers. The biggest discrepancy between the caliper and OCT measurements was the thickness of the 256 μm paper, which OCT estimated to be more than 100 μm too big. In contrast, Method 3 performed quite well for the 164 μm and 443 μm papers. The most probable explanation for this discrepancy is that the paper was not in proper contact with the surface below.

5.3.3 Surface roughness and defect detection

Surface roughness makes it harder to measure paper thickness using an optical system. Especially, if the roughness is on a length scale that is longer than the spot size of the optical system. However, OCT has the advantage that it images the surface simultaneously with the thickness determination, such that the roughness of the surface can be evaluated. The difference in surface roughness is evident between the three samples in Figure 5.7, where the 443 μm paper is most rough, and the 256 μm paper has a very smooth surface with a separate layer at the top, and a darker region below. This layer adds a high gloss finish to the paper. The layer has an optical thickness of $30 - 40$ μm, which is consistent with the thickness of the coating on high gloss photo paper reported in [116]. Assuming a refractive index of high-gloss alkyd enamel of 1.7 [86], this corresponds to a thickness of $18 - 24$ μm.

The ability of OCT to detect defects in the paper structure is shown in Figure 5.8. In **a)** and **c)** the 108 μm paper is shown. In the B-scan a void in the paper structure is apparent. The void results in improved penetration of the light such that the mirror is resolved below. A few more voids are also visible in the en-face image. In **b)** and **d)** a cut in the 108 μm paper is shown. The cut reveals the mirror beneath the paper. The en-face image shows the length of the cut, and that part of the cut is only a scratch in the surface of the paper.

To test the appearance of an oil drop on a paper sample a small droplet of sunflower oil was placed on the 68 μm paper. In Figure 5.9 **a)** and **b)** B-scans of the oil droplet on the paper is shown. The oil droplet appears as a curve with a very sharp top surface

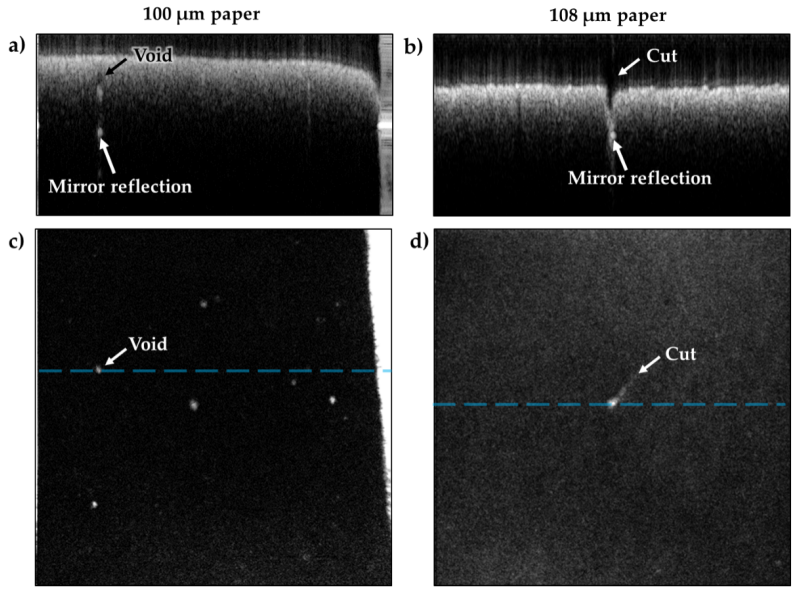

Figure 5.8: OCT images of paper defects and a cut in the paper. **a)** shows a B-scan, where there is a void in the 100 μm paper. **c)** shows the corresponding en-face image, from a full volume scan. The dashed line shows the position of the B-scan in **a)**. In **b)** and **d)** a B-scan and an en-face image is also shown, in this case of a cut in the 108 μm paper.

on top of the paper. As the oil is dissolved into the paper matrix, small air holes are filled out, and as the oil has a refractive index much closer to the cellulose than air does, this results in better light penetration. Therefore, the soaked area of the paper can be seen from the extent that the mirror is visible below the paper. This region has been marked as ”soaked paper” in **a)**. In **b)** the better penetration of the light reveals air gaps between the paper and the mirror as a dark region below the scattering signal seen from the paper.

An en-face image of the paper surface is shown in **c)**. The oil droplet is apparent as a high gloss surface. Next to the oil droplet is a region of soaked paper which appears slightly darker than the dry paper surrounding it. In **d)** an en-face image below the top surface of the paper is shown. Here, the improved penetration results in a brighter signal in the soaked paper than in the dry paper. The improved penetration from applying a clearing agent was also used in [117], where benzyl-alcohol added to a 102 μm paper sample allowed full penetration with 830 nm light from an SLD.

5.3.4 Discussion

In this work it was shown that 4 μm OCT allowed much better penetration in paper samples than had previously been reported for near-IR systems [116, 117]. This suggests that even better penetration could be achieved by taking advantage of even longer

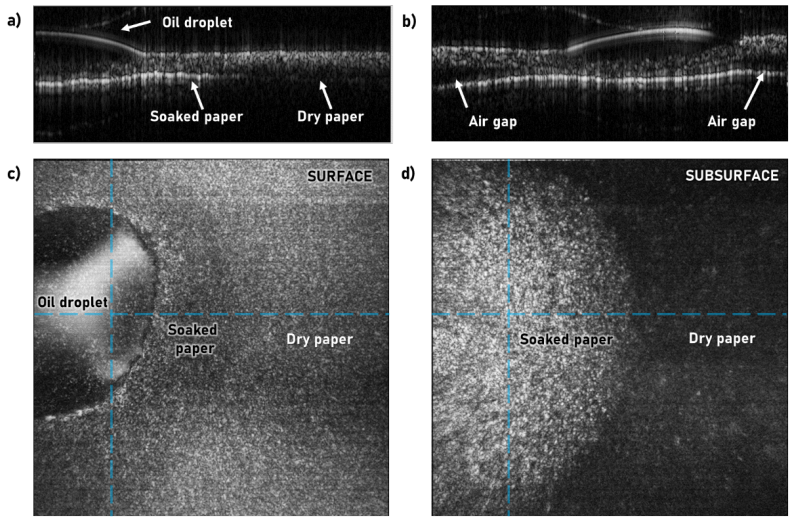

Figure 5.9: OCT images of an oil droplet on a paper sample. **a)** and **b)** orthogonal B-scans of the oil droplet. **c)** en-face image of the surface of the paper, and **d)** en-face image below the paper surface. The dashed lines in **c)** and **d)** show the positions of the B-scans in **a)** and **b)**.

wavelength SC sources, that have been achieved past 10 μm [15, 59]. Unfortunately, this would lead to reduced resolution, due to the longer centre wavelength.

It was shown that OCT can be used to estimate the refractive index of a paper sample, which can potentially be used to distinguish papers with different constituents and densities. However, the broad bandwidth that is necessary for good axial resolution means that it cannot be assumed that the refractive index is constant. As such, OCT will only be able to estimate an average of the refractive index. The full spectral dependence on the wavelength could probably be estimated by doing spectroscopic OCT, which is in fact the topic of the next chapter - although not on the application on paper samples.

CHAPTER 6

Spectroscopic Optical Coherence Tomography

In spectroscopic optical coherence tomography (S-OCT), the broad bandwidth of the laser source is used to gather spectrally dependent information about the sample. The earliest use of the term spectroscopic optical coherence tomography, I have found, is in a conference paper from 1996 [118]. Across the spectral range $1270 - 1340$ nm they spectrally resolved the scattering coefficient of polystyrene micro spheres suspended in collagen gel. In 2000, an OCT system based on a 350 nm bandwidth $Ti : Al_2O_3$ laser allowed spectrally differentiating melanocytes in OCT taken in-vivo of African frog tadpoles [119]. Spectroscopic contrast was obtained by subdividing the spectrum using a Morlet wavelet transform. A similar approach based on a windowed Fourier Transform of visible light OCT interferograms allowed true colour S-OCT images in-vivo of a dorsal skinfold window chamber model in a mouse [120]. The illuminating light source was an SC laser source. Similarly to conventional OCT, much of the progress in S-OCT has been driven by its application in biomedical imaging [121]. Of specific interest in S-OCT is the tracking of hemoglobin oxygen saturation [120, 122].

As discussed in Chapter 5, the mid-IR spectral range is not suitable for most biomedical imaging applications. However, it has potential in many of the applications, that mid-IR SC sources are already applied for, such as trace gas detection and spectroscopy [11, 58]. As touched upon in section 4.2, there is a significant CO_2 absorption band centred at 4.28 μm (This number is the centre-of-mass of the absorption curve provided by the HITRAN database [123]). This motivates that depth-resolved imaging of the presence of CO_2 can be achieved, which is the topic of the next section.

6.1 CO_2 Flow Measurements with Spectroscopic OCT

Storage of CO_2 through mineralisation in the underground is a promising approach to mitigate climate change [124, 125]. In fact, mineral storage of CO_2 in only the ocean ridges that Iceland is a part of, which consists mostly of basalt, has the potential to store the CO_2 that would be emitted from burning all of the fossil fuel carbon on earth [126]. Therefore, we decided to pursue imaging of CO_2 flow in porous rock as we believed that any contribution to this research would be of utmost importance.

The first goal is to show proof-of-concept depth-resolved imaging of CO_2 flow, which will be the purpose of this section. This will also be the last section before a general

conclusion to the thesis is given in the next chapter. Hopefully, my colleagues will continue the endeavour in CO_2 flow imaging after I have left. In [VI] we have shown sensitivity to the presence of CO_2 between the imaging lens and a mirror on an A-scan level. Since then, the approach has been to go for a more controlled environment, where flow of pure CO_2 could be imaged real time on a B-scan level. This environment is shown in Figure 6.1.

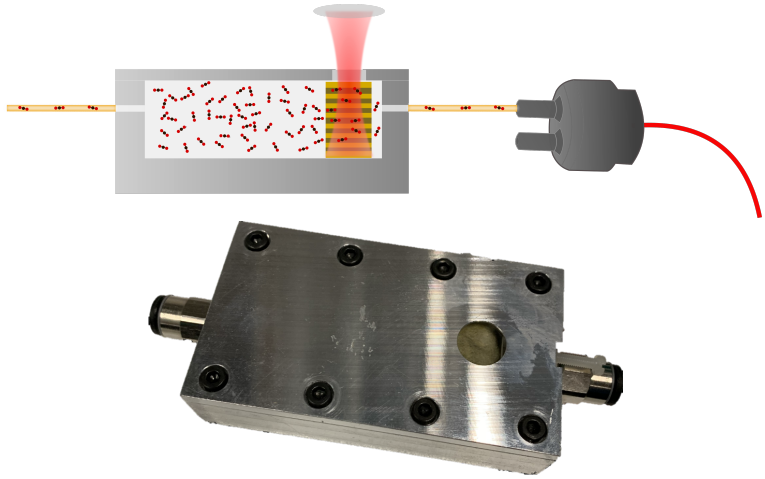

Figure 6.1: Top) A sketch of the setup used in imaging of CO_2 flow. **Below)** Photograph of the gas cell, with rockwool inside.

A gas cell is connected to a canister of CO_2 on one side, and a CO_2 sensor (SprintIR®-W CO2 Sensor, Gas Sensing Solutions) on the other, both with push-tubes. The gas sensor is able to measure between 0 % and 100 % CO_2 concentration in normal atmospheric conditions. As the gas cell was tested up to approximately 5 bar pressure, the CO_2 sensor was saturated in many measurements. Pressure above 1 bar was achieved by closing of the setup with a needle valve after the CO_2 sensor. As the CO_2 sensor and the sample are not in the exact same position, there can be a discrepancy between the timing of the concentration in the gas cell and the sensor. The 3 mm thick CaF_2 window allows imaging into the gas cell. An identical window was placed in the reference arm to avoid unbalanced dispersion.

A large set of samples has been investigated as candidates for proof-of-concept imaging of CO_2 flow. An ideal sample holds several properties:

- Transparent in the spectral range of our OCT system. Without this property presence of CO_2 can only be detected *above* the sample, not *within*.
- The sample should be porous, such that CO_2 can flow through it.
- Ideally, the sample has a smooth surface. A rough surface leads to a significant loss in signal for layers below. Samples with a rougher surface could be investigated, if the setup had a higher sensitivity.

- A mechanically stable sample is preferable, as the air flow would otherwise mean that the sample shifts around.

An obvious sample to investigate is basalt rock, which has kindly been provided by Professor Susan Stipp from DTU Physics. The basalt rock is shown in Figure 6.2. Each

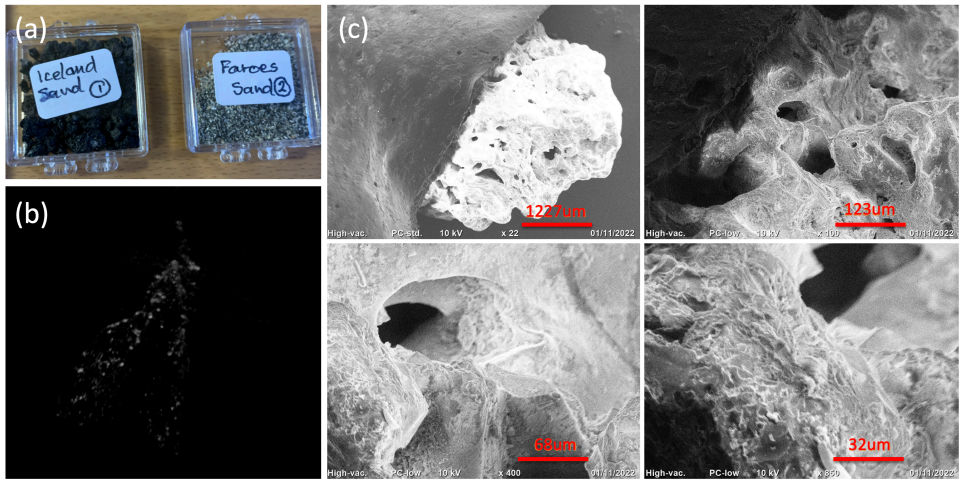

Figure 6.2: **(a)** photograph of basalt stone from Iceland (left) and sand from the Faroe Islands (right), kindly provided by Professor Susan Stipp. **(b)** OCT volume scan of a rock from the basalt sample. **(c)** SEM images of the basalt sample at four different levels of magnification.

rock in the sample is a few millimetres in each dimension. In **(b)** an OCT C-scan of the tip of a piece of basalt rock is shown. The outer contours of the rock can be seen, and in the cases where a surface results in a perfect back-reflection, a strong signal can be seen. Unfortunately, no significant signal came from the inside of the rock. This could potentially be remedied by first polishing the rock to obtain a smoother surface. SEM images taken at Nanoteket at DTU Physics are shown in **(c)**. The four images show 4 different magnification levels. The basalt rock has a porous structure, where some pores are more than 100 μm in length and height. At such a length scale, the pores should be resolvable in our mid-IR OCT system.

The need for a high amount of porosity, gave Asbjørn Moltke the idea that maybe we should go for the most porous material that we know of: Aerogel. Aerogel is a solid material consisting mostly of air. The specific sample we have is based on silica, and it is bought from Amazon, where it is claimed to consist of 99.8 % air [1]. The aerogel sample is shown in Figure 6.3. In **(a)** chunks of the aerogel is shown. For imaging, the aerogel was first crushed into a powder. In **(b)** an OCT B-scan of the crushed aerogel is shown on top of a mirror. In the left half of the image there is no aerogel,

[1] https://www.amazon.com/Aerogel-Particle-Laboratory-Sifity-Lightest/dp/B09LSJ34KQ/ref=sr_1_3?keywords=aerogel&qid=1676902573&sr=8-3

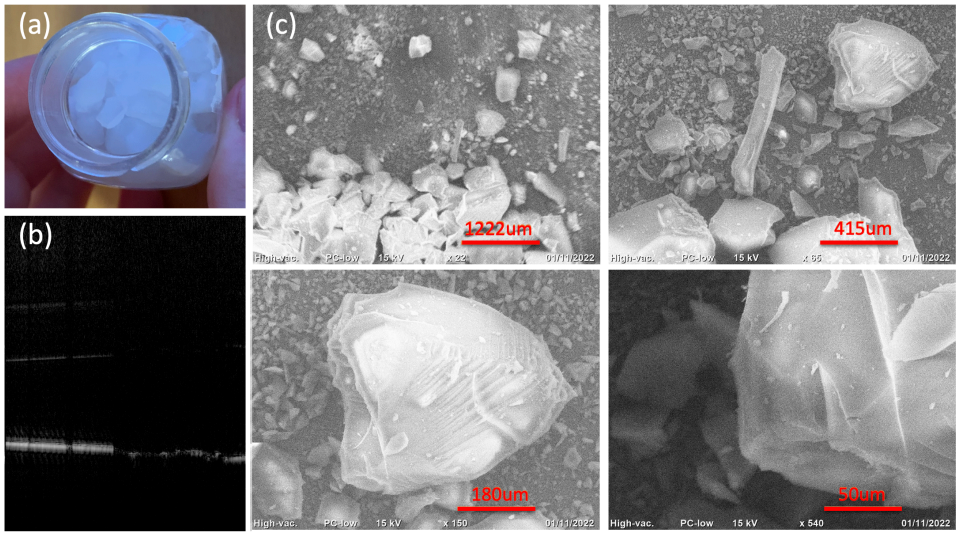

Figure 6.3: **(a)** photograph of chunks of aerogel. **(b)** OCT B-scan of crushed aerogel on a mirror. There is only aerogel on the mirror on in the right half of the image, in the left half the mirror was left bare. **(c)** SEM images of crushed aerogel at four different levels of magnification.

and in the right half there is. Interestingly, the extremely high porosity of the aerogel has rendered it completely invisible to the mid-IR OCT system. The only thing that shows that there is indeed a sample in the image, is that the mirror is attenuated and shifted slightly downwards. The fact that the aerogel consists almost purely of air, means that the refractive index is very close to 1, such that the optical path through the aerogel is only slightly longer than through air. The implications of having a solid sample, that is practically invisible to the imaging system are very interesting. One could consider using it as an invisible medium to host another sample. Unfortunately, its invisibility rendered it uninteresting in terms of CO_2 flow imaging. In **(c)** SEM images of crushed aerogel is shown. It does not appear porous in the same way that the basalt sample did. however, the sample holder can be seen through the aerogel in some places, which shows it is also partially transparent for electrons.

Other potential samples we have investigated are:

- Packaging foam, which moves with the air flow, and has a quite rough surface, but can otherwise be penetrated nicely by the light.
- Dried up PU foam, which did not allow air flow through it. [2]
- Rockwool, which cannot be penetrated.

[2]Bought at Harald Nyborg - https://www.harald-nyborg.dk/droppen-pu-skum-500-ml

- Sand from Faroe islands, also shown in Figure 6.2 **(a)** which has a rough surface but can otherwise be penetrated nicely. This sand was about 80 million years old, which means it was no longer viable to store CO_2 through mineralisation.

The sample that proved most useful to show proof-of-concept imaging of CO_2 flow was 3D printed epoxy resin cubes with air channels running through. The designs were made in collaboration with Coraline Lapre, and the prints were performed by DTU Skylab. Several designs were tested for the geometry of the cube. The limiting factors

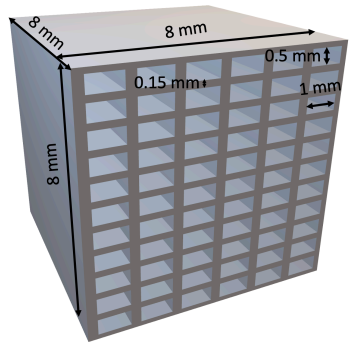

Figure 6.4: 3D drawing of a cube with channels running through it. Drawn in SOLIDWORKS prior to 3D print.

of the print were whether the printer was able to flush out the channels all the way through, and rounding of all corners due to printing resolution. A sketch of the final epoxy resin cube is shown in Figure 6.4. Rectangular channels were chosen to have longer flat surfaces in the transverse direction, while still minimising the amount of air, that the light has to travel through.

The CO_2 flow data set, that will be illustrated now consists of 300 B-scans taken in the same positions, such that the same place is imaged but temporally resolved. Such a data structure is sometimes referred to as an M-scan. Each B-scan consists of 300 A-scans, and an integration time of 900 μs was applied. The data processing is identical to that of conventional OCT up to the point of the Fourier Transform. At this point the interferograms, $\mathrm{Int}(k)$, are multiplied by Gaussian windows, such that the signal can be resolved spectrally.

$$\mathrm{Int}(k, k_0, \Delta k) = \mathrm{Int}(k) \exp\left(-\frac{(k-k_0)^2}{\Delta k^2}\right) \tag{6.1}$$

The spectral windows are shown in Figure 6.5, along with the reference arm spectrum and the CO_2 absorption curve. Two spectral windows are applied additionally to the CO_2 window - one on each side. The centre of the CO_2 sensitive window is set to the centre of mass of the CO_2 absorption curve. The width of the CO_2 window and the distance to the two neighbouring windows have been chosen through manual optimisation of the CO_2 sensitive contrast that will be described shortly. The widths

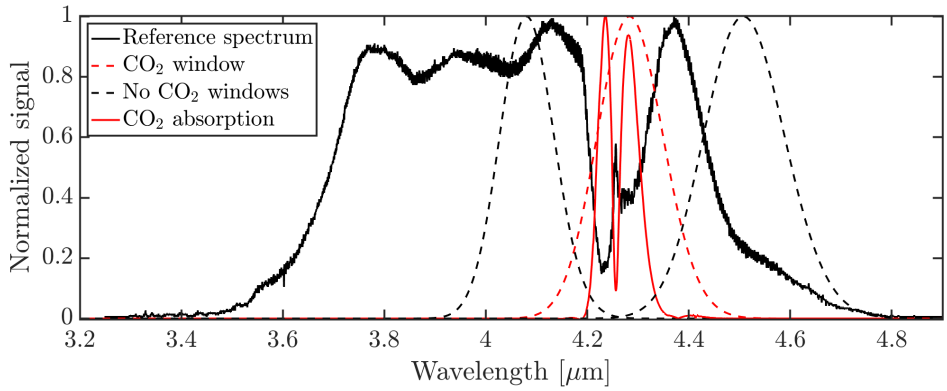

Figure 6.5: Windows used in spectroscopic post processing of data plotted on top of the reference arm spectrum, and the CO_2 absorption curve from the HITRAN database. The window in the CO_2 absorption band is shown in dashed red, while the black windows on either side are not sensitive to CO_2 presence.

of the two windows outside the CO_2 absorption band have been chosen such that the resolution is the same in all three windows by keeping the quantity $\lambda_c^2/\Delta\lambda$ constant. The three windows have centre wavelengths and FWHM given by $\lambda_c = 4.080$ μm $\Delta\lambda = 0.125$ μm, $\lambda_c = 4.283$ μm $\Delta\lambda = 0.153$ μm, and $\lambda_c = 4.507$ μm $\Delta\lambda = 0.188$ μm.

Additionally to the three windowed Fourier transforms, A-scans from the full interferograms, A-$\text{scan}_{\text{Full}}$, are also calculated. The analysis is similar to the one described in [127], where they showed sensitivity to the contrast agent indocyananine in in-vivo imaging of a mouse eye. To obtain the spectral sensitivity, a post processing approach was applied, where the OCT spectrum was split in 3 windows, and the relative intensity in the images between spectral bands allowed temporally and spatially resolving the presence of the contrast agent.

The multiplication of windows to the interference signal has a couple of negative implications:

- The axial resolution is lowered due to the much more narrow bandwidth. In the following figures this has been partially remedied by multiplying the windowed Fourier transforms by A-$\text{scan}_{\text{Full}}$, such that the spectroscopic signal is obtained by the windowed Fourier transform, and the resolution is set by the full spectrum. This approach is conceptually similar to the ”dual-window” approach that was applied in [120].
- The windows introduce a decline in sensitivity, due to the previously discussed sensitivity advantage one gets from using a spectrometer [92]. The sensitivity gain scales with the number of diodes in the spectrometer, so when the windows introduce an effective reduction in the number of diodes, the sensitivity is diminished.

Defining the A-scans obtained from the CO_2 window as A-scan$_{CO_2}$, and the average of the two other windows as A-scan$_{Rest}$, the spectroscopic contrast is defined as

$$\text{A-scan}_{\text{Contrast}} = \frac{|\text{A-scan}_{CO_2} - \text{A-scan}_{\text{Rest}}|}{\text{A-scan}_{CO_2}} \tag{6.2}$$

Due to the risk of dividing by a very small number, a minimum threshold on A-scan$_{\text{Contrast}}$ is applied, such that the contrast is set to zero, for any pixel in which A-scan$_{\text{Full}} < 0.05 \cdot \max(\text{A-scan}_{\text{Full}})$.

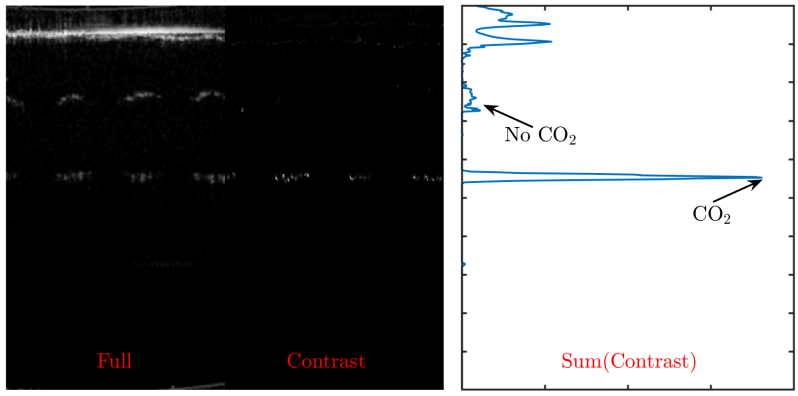

Figure 6.6: The left image shows the OCT image using the full bandwidth next to the contrast calculated according to equation 6.2. The graph on the right shows the sum at each depth of the contrast image.

One frame from the time resolved B-scans of the epoxy resin cube is shown in the left most image, marked by "Full", in Figure 6.6. The top interface in the image is the bottom of the CaF_2 window, and the top of the epoxy resin cube. The top of the epoxy resin cube is pressed up against the window to minimise the amount of CO_2 above the sample. The maximum value in each A-scan comes from the bottom of the window, which means that each A-scan could be shifted pixel-by-pixel such that this surface appears flat rather than curved. The next interface is the top of the first layer of channels, and the interface below is the bottom of the air hole. The lateral scan range resulted in imaging of almost 4 channels. Each channel has a height of approximately 450 μm, according to the OCT images, which is a difference of 10 % compared to the design. The shape of the CO_2 absorption curve is multiplied to the interferograms. After a Fourier transform of the obtained interferograms this results in the appearance of extra lines around each interface below the OCT gas. This is due to the CO_2 absorption curve appearing as a low frequency signal multiplied on the higher frequency, which appears as a slight shift in OPD.

The image marked by "Contrast" shows the contrast as calculated with equation 6.2. In this frame the gas cell was filled with CO_2, which can be seen by contrast appearing at the same positions as the bottom of each channel. In the graph shown

on the right, a sum of the contrast at each depth is shown. This shows that contrast appears in the images, even where there is no presence of CO_2. The contrast measure, as defined in equation 6.2, will also be sensitive to other effects such as slightly different axial resolution in the three windows, any amount of unbalanced dispersion, and the dispersion of the sample. These effects are amplified by the strong signal from the window and the top of the cube. Therefore, the best measure for the strength of the CO_2 contrast is given by the relative contrast by two interfaces which are alike and only separated by air - the top and the bottom of the channel. These two signals are marked by "No CO_2" for the top of the channels, and "CO_2" for the bottom.

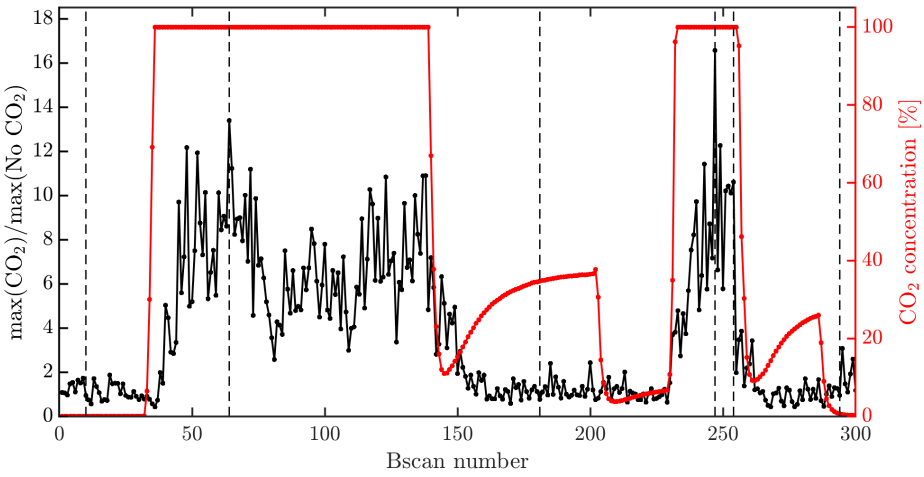

Figure 6.7: The ratio of the signal from the bottom interface to the top interface of the channels in the 3D printed cube, as a function of the B-scan number. The right y-axis shows the corresponding CO_2 concentration measured on the CO_2 sensor. The vertical dashed lines indicate the positions of B-scans that are shown in Figure 6.8.

The relative strength of these signals, as a function of the B-scan number, is plotted (in black) in Figure 6.7. The CO_2 concentration measured with the CO_2 sensor is plotted on the right y-axis. The dynamic range of the sensor only goes to pure CO_2 in atmospheric conditions. Therefore, the sensor is saturated in all cases where the pressure in the gas cell is above atmospheric. In the current setup we have no way of controlling the pressure accurately. Between B-scan 150 and B-scan 200, the CO_2 sensor measured a slowly varying concentration, which was achieved by quickly flushing with nitrogen, and then letting the residual CO_2 in the setup flow back. However, as the sensor and the sample are not in the same position, the sensor does not give a reliable measure of the CO_2 presence. The relative strength does not indicate, that there was any CO_2 in the channels in these B-scans.

The highest relative strength is above 16, and the trend in the relative strength is generally in good agreement with the CO_2 sensor. In Figure 6.8, the contrast has been mapped to a red-scale which is plotted on top of the OCT intensity. The red-scale is only visible on the bottom channels. The OCT intensity is calculated with the full

bandwidth of the system. Six different B-scans are chosen, according to the vertical dashed lines in Figure 6.7. CO_2 has flown into the channels between B-scan 10 and B-scan 64. The remaining B-scans show the CO_2 having been flushed out with nitrogen gas, pumped back in, and flushed back out again. The B-scans generally show the same tendencies as Figure 6.7.

Thus, it has been shown as a proof-of-concept that the current setup is indeed able to resolve the presence of CO_2 gas, both temporally and spatially. An improvement on several parameters would show a more impressive proof of concept:

- A better way of controlling the concentration would allow a proper determination of the sensitivity of the system.
- A sample, where more layers could be resolved in depth would highlight the ability to do depth resolved imaging in much more clear way. This would result in the contrast being approximately equal between the bottom of one channel and the top of the channel below, such that the CO_2 signal should always be calculated relative to the channel above.

  We have almost exhausted the resolution of the epoxy resin 3D printer, that we had available. However, alternative manufacturing techniques such as ceramic 3D printing is interesting for a better proof-of-concept sample [3]
- Of course, higher sensitivity would also be highly desirable.

This concludes the chapter on S-OCT. In the next, and final, chapter the thesis will be concluded.

[3]See e.g. the company Lithoz: https://lithoz.com/en/

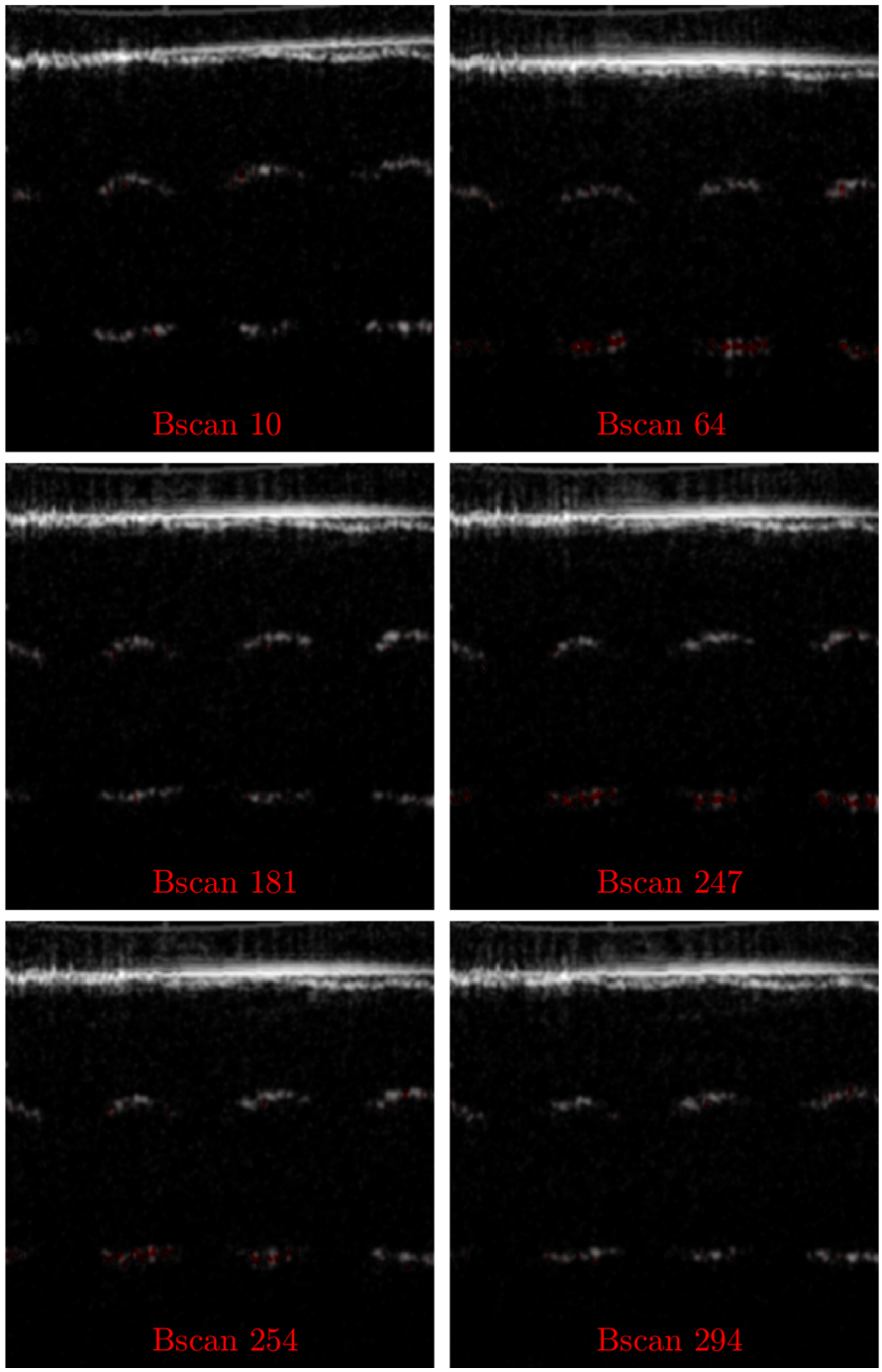

Figure 6.8: Selected B-scans from the temporally resolved scan. The grey-scale shows the intensity. The CO_2 signal is mapped to a red-scale on top of the intensity.

CHAPTER 7

Conclusion and Outlook

This thesis, as the culmination to my PhD project, has provided a review of doing exactly what the title says: "Mid-Infrared Supercontinuum based Spectroscopic OCT". An SC laser source has been described as the light source for our mid-IR OCT setup. However, the applications of SC sources are not limited to OCT. Two key parameters for SC sources are the spectral range and the noise performance. In cascaded SC generation, which is a widely used approach to mid-IR SC generation, promising progress has been shown for both of these parameters:
Using numerical simulations, a collective redshift, due to Raman interaction between dispersed pulse tails, has been discovered in the normal dispersion regime. It has been identified as an important effect to shift light further into the mid-IR in highly nonlinear chalcogenide fibres, that act as the last stages in cascaded SC generation. Furthermore, it was shown that the resulting spectrum is tunable by manipulating the dispersion, which can be achieved by choosing different fiber parameters. Thereby, the SC spectrum can be designed with a specific application in mind.
Also in cascaded SC generation, it was shown, both in experiment and numerical simulations how the noise can be lowered significantly when solitons are coupled into a highly nonlinear chalcogenide fiber within the normal dispersion regime. Specifically, a reduction in RIN from above 35 % to below 25 % across a broad bandwidth from 2.7 μm to 3.5 μm. In fact, the noise was reduced all the way to the IR edge of the spectrum. Numerical simulations revealed that the noise reduction happens extremely rapidly, such that few centimetres of fibre - or the shortest length that practically can be handled - is sufficient. It is my hope that knowledge of these effects will help generate SC with even broader bandwidth, higher power, and lower noise in the mid-IR.

The mid-IR OCT system operates with a centre wavelength of 4 μm, and a bandwidth of almost 1 μm. Up-conversion to near-IR using sum-frequency generation allows detection of the mid-IR light using mature near-IR technology. Due to updates of our mid-IR OCT system, a thorough characterisation has been provided, showing an axial resolution of 11.9 μm, and a sensitivity of 60 dB at an integration time of 300 μs. As an example of the applicability of OCT within non-destructive testing, paper thickness and quality monitoring was shown. OCT can provide simultaneous measurements of thickness, surface roughness, and defects such as cuts, voids, and dirt (in the form of a droplet of oil). All of this is achieved without any contact between the OCT probe and the paper. Mid-IR OCT has already shown great potential in materials characterisation with a resolution of few microns. With the rapid development of better mid-IR SC sources, and more efficient detection of the mid-IR light, mid-IR OCT will only show even better applicability in the future.

Finally, a proof of concept of depth resolved sensing of CO_2 was given. Sensitivity

to the presence of CO_2 in channels inside a 3D printed epoxy resin sample was clearly illustrated. Further improvement of both the OCT system as well as the spectroscopic post-processing has the potential to enable imaging inside more interesting samples such as the porous rocks that are used to store CO_2 through mineralisation at the Hellisheidi geothermal power plant in Iceland.

Bibliography

[1] J. P. Gardner, J. C. Mather, M. Clampin, R. Doyon, M. A. Greenhouse, H. B. Hammel, J. B. Hutchings, P. Jakobsen, S. J. Lilly, K. S. Long, et al., "The james webb space telescope," Space Science Reviews **123**, 485 (2006).

[2] G. H. Rieke, G. S. Wright, T. Böker, J. Bouwman, L. Colina, A. Glasse, K. D. Gordon, T. P. Greene, M. Güdel, T. Henning, K. Justtanont, P.-O. Lagage, M. E. Meixner, H.-U. Nørgaard-Nielsen, T. P. Ray, M. E. Ressler, E. F. van Dishoeck, and C. Waelkens, "The mid-infrared instrument for the james webb space telescope, i: introduction," Publications of the Astronomical Society of the Pacific **127**, 584 (2015).

[3] D. Huang, E. A. Swanson, C. P. Lin, J. S. Schuman, W. G. Stinson, W. Chang, M. R. Hee, T. Flotte, K. Gregory, C. A. Puliafito, and J. G. Fujimoto, "Optical coherence tomography," Science **254**, 1178 (1991).

[4] W. Drexler and J. G. Fujimoto, *Optical coherence tomography technology and applications*, 2nd edition (Springer International Publishing, 2015).

[5] B. Povazay, K. Bizheva, A. Unterhuber, B. Hermann, H. Sattmann, A. F. Fercher, W. Drexler, A. Apolonski, W. J. Wadsworth, J. C. Knight, P. St. J. Russell, M. Vetterlein, and E. Scherzer, "Submicrometer axial resolution optical coherence tomography," Opt. Lett. **27**, 1800 (2002).

[6] P. Wachulak, A. Bartnik, and H. Fiedorowicz, "Optical coherence tomography (oct) with 2 nm axial resolution using a compact laser plasma soft x-ray source," Scientific Reports **8**, 10.1038/s41598-018-26909-0 (2018).

[7] S. Grelet, A. M. Jiménez, R. D. Engelsholm, P. B. Montague, and A. Podoleanu, "40 mhz swept-source optical coherence tomography at 1060 nm using a time-stretch and supercontinuum spectral broadening dynamics," IEEE Photonics Journal **14**, 1 (2022).

[8] B. P. Abbott et al. (LIGO Scientific Collaboration and Virgo Collaboration), "Observation of gravitational waves from a binary black hole merger," Phys. Rev. Lett. **116**, 061102 (2016).

[9] I. Hartl, X. D. Li, C. Chudoba, R. K. Ghanta, T. H. Ko, J. G. Fujimoto, J. K. Ranka, and R. S. Windeler, "Ultrahigh-resolution optical coherence tomography using continuum generation in an air–silica microstructure optical fiber," Opt. Lett. **26**, 608 (2001).

[10] N. M. Israelsen, C. R. Petersen, A. Barh, D. Jain, M. Jensen, G. Hannesschläger, P. Tidemand-Lichtenberg, C. Pedersen, A. Podoleanu, and O. Bang, "Real-time high-resolution mid-infrared optical coherence tomography," Light: Science & Applications **8**, 1 (2019).

[11] M. A. Abbas, K. E. Jahromi, M. Nematollahi, R. Krebbers, N. Liu, G. Woyessa, O. Bang, L. Huot, F. J. M. Harren, and A. Khodabakhsh, "Fourier transform spectrometer based on high-repetition-rate mid-infrared supercontinuum sources for trace gas detection," Opt. Express **29**, 22315 (2021).

[12] K. Shi, P. Li, S. Yin, and Z. Liu, "Chromatic confocal microscopy using supercontinuum light," Opt. Express **12**, 2096 (2004).

[13] H. Tu, Y. Liu, D. Turchinovich, M. Marjanovic, J. K. Lyngsø, J. Laegsgaard, E. J. Chaney, Y. Zhao, S. You, W. L. Wilson, B. Xu, M. Dantus, and S. Boppart, "Stain-free histopathology by programmable supercontinuum pulses," Nature Photonics **10**, 10.1038/nphoton.2016.94 (2016).

[14] S. G. Leon-Saval, T. A. Birks, W. J. Wadsworth, P. St.J. Russell, and M. W. Mason, "Supercontinuum generation in submicron fibre waveguides," Opt. Express **12**, 2864 (2004).

[15] C. R. Petersen, U. Møller, I. Kubat, B. Zhou, S. Dupont, J. Ramsay, T. Benson, S. Sujecki, N. Abdel-Moneim, Z. Tang, D. Furniss, A. Seddon, and O. Bang, "Mid-infrared supercontinuum covering the 1.4–13.3 μm molecular fingerprint region using ultra-high na chalcogenide step-index fibre," Nature Photonics **8**, 830 (2014).

[16] G. Agrawal, *Nonlinear fiber optics*, 5th edition, Electronics & Electrical (Elsevier Science, 2012).

[17] R. D. Engelsholm, "Low noise supercontinuum lasers for optical coherence tomography systems," PhD thesis (Technical University of Denmark, 2018).

[18] R. E. Hansen, *Cascaded mid-infrared supercontinuum lasers*, DTU Department of Electrical and Photonics Engineering, Master Thesis, 2020.

[19] R. D. Engelsholm and O. Bang, "Supercontinuum noise reduction by fiber undertapering," Opt. Express **27**, 10320 (2019).

[20] M. Frigo and S. Johnson, "The design and implementation of fftw3," Proceedings of the IEEE **93**, 216 (2005).

[21] J. Hult, "A fourth-order runge–kutta in the interaction picture method for simulating supercontinuum generation in optical fibers," J. Lightwave Technol. **25**, 3770 (2007).

[22] A. M. Heidt, A. Hartung, G. W. Bosman, P. Krok, E. G. Rohwer, H. Schwoerer, and H. Bartelt, "Coherent octave spanning near-infrared and visible supercontinuum generation in all-normal dispersion photonic crystal fibers," Opt. Express **19**, 3775 (2011).

[23] B. Saleh and M. Teich, *Fundamentals of photonics, 2nd edition* (June 2007).

[24] I. H. Malitson, "Interspecimen comparison of the refractive index of fused silica∗,†," J. Opt. Soc. Am. **55**, 1205 (1965).

[25] Knight, J.C., J. Arriaga, Birks, T.A., A. Ortigosa-Blanch, W. Wadsworth, and Russell, P.St.J., "Anomalous dispersion in photonic crystal fiber," Photonics Technology Letters, IEEE **12**, 807 (2000).

[26] P. Hlubina, M. Kadulová, and D. Ciprian, "Spectral interferometry-based chromatic dispersion measurement of fibre including the zero-dispersion wavelength," Journal of the European Optical Society - Rapid Publications vol 7 12017, 5 pages **7**, 2017 (2012).

[27] P. M. Moselund, "Long-pulse supercontinuum light sources," PhD thesis (Technical University of Denmark, 2009).

[28] J. Lægsgaard, "Mode profile dispersion in the generalized nonlinear schrödinger equation," Opt. Express **15**, 16110 (2007).

[29] K. Rottwitt and J. H. Povlsen, "Analyzing the fundamental properties of raman amplification in optical fibers," Journal of Lightwave Technology **23**, 3597 (2005).

[30] J. M. Dudley, G. Genty, and S. Coen, "Supercontinuum generation in photonic crystal fiber," Rev. Mod. Phys. **78**, 1135 (2006).

[31] A. V. Gorbach and D. V. Skryabin, "Theory of radiation trapping by the accelerating solitons in optical fibers," Physical Review A **76** (2007).

[32] A. M. Heidt, J. S. Feehan, J. H. V. Price, and T. Feurer, "Limits of coherent supercontinuum generation in normal dispersion fibers," J. Opt. Soc. Am. B **34**, 764 (2017).

[33] F. M. Mitschke and L. F. Mollenauer, "Discovery of the soliton self-frequency shift," Opt. Lett. **11**, 659 (1986).

[34] J. Yi, W. Liu, S. Chen, V. Backman, N. Sheibani, C. M. Sorenson, A. A. Fawzi, R. A. Linsenmeier, and H. F. Zhang, "Visible light optical coherence tomography measures retinal oxygen metabolic response to systemic oxygenation," Light: Science & Applications **4**, e334 (2015).

[35] S. P. Chong, M. Bernucci, H. Radhakrishnan, and V. J. Srinivasan, "Structural and functional human retinal imaging with a fiber-based visible light oct ophthalmoscope," Biomed. Opt. Express **8**, 323 (2017).

[36] M. Maria, L. d'Hont, A. Anisimov, M. Stols-Witlox, and R. Groves, "Three-dimensional spectral measurements of paint samples using optical coherence tomography," in Optics for arts, architecture, and archaeology viii, Vol. 11784, edited by H. Liang and R. Groves (International Society for Optics and Photonics, 2021), 117840Q.

[37] F. G. Omenetto, A. J. Taylor, M. D. Moores, and D. H. Reitze, "Adaptive control of femtosecond pulse propagation in optical fibers," Opt. Lett. **26**, 938 (2001).

[38] M. Tianprateep, J. Tada, T. Yamazaki, and F. Kannari, "Spectral-shape-controllable supercontinuum generation in microstructured fibers using adaptive pulse shaping technique," Japanese Journal of Applied Physics **43**, 8059 (2004).

[39] J. Tada, T. Kono, A. Suda, H. Mizuno, A. Miyawaki, K. Midorikawa, and F. Kannari, "Adaptively controlled supercontinuum pulse from a microstructure fiber for two-photon excited fluorescence microscopy," Appl. Opt. **46**, 3023 (2007).

[40] C. R. Smith, A. I. Adamu, M. Michieletto, and O. Bang, "Spectral broadening of ultraviolet dispersive waves in gas-filled hollow-core fiber using pump pulse modulation," Opt. Lett. **45**, 6744 (2020).

[41] C. Amra, M. Zerrad, S. Liukaityte, and M. Lequime, "Instantaneous one-angle white-light scatterometer," Opt. Express **26**, 204 (2018).

[42] E. Genier, P. Bowen, T. Sylvestre, J. M. Dudley, P. Moselund, and O. Bang, "Amplitude noise and coherence degradation of femtosecond supercontinuum generation in all-normal-dispersion fibers," J. Opt. Soc. Am. B **36**, A161 (2019).

[43] H. G. Dantanarayana, N. Abdel-Moneim, Z. Tang, L. Sojka, S. Sujecki, D. Furniss, A. B. Seddon, I. Kubat, O. Bang, and T. M. Benson, "Refractive index dispersion of chalcogenide glasses for ultra-high numerical-aperture fiber for mid-infrared supercontinuum generation," Opt. Mater. Express **4**, 1444 (2014).

[44] B. Ung and M. Skorobogatiy, "Chalcogenide microporous fibers for linear and nonlinear applications in the mid-infrared," Opt. Express **18**, 8647 (2010).

[45] F. Chenard, O. Alvarez, and H. Moawad, "Mir chalcogenide fiber and devices," Progress in Biomedical Optics and Imaging - Proceedings of SPIE **9317**, 10.1117/12.2085056 (2015).

[46] C. Xia, Z. Xu, M. N. Islam, F. L. Terry, M. J. Freeman, A. Zakel, and J. Mauricio, "10.5 w time-averaged power mid-ir supercontinuum generation extending beyond 4 μm with direct pulse pattern modulation," IEEE Journal of Selected Topics in Quantum Electronics **15**, 422 (2009).

[47] J.-C. Gauthier, V. Fortin, J.-Y. Carrée, S. Poulain, M. Poulain, R. Vallée, and M. Bernier, "Mid-ir supercontinuum from 2.4 to 5.4 μm in a low-loss fluoroindate fiber," Opt. Lett. **41**, 1756 (2016).

[48] B. Eggleton, B. Luther-Davies, and K. Richardson, "Chalcogenide photonics," Nature Photonics **5** (2011).

[49] V. Artyushenko, A. Bocharnikov, T. Sakharova, and I. Usenov, "Mid-infrared fiber optics for 1 — 18 m range," Optik & Photonik **9**, 35 (2014).

[50] *As2s3 fiber data in webpage*, https://irflex.com/products/irf-s-series/, Accessed: 2022-30-12.

[51] *As2se3 fiber data in webpage*, https://irflex.com/products/irf-se-series/, Accessed: 2022-30-12.

[52] T. Cheng, K. Nagasaka, T. H. Tuan, X. Xue, M. Matsumoto, H. Tezuka, T. Suzuki, and Y. Ohishi, "Mid-infrared supercontinuum generation spanning 2.0 to 15.1 μm in a chalcogenide step-index fiber," Opt. Lett. **41**, 2117 (2016).

[53] A. Lemière, R. Bizot, F. Désévédavy, G. Gadret, J.-C. Jules, P. Mathey, C. Aquilina, P. Béjot, F. Billard, O. Faucher, B. Kibler, and F. Smektala, "1.7–18 µm mid-infrared supercontinuum generation in a dispersion-engineered step-index chalcogenide fiber," Results in Physics **26**, 104397 (2021).

[54] C. R. Petersen, P. M. Moselund, L. Huot, L. Hooper, and O. Bang, "Towards a table-top synchrotron based on supercontinuum generation," Infrared Physics & Technology **91**, 182 (2018).

[55] C. Xia, M. Kumar, O. P. Kulkarni, M. N. Islam, F. L. Terry, M. J. Freeman, M. Poulain, and G. Mazé, "Mid-infrared supercontinuum generation to 4.5 μm in zblan fluoride fibers by nanosecond diode pumping," Opt. Lett. **31**, 2553 (2006).

[56] R. R. Gattass, L. Brandon Shaw, V. Q. Nguyen, P. C. Pureza, I. D. Aggarwal, and J. S. Sanghera, "All-fiber chalcogenide-based mid-infrared supercontinuum source," Optical Fiber Technology **18**, Fiber Supercontinuum sources and their applications, 345 (2012).

[57] C. R. Petersen, P. M. Moselund, C. Petersen, U. Møller, and O. Bang, "Spectral-temporal composition matters when cascading supercontinua into the mid-infrared," Opt. Express **24**, 749 (2016).

[58] G. Woyessa, K. Kwarkye, M. K. Dasa, C. R. Petersen, R. Sidharthan, S. Chen, S. Yoo, and O. Bang, "Power stable 1.5–10.5 µm cascaded mid-infrared supercontinuum laser without thulium amplifier," Opt. Lett. **46**, 1129 (2021).

[59] R. A. Martinez, G. Plant, K. Guo, B. Janiszewski, M. J. Freeman, R. L. Maynard, M. N. Islam, F. L. Terry, O. Alvarez, F. Chenard, R. Bedford, R. Gibson, and A. I. Ifarraguerri, "Mid-infrared supercontinuum generation from 1.6 to >11 µm using concatenated step-index fluoride and chalcogenide fibers," Opt. Lett. **43**, 296 (2018).

[60] S. Rao D. S., M. Jensen, L. Grüner-Nielsen, J. Olsen, P. Heiduschka, B. Kemper, J. Schnekenburger, M. Glud, M. Mogensen, N. Israelsen, and O. Bang, "Shot-noise limited, supercontinuum based optical coherence tomography," **10**, 133 (2021).

[61] D. R. Solli, C. Ropers, and B. Jalali, "Active control of rogue waves for stimulated supercontinuum generation," Phys. Rev. Lett. **101**, 233902 (2008).

[62] K. Kwarkye, M. Jensen, R. D. Engelsholm, M. K. Dasa, D. Jain, P. Bowen, P. M. Moselund, C. R. Petersen, and O. Bang, "In-amplifier and cascaded mid-infrared supercontinuum sources with low noise through gain-induced soliton spectral alignment," Scientific Reports **10**, 10.1038/s41598-020-65150-6 (2020).

[63] J. M. Dudley, G. Genty, A. Mussot, A. Chabchoub, and F. Dias, "Rogue waves and analogies in optics and oceanography," Nature Reviews Physics **1**, 675 (2019).

[64] D. R. Solli, C. Ropers, P. Koonath, and B. Jalali, "Optical rogue waves," Nature **450**, 1054 (2007).

[65] M. N. Islam, G. Sucha, I. Bar-Joseph, M. Wegener, J. P. Gordon, and D. S. Chemla, "Femtosecond distributed soliton spectrum in fibers," J. Opt. Soc. Am. B **6**, 1149 (1989).

[66] M. Erkintalo, G. Genty, and J. M. Dudley, "Giant dispersive wave generation through soliton collision," Opt. Lett. **35**, 658 (2010).

[67] M. Erkintalo, G. Genty, and J. M. Dudley, "Experimental signatures of dispersive waves emitted during soliton collisions," Opt. Express **18**, 13379 (2010).

[68] Y. Fang, D. Jayasuriya, D. Furniss, Z. Q. Tang, L. Sojka, C. Markos, S. Sujecki, A. B. Seddon, and T. Benson, "Determining the refractive index dispersion and thickness of hot-pressed chalcogenide thin films from an improved swanepoel method," Optical and Quantum Electronics **49**, 10.1007/s11082-017-1057-9 (2017).

[69] C. Petersen, S. Dupont, C. Agger, J. Thøgersen, O. Bang, and S. R. Keiding, "Stimulated raman scattering in soft glass fluoride fibers," JOSA B **28**, 2310 (2011).

[70] S. Venck, F. St-Hilaire, L. Brilland, A. N. Ghosh, R. Chahal, C. Caillaud, M. Meneghetti, J. Troles, F. Joulain, S. Cozic, S. Poulain, G. Huss, M. Rochette, J. M. Dudley, and T. Sylvestre, "2–10 µm mid-infrared fiber-based supercontinuum laser source: experiment and simulation," Laser & Photonics Reviews **14**, 2000011 (2020).

[71] D. Anderson, M. Desaix, M. Lisak, and M. L. Quiroga–Teixeiro, "Wave breaking in nonlinear-optical fibers," J. Opt. Soc. Am. B **9**, 1358 (1992).

[72] J. M. Dudley, F. Dias, M. Erkintalo, and G. Genty, "Instabilities, breathers and rogue waves in optics," Nature Photonics **8**, 10.1038/nphoton.2014.220 (2014).

[73] J. M. Dudley, G. Genty, and B. J. Eggleton, "Harnessing and control of optical rogue waves in supercontinuum generation," Opt. Express **16**, 3644 (2008).

[74] S. T. Sørensen, O. Bang, B. Wetzel, and J. M. Dudley, "Describing supercontinuum noise and rogue wave statistics using higher-order moments," Optics Communications **285**, 2451 (2012).

[75] F. Gan, "Optical properties of fluoride glasses: a review," Journal of Non-Crystalline Solids **184**, Non-oxide Glasses, 9 (1995).

[76] C. Xiong, E. Magi, F. Luan, A. Tuniz, S. Dekker, J. S. Sanghera, L. B. Shaw, I. D. Aggarwal, and B. J. Eggleton, "Characterization of picosecond pulse nonlinear propagation in chalcogenide as2s3 fiber," Applied optics **48**, 5467 (2009).

[77] S. Chen, Y. Jung, S. Alam, D. J. Richardson, R. Sidharthan, D. Ho, S. Yoo, and J. M. O. Daniel, "Ultra-short wavelength operation of thulium-doped fiber amplifiers and lasers," Opt. Express **27**, 36699 (2019).

[78] C. R. Smith, R. D. Engelsholm, and O. Bang, "Pulse-to-pulse relative intensity noise measurements for ultrafast lasers," Opt. Express **30**, 8136 (2022).

[79] J. G. Fujimoto, M. E. Brezinski, G. J. Tearney, S. A. Boppart, B. Bouma, M. R. Hee, J. F. Southern, and E. A. Swanson, "Optical biopsy and imaging using optical coherence tomography," Nature medicine **1**, 970 (1995).

[80] A. F. Fercher, "In vivo optical coherence tomography in ophthalmology," in Medical optical tomography: functional imaging and monitoring, Vol. 10311, edited by G. J. Mueller (International Society for Optics and Photonics, 1993), page 103110L.

[81] E. A. Swanson, J. A. Izatt, M. R. Hee, D. Huang, C. P. Lin, J. S. Schuman, C. A. Puliafito, and J. G. Fujimoto, "In vivo retinal imaging by optical coherence tomography," Opt. Lett. **18**, 1864 (1993).

[82] N. M. Israelsen, M. Maria, M. Mogensen, S. Bojesen, M. Jensen, M. Haedersdal, A. Podoleanu, and O. Bang, "The value of ultrahigh resolution oct in dermatology - delineating the dermo-epidermal junction, capillaries in the dermal papillae and vellus hairs," Biomed. Opt. Express **9**, 2240 (2018).

[83] M. E. Brezinski, G. J. Tearney, B. E. Bouma, J. A. Izatt, M. R. Hee, E. A. Swanson, J. F. Southern, and J. G. Fujimoto, "Optical coherence tomography for optical biopsy," Circulation **93**, 1206 (1996).

[84] F. Wiesner, M. Wünsche, J. Reinhard, J. J. Abel, J. Nathanael, S. Skruszewicz, C. Rödel, S. Yulin, A. Gawlik, G. Schmidl, U. Hübner, J. Plentz, G. G. Paulus, and S. Fuchs, "Material-specific imaging of nanolayers using extreme ultraviolet coherence tomography," Optica **8**, 230 (2021).

[85] P. Targowski, M. Iwanicka, M. Sylwestrzak, C. Frosinini, J. Striova, and R. Fontana, "Using optical coherence tomography to reveal the hidden history of the landsdowne virgin of the yarnwinder by leonardo da vinci and studio," Angewandte Chemie International Edition **57**, 7396 (2018).

[86] C. R. Petersen, N. Rajagopalan, C. Markos, N. M. Israelsen, P. J. Rodrigo, G. Woyessa, P. Tidemand-Lichtenberg, C. Pedersen, C. E. Weinell, S. Kiil, and O. Bang, "Non-destructive subsurface inspection of marine and protective coatings using near- and mid-infrared optical coherence tomography," Coatings **11**, 10.3390/coatings11080877 (2021).

[87] S. Ishida and N. Nishizawa, "Quantitative comparison of contrast and imaging depth of ultrahigh-resolution optical coherence tomography images in 800–1700 nm wavelength region," Biomed. Opt. Express **3**, 282 (2012).

[88] Z. Ding, H. Ren, Y. Zhao, J. S. Nelson, and Z. Chen, "High-resolution optical coherence tomography over a large depth range with an axicon lens," Opt. Lett. **27**, 243 (2002).

[89] J. Holmes, S. Hattersley, N. Stone, F. Bazant-Hegemark, and H. Barr, "Multichannel fourier domain oct system with superior lateral resolution for biomedical applications - art. no. 68470o," Proceedings of SPIE - The International Society for Optical Engineering **6847**, 10.1117/12.761655 (2008).

[90] D. Fechtig, A. Kumar, W. Drexler, and R. A. Leitgeb, "Full range line-field parallel swept source imaging utilizing digital refocusing," Journal of Modern Optics **62**, 1 (2015).

[91] A.F. Fercher, C.K. Hitzenberger, G. Kamp, and S.Y. El-Zaiat, "Measurement of intraocular distances by backscattering spectral interferometry," Optics Communications **117**, 43 (1995).

[92] R. Leitgeb, C. K. Hitzenberger, and A. F. Fercher, "Performance of fourier domain vs. time domain optical coherence tomography," Opt. Express **11**, 889 (2003).

[93] N. Nassif, B. Cense, B. H. Park, S. H. Yun, T. C. Chen, B. E. Bouma, G. J. Tearney, and J. F. de Boer, "In vivo human retinal imaging by ultrahigh-speed spectral domain optical coherence tomography," Opt. Lett. **29**, 480 (2004).

[94] S. H. Yun, G. J. Tearney, B. E. Bouma, B. H. Park, and J. F. de Boer, "High-speed spectral-domain optical coherence tomography at 1.3 µm wavelength," Opt. Express **11**, 3598 (2003).

[95] A. G. Podoleanu, "Unbalanced versus balanced operation in an optical coherence tomography system," Appl. Opt. **39**, 173 (2000).

[96] A. Bradu and A. G. Podoleanu, "Fourier domain optical coherence tomography system with balance detection," Opt. Express **20**, 17522 (2012).

[97] S. R. Chinn, E. A. Swanson, and J. G. Fujimoto, "Optical coherence tomography using a frequency-tunable optical source," Opt. Lett. **22**, 340 (1997).

[98] R. Huber, M. Wojtkowski, and J. G. Fujimoto, "Fourier domain mode locking (fdml): a new laser operating regime and applications for optical coherence tomography," Opt. Express **14**, 3225 (2006).

[99] T. Pfeiffer, M. Petermann, W. Draxinger, C. Jirauschek, and R. Huber, "Ultra low noise fourier domain mode locked laser for high quality megahertz optical coherence tomography," Biomed. Opt. Express **9**, 4130 (2018).

[100] T. Klein, W. Wieser, L. Reznicek, A. Neubauer, A. Kampik, and R. Huber, "Multi-mhz retinal oct," Biomed. Opt. Express **4**, 1890 (2013).

[101] M. J. Marques, S. Rivet, A. Bradu, and A. Podoleanu, "Complex master-slave for long axial range swept-source optical coherence tomography," OSA Continuum **1**, 1251 (2018).

[102] T. Klein and R. Huber, "High-speed oct light sources and systems," Biomedical optics express **8**, 828 (2017).

[103] M. I. Suresh, J. Hammer, N. Y. Joly, Philip St.J. Russell, and F. Tani, "Deep-uv-enhanced supercontinuum generated in a tapered gas-filled photonic crystal fiber," Opt. Lett. **46**, 4526 (2021).

[104] A. G. Podoleanu and A. Bradu, "Master–slave interferometry for parallel spectral domain interferometry sensing and versatile 3d optical coherence tomography," Opt. Express **21**, 19324 (2013).

[105] S. Rivet, M. Maria, A. Bradu, T. Feuchter, L. Leick, and A. Podoleanu, "Complex master slave interferometry," Opt. Express **24**, 2885 (2016).

[106] C. S. Colley, J. C. Hebden, D. T. Delpy, A. D. Cambrey, R. A. Brown, E. A. Zibik, W. H. Ng, L. R. Wilson, and J. W. Cockburn, "Mid-infrared optical coherence tomography," Review of Scientific Instruments **78**, 123108 (2007).

[107] R. I. Woodward, M. R. Majewski, D. D. Hudson, and S. D. Jackson, "Swept-wavelength mid-infrared fiber laser for real-time ammonia gas sensing," APL Photonics **4**, 020801 (2019).

[108] I. Zorin, R. Su, A. Prylepa, J. Kilgus, M. Brandstetter, and B. Heise, "Mid-infrared fourier-domain optical coherence tomography with a pyroelectric linear array," Opt. Express **26**, 33428 (2018).

[109] A. Vanselow, P. Kaufmann, I. Zorin, B. Heise, H. M. Chrzanowski, and S. Ramelow, "Frequency-domain optical coherence tomography with undetected mid-infrared photons," Optica **7**, 1729 (2020).

[110] I. Zorin, P. Gattinger, A. Prylepa, and B. Heise, "Time-encoded mid-infrared fourier-domain optical coherence tomography," Opt. Lett. **46**, 4108 (2021).

[111] I. Zorin, D. Brouczek, S. Geier, S. Nohut, J. Eichelseder, G. Huss, M. Schwentenwein, and B. Heise, "Mid-infrared optical coherence tomography as a method for inspection and quality assurance in ceramics additive manufacturing," Open Ceramics **12**, 100311 (2022).

[112] K. Rottwitt and P. Tidemand-Lichtenberg, *Nonlinear optics: principles and applications*, English (CRC Press, 2014).

[113] M. Jensen, I. B. Gonzalo, R. D. Engelsholm, M. Maria, N. M. Israelsen, A. Podoleanu, and O. Bang, "Noise of supercontinuum sources in spectral domain optical coherence tomography," J. Opt. Soc. Am. B **36**, A154 (2019).

[114] M. Waller, "On-line papermaking sensors: an historical perspective," XIIth Fund. Res. Symp. Oxford, 785 (2001).

[115] J. Graeffe and S. Nuyan, "An online laser caliper measurement for the paper industry," in Optical measurement systems for industrial inspection iv, Vol. 5856, edited by W. Osten, C. Gorecki, and E. L. Novak (International Society for Optics and Photonics, 2005), pages 318–326.

[116] T. Prykäri, J. Czajkowski, E. Alarousu, and R. Myllylä, "Optical coherence tomography as an accurate inspection and quality evaluation technique in paper industry," Optical review **17**, 218 (2010).

[117] E. Alarousu, L. Krehut, T. Prykäri, and R. Myllylä, "Study on the use of optical coherence tomography in measurements of paper properties," Measurement Science and Technology **16**, 1131 (2005).

[118] M. D. Kulkarni and J. A. Izatt, "Spectroscopic optical coherence tomography," in Conference on lasers and electro-optics (1996), CMJ6.

[119] U. Morgner, W. Drexler, F. X. Kärtner, X. D. Li, C. Pitris, E. P. Ippen, and J. G. Fujimoto, "Spectroscopic optical coherence tomography," Opt. Lett. **25**, 111 (2000).

[120] F. E. Robles, C. Wilson, G. Grant, and A. Wax, "Molecular imaging true-colour spectroscopic optical coherence tomography," Nature photonics **5**, 744 (2011).

[121] H. S. Nam and H. Yoo, "Spectroscopic optical coherence tomography: a review of concepts and biomedical applications," Applied Spectroscopy Reviews **53**, 91 (2018).

[122] D. J. Faber, E. G. Mik, M. C. G. Aalders, and T. G. van Leeuwen, "Light absorption of (oxy-)hemoglobin assessed by spectroscopic optical coherence tomography," Opt. Lett. **28**, 1436 (2003).

[123] I. Gordon, L. Rothman, R. Hargreaves, R. Hashemi, E. Karlovets, F. Skinner, E. Conway, C. Hill, R. Kochanov, Y. Tan, P. Wcisło, A. Finenko, K. Nelson, P. Bernath, M. Birk, V. Boudon, A. Campargue, K. Chance, A. Coustenis, B. Drouin, J.-M. Flaud, R. Gamache, J. Hodges, D. Jacquemart, E. Mlawer, A. Nikitin, V. Perevalov, M. Rotger, J. Tennyson, G. Toon, H. Tran, V. Tyuterev, E. Adkins, A. Baker, A. Barbe, E. Canè, A. Császár, A. Dudaryonok, O. Egorov, A. Fleisher, H. Fleurbaey, A. Foltynowicz, T. Furtenbacher, J. Harrison, J.-M. Hartmann, V.-M. Horneman, X. Huang, T. Karman, J. Karns, S. Kassi, I. Kleiner, V. Kofman, F. Kwabia–Tchana, N. Lavrentieva, T. Lee, D. Long, A. Lukashevskaya, O. Lyulin, V. Makhnev, W. Matt, S. Massie, M. Melosso, S. Mikhailenko, D. Mondelain, H. Müller, O. Naumenko, A. Perrin, O. Polyansky, E. Raddaoui, P. Raston, Z. Reed, M. Rey, C. Richard, R. Tóbiás, I. Sadiek, D. Schwenke, E. Starikova, K. Sung, F. Tamassia, S. Tashkun, J. Vander Auwera, I. Vasilenko, A. Vigasin, G. Villanueva, B. Vispoel, G. Wagner, A. Yachmenev, and S. Yurchenko, "The hitran2020 molecular spectroscopic database," Journal of Quantitative Spectroscopy and Radiative Transfer **277**, 107949 (2022).

[124] I. Gunnarsson, E. S. Aradóttir, E. H. Oelkers, D. E. Clark, M. Þ. Arnarson, B. Sigfússon, S. Ó. Snæbjörnsdóttir, J. M. Matter, M. Stute, B. M. Júlíusson, and S. R. Gíslason, "The rapid and cost-effective capture and subsurface mineral storage of carbon and sulfur at the carbfix2 site," International Journal of Greenhouse Gas Control **79**, 117 (2018).

[125] S. Ó. Snæbjörnsdóttir, B. Sigfússon, C. Marieni, D. Goldberg, S. R. Gislason, and E. H. Oelkers, "Carbon dioxide storage through mineral carbonation," Nature Reviews Earth & Environment **1**, 90 (2020).

[126] S. Ó. Snæbjörnsdóttir, F. Wiese, T. Fridriksson, H. Ármansson, G. M. Einarsson, and S. R. Gislason, "Co2 storage potential of basaltic rocks in iceland and the oceanic ridges," Energy Procedia **63**, 12th International Conference on Greenhouse Gas Control Technologies, GHGT-12, 4585 (2014).

[127] C. W. Merkle, M. Augustin, D. J. Harper, and B. Baumann, "Indocyanine green provides absorption and spectral contrast for optical coherence tomography at 840 nm in vivo," Opt. Lett. **45**, 2359 (2020).

Technical University of Denmark
DTU Electro
Department of Electrical and Photonics Engineering

Ørsteds Plads 343
2800 Kongens Lyngby, Denmark
Phone: +45 4525 6352

www.electro.dtu.dk